

2016

STUDY OF MACROTURBULENCE AND BURSTING VIA THE -1 SPECTRAL POWER LAW REGION OF TURBULENT OPEN CHANNEL FLOWS OVER GRAVEL BEDS

Amirreza Ghasemi

University of Kentucky, amir_gh_reza@yahoo.com

Digital Object Identifier: <http://dx.doi.org/10.13023/ETD.2016.365>

Recommended Citation

Ghasemi, Amirreza, "STUDY OF MACROTURBULENCE AND BURSTING VIA THE -1 SPECTRAL POWER LAW REGION OF TURBULENT OPEN CHANNEL FLOWS OVER GRAVEL BEDS" (2016). *Theses and Dissertations--Civil Engineering*. 43.
http://uknowledge.uky.edu/ce_etds/43

This Master's Thesis is brought to you for free and open access by the Civil Engineering at UKnowledge. It has been accepted for inclusion in Theses and Dissertations--Civil Engineering by an authorized administrator of UKnowledge. For more information, please contact UKnowledge@lsv.uky.edu.

STUDENT AGREEMENT:

I represent that my thesis or dissertation and abstract are my original work. Proper attribution has been given to all outside sources. I understand that I am solely responsible for obtaining any needed copyright permissions. I have obtained needed written permission statement(s) from the owner(s) of each third-party copyrighted matter to be included in my work, allowing electronic distribution (if such use is not permitted by the fair use doctrine) which will be submitted to UKnowledge as Additional File.

I hereby grant to The University of Kentucky and its agents the irrevocable, non-exclusive, and royalty-free license to archive and make accessible my work in whole or in part in all forms of media, now or hereafter known. I agree that the document mentioned above may be made available immediately for worldwide access unless an embargo applies.

I retain all other ownership rights to the copyright of my work. I also retain the right to use in future works (such as articles or books) all or part of my work. I understand that I am free to register the copyright to my work.

REVIEW, APPROVAL AND ACCEPTANCE

The document mentioned above has been reviewed and accepted by the student's advisor, on behalf of the advisory committee, and by the Director of Graduate Studies (DGS), on behalf of the program; we verify that this is the final, approved version of the student's thesis including all changes required by the advisory committee. The undersigned agree to abide by the statements above.

Amirreza Ghasemi, Student

Dr. James Fox, Major Professor

Dr. Y. T. Wang, Director of Graduate Studies

STUDY OF MACROTURBULENCE AND BURSTING VIA THE -1 SPECTRAL
POWER LAW REGION OF TURBULENT OPEN CHANNEL FLOWS OVER
GRAVEL BEDS

THESIS

A thesis submitted in partial fulfillment of the requirements
for the degree of Master of Science in Civil Engineering
in the College of Engineering at the University of Kentucky

By

Amirreza Ghasemi

Lexington, Kentucky

Director: Dr. James Fox, Professor of Civil Engineering

Lexington, Kentucky

2016

Copyright © Amirreza Ghasemi 2016

ABSTRACT OF THESIS

STUDY OF MACROTURBULENCE AND BURSTING VIA THE -1 SPECTRAL POWER LAW REGION OF TURBULENT OPEN CHANNEL FLOWS OVER GRAVEL BEDS

The large scale and smaller production scale motions contain over the half of turbulent kinetic energy in the flow. These motions are responsible for sediment transport and deposition processes, contaminant mixing and stream bio-diversity. These motions are corresponded to the left and right bounds of -1 power region of the spectral energy. The most well recognized and highly studied power law has been upon Kolmogorov's $-5/3$ power law region of the streamwise spectral energy density and this research focused on investigating the -1 power region bounds and energy. Energy budget and time-average turbulence calculations along with spectral analysis are performed to investigate the characteristics of large scale and smaller production scale motions in the flow. Spectral analyses of turbulent flows offers the utility of investigating the distribution of turbulent energy across wavenumber scales as well as identifying prominent wavenumbers at which the periodicity of coherent processes are centered. In turn, the results of spectral analyses can be coupled with visualization of coherent vortices and time-average turbulence results to advance our understanding of turbulent energy distribution and dominant processes that drive environmental phenomena such as sediment transport and solute transfer. A new method for identifying the wavenumbers associated to the macroturbulence and bursting is introduced. Also this study offers a new scaling method of energy spectral that derived from the turbulence energy model for an equilibrium boundary layer. Results of this study show an equilibrium boundary layer for the outer region of the flow in which the flow is uniform and fully-developed. Also for a given roughness, the results of this study provide an approach to calculate the streamwise turbulence kinetic energy of bursting and macroturbulence which show a linkage of this work to applications such as bedload and suspended load sediment transport.

KEYWORDS: macroturbulence, bursting, -1 power region, equilibrium boundary layer

Amirreza Ghasemi

5-31-2016

STUDY OF MACROTURBULENCE AND BURSTING VIA THE -1 SPECTRAL
POWER LAW REGION OF TURBULENT OPEN CHANNEL FLOWS OVER
GRAVEL BEDS

By

Amirreza Ghasemi

James Fox

Director of Thesis

Y. T. Wang

Director of Graduate Studies

5-31-2016

Date

ACKNOWLEDGMENTS

The following thesis benefitted from the input of several people. Firstly, I would like to thank my Thesis Chair, Dr. James Fox, for his support and encouragement. I would also like to thank the other members of my Thesis Committee: Dr. Scott Yost and Dr. Dwayne Edwards. Finally, I would like to thank the University of Kentucky Civil Engineering Department for providing me the academic support to develop and implement my ideas.

Table of Contents

ACKNOWLEDGMENTS	iii
List of Tables	vi
List of Figures	vii
Chapter 1 Introduction	1
1.1 Motivation for Research of Turbulence in Rivers:	1
1.2 Background: Investigating the -1 Power Region for Macroturbulence and Bursting:.....	2
1.3 Objective:.....	6
1.4 Thesis Layout:.....	7
Chapter 2 Methods for the Small Flume.....	11
2.1 Experimental Design:.....	11
2.2 Experimental Setup:.....	13
2.3 Velocity Data Collection and Post-Processing:	15
2.4 Analyses of Time-Average Parameters: Velocities, Reynolds Stresses and Energy Terms:.....	19
2.5 Spectral Analyses:.....	25
2.6 Spectral scaling:	31
Chapter 3 Results for the Small Flume:.....	36
3.1 Validating Turbulence Data, Time-Average Parameters and Secondary Currents:.....	36
3.2 Selecting Wavenumbers for Macroturbulence and Bursting:	41
3.3 Existence and Non-Existence of the Spectral Production Region:	44
3.4 Scaling of the Wavenumbers and Energy for Macroturbulence, Bursting and the -1 Power Region Plots:	44
Chapter 4 Methods for Large Flume:	63
4.1 Experimental Design:.....	63
4.2 Experimental Setup:.....	64
4.3 Velocity Data Collection and Post-Processing:	65
4.4 Analyses of Time-Average Parameters: Velocities, Reynolds Stresses and Energy Terms:.....	65
4.5 Spectral Analyses:.....	66
Chapter 5 Results for Large Flume:.....	69

5.1 Validating Turbulence Data, Time-Average Parameters and Secondary Currents:.....	69
5.2 Selecting Wavenumbers for Macroturbulence and Bursting:.....	71
5.3 Scaling of the Wavenumbers and Energy for Macroturbulence, Bursting and the -1 Power Region Plots:	71
Chapter 6 Comparison the results of two flumes:.....	84
Chapter 7 Discussion	91
Chapter 8 Conclusion.....	107
Appendix I – Index	109
Appendix II – Procedure data collection and processing	113
Appendix III.....	135
References.....	156
VITA.....	161

List of Tables

Table 2.1. Experimental tests conditions for small flume.	34
Table 3.1. Results of the friction velocity estimated from the different methods.	47
Table 3.2. Sensitivity of macroturbulence and bursting wavenumber and energy to the number of data collected.	48
Table 4.1. Experimental tests conditions for the big flume	67
Table 5.1. Results of the friction velocity estimated from different methods for the big flume.	73

List of Figures

Figure 1.1. Visualization of coherent motions.	8
Figure 1.2. Macroturbulence and bursting structures with related bedload and suspended load transports.....	9
Figure 1.3. Conceptual figure of spectral regions.....	10
Figure 2.1. Experimental setup for the small flume.....	35
Figure 3.1. Comparison of the friction velocity from the three methods in the small flume.....	49
Figure 3.2. Example of parameter fitting to estimate the friction velocity for test 7 in the small flume.	50
Figure 3.3. Streamwise velocity distributions for the datasets in the small flume	51
Figure 3.4. Primary Reynolds shear stress and streamwise Reynolds normal stress in the small flume.....	52
Figure 3.5. Secondary velocities in the small flume.....	53
Figure 3.6. Secondary Reynolds normal stresses, TKE and anisotropy scaled with the friction velocity in the small flume	54
Figure 3.7. Method for identification of km	55
Figure 3.8. Method for identification of Kb	56
Figure 3.9. Sensitivity analysis about the number of data required to get reliable information about macroturbulence and bursting structures.	57
Figure 3.10. Example of spectral results showing no -1 power region.....	58
Figure 3.11. Scaling Km and Kb with inner and outer variables.	59
Figure 3.12. Scaling energy spectral with inner and outer variables.	60
Figure 3.13. Scaling spectral energy and wave-numbers with inner and outer variables for $y/H \leq 0.1$	61
Figure 3.14. Scaling spectral energy and wave-numbers with inner and outer variables for $y/H > 0.1$	62
Figure 4.1. Experimental setup for the large flume	68
Figure 5.1. Comparison of the friction velocity from the three methods in the large flume.....	74
Figure 5.2. Example of parameter fitting to estimate the friction velocity in the large flume	75

Figure 5.3. Streamwise velocity distributions for the datasets in the large flume:	76
Figure 5.4. Primary Reynolds shear stress and streamwise Reynolds normal stress in the large flume	77
Figure 5.5. Secondary velocities in the large flume.....	78
Figure 5.6. Secondary Reynolds normal stresses, TKE and anisotropy scaled with friction velocity in the large flume	79
Figure 5.7. Scaling K_m and K_b with inner and outer variables.....	80
Figure 5.8. Scaling energy spectral with inner and outer variables.....	81
Figure 5.9. Scaling spectral energy and wave-numbers with inner and outer variables for $y/H \leq 0.4$	82
Figure 5.10. Scaling spectral energy and wave-numbers with inner and outer variables for $y/H > 0.4$	83
Figure 6.1. Comparison of streamwise velocity distribution for two flumes.....	86
Figure 6.2. Comparison of primary Reynolds shear stress streamwise Reynolds normal stress for two flumes	87
Figure 6.3. Comparison of secondary Reynolds normal stresses, TKE and anisotropy for two flumes.....	88
Figure 6.4. Relationship between energy spectral of ‘-1’ power region and streamwise Reynolds normal stress.	89
Figure 6.5. Plot of $K_m H$ vs H/K_s for both flumes	90
Figure 7.1. Plot of the equation developed for energy prediction for small flume.....	103
Figure 7.2. Plot of the equation developed for periodicity prediction for small flume ..	104
Figure 7.3. Plot of the equation developed for energy prediction for large flume	105
Figure 7.4. Plot of the equation developed for periodicity prediction for large flume ...	106

Chapter 1 Introduction

1.1 Motivation for Research of Turbulence in Rivers:

Large scale motions, known as macroturbulence, and smaller production scale motions, known as bursting, exist as a double-layer of turbulence generation characterized by quasi-periodic coherent motions (Figure 1.1). These motions are believed to be responsible for bedload and suspended load transport, respectively, in a river system and can impact ecosystem processes through solute transfer (Figure 1.2). Macroturbulence and bursting correspond to the left and right bounds of the -1 power region of the spectral energy. The most recognized and highly studied power law is based upon Kolmogorov's $-5/3$ power law region of the spectral energy; fewer studies have investigated the -1 power law region. A better understanding of the existence or non-existence of the -1 power law region, as well as of its bounds and energy is expected to allow the prediction of the periodicity and turbulent energy of macroturbulence and bursting. Consequently, this study advances a more explicit inclusion of the physics of the coherent motions within hydraulics and sediment transport models. Some studies have been done to investigate large scale and smaller scale production motions, but a new study that allows researchers to predict the energy and length scale of these motions is needed. In this regard, the motivation of this work is to better understand these motions and predict the periodicity and turbulent energy of macroturbulence and bursting in open channel flow over a gravel bed for a range of hydraulic conditions.

1.2 Background: Investigating the -1 Power Region for Macroturbulence and Bursting:

Spectral analyses of turbulent flows offer the utility of investigating the distribution of turbulent energy across wavenumber scales as well as of identifying prominent wavenumbers, or eddy scales, at which the periodicity of coherent processes are centered (Venditti and Bennet, 2000). In turn, the results of spectral analyses can be coupled with visualization of coherent vortices and time-average turbulence results to advance our understanding of turbulent energy distribution and dominant processes driving environmental phenomena such as sediment transport and solute transfer (Nikora and Roy., 2012, book chapter 1). Spectral investigation of instantaneous velocity data from turbulent open channel flow has shown the prevalence of consistent power law regions associated with turbulent energy production, transfer, and dissipation (Nezu and Nekagawa, 1993; Nikora, 2005). The most highly studies of power law have been based on Kolmogorov's -5/3 power law region of the streamwise spectral energy density and its association with the transfer of turbulent energy to the dissipative scale. The authors found a previous study (Nikora, 2005), with less systematic investigation of experimental conditions, that inquired into the -1 power region of the streamwise spectral energy density for open channel flow over a gravel bed. Therefore, our motivation in this paper was to investigate the -1 power region by carefully examining its existence, its bounds, and its scaling over a range of hydraulic conditions. Thereafter, authors discuss the prominent turbulent features that the -1 power region captures within the context of the turbulent flow structure in the open channel flow over a gravel bed.

The -1 power region is conceptualized in Figure 1.1. The spectral plot is shown to exhibit a constant -1 slope when the streamwise spectral energy density is plotted in a log-log scale (Figure 1.1a). The figure shows the most typical spectral plotting in the literature in log-log scale in which the vertical axis is the logarithm of the power spectral density while the horizontal axis is the logarithm of the wavenumber. In this type of plotting, the power law regions of the spectra can be easily visualized; e.g., see the -1 and -5/3 regions in the plot. In order to gain more information about the energy or variance level that an individual wavenumber exhibits within the flow, the spectra can be plotted in a variance preserving form. The variance preserving form, also called the pre-multiplied spectra, is a semi-log spectral plot in which the vertical axis is the multiplication of the power spectral density and its corresponding wavenumber while the horizontal axis is the logarithm of the wavenumber. This type of plot is called a variance preserving form since the area under the curve between two frequencies corresponds to the spectral signal variance in the specified interval. The plotting preserves the variance mathematically as

$$\sigma^2 = \int_{k_1}^{k_2} KS(K)d(\log(K)) = \int_{k_1}^{k_2} S(K)dK \quad (1)$$

where K is wavenumber and $S(K)$ is spectral energy. In this manner, the area under the curve within a wavenumber interval for the variance preserving plot is the level of energy contained in that interval, and it is useful for energy level comparison across wavenumbers. The variance preserving form plot in Figure 1.1b shows visually that the -1 power region is a region in which all eddy scales have the same energy associated with them.

The constant turbulent energy of eddy scales within the -1 power region is a fascinating phenomenon, and a number of historic studies investigated its nature and

prediction within turbulent shear flows and for turbulent wall-bounded flows (e.g., Tchen, 1953; Perry and Abell, 1977). While approaches to predicting the -1 power region have varied from semi-empirical, via dimensional analyses, to theoretical modeling by considering idealized eddies (Kader and Yaglom, 1984; Perry and Chong, 1982), a consistent conceptual understanding of the -1 power region has centered around its association with turbulent energy production within the flow and the fact that the -1 power region is not universal to all locations within all turbulent flows (see review Table 1 in Katal and Chu, 1998). In the case of wall-bounded flows (characteristic of open channel flow over a gravel bed), a consistent conceptual model of the -1 power region can be further extended to reflect a hierarchy of overlapping, if not bound, vortical structures that are responsible for production of turbulent energy from the mean flow (Perry and Abell, 1977; Perry and Chong, 1982; Kim and Adrian, 1999; Nikora, 1999). In this manner, the low and high wavenumber extent of the -1 power region have been suggested to indicate a bimodal interpretation of two prominent and recurring vortical scales within the turbulent flow including a very-large scale motion and smaller production scale motions (Kim and Adrian, 1999).

In the case of open channel flow over a gravel bed, turbulent energy production has been suggested to be associated with two coherent eddy scales, including the macroturbulence associated with coherency that comprises the full flow depth as alternating fluid zones of constant momentum and the bursting phenomena associated with near-bed shedding (Roy et al., 2004). The -1 power region of the streamwise spectra indicates turbulent energy production across wavenumbers and therefore can be used to indicate the periodicity and energy of macroturbulence and bursting within the flow, and

the macroturbulence and bursting wavenumbers (K_m and K_b) bounding the -1 power region are conceptualized in Figure 1.1. Macroturbulence is manifested as a broad peak in the streamwise spectra at the low wavenumber boundary of the -1 power region for open channel flow over a gravel bed (Fox et al., 2005; Stewart and Fox, 2015), which is consistent with the scale of very-large scale motion bounding the -1 power region found for pipe flows (Kim and Adrian, 1999). Bursting is conceptualized in Figure 1.1 to be manifested as the smaller scale, upper wavenumber boundary of the -1 power region, at which shedding occurs. In this manner, the -1 power region indicates the previously identified turbulence production scales and the conceptual model of the -1 power region can be investigated under a range of hydraulic conditions.

The authors found that few studies have investigated the characteristics of the -1 power region for open channel flow over a gravel bed. The exception has been the work of Nikora and his co-authors, and their work included a number of significant advancements to our knowledge of spectra, including a proposed four-range spectral model that includes a zero slope power region (Nikora and Goring, 1998), an explanation of the -1 power region based on the eddy hierarchy (Nikora, 1999), and proposed scaling for the open channel flow case based on inner variables (Nikora, 2005). That said, Nikora (2005) highlights the need for further study of the boundaries between power law regions across experimental conditions and a need to further study the linkages between spectral scaling and coherent structures. Two important reasons for the lack of on-going investigation of the -1 power region are the extensive data at a single location needed to quantify energy at the low wavenumber scales and difficulty with the ambiguity of choosing boundaries between spectral scaling regions.

1.3 Objective:

With past innovations and knowledge as well as current limitations in mind, the author is investigating the -1 power region by carefully examining its existence, its bounds, and its scaling over a range of hydraulic conditions within an open channel flow over a gravel bed. Experiments are designed with the intent to capture a wide range of energy gradients and flow depths in a laboratory flume in order that variation of the -1 slope region might be captured. After post-processing and validating the turbulence dataset and its time-average parameters, emphasis is placed upon the sensitivity and selection of K_m and K_b , and a number of sub-classifications of the -1 power region are observed. The existence or non-existence of the -1 power region is investigated in relationship to the turbulence energy budget and specifically the ratio of turbulent energy production to turbulent energy transfer is used to categorize the spectral cases. Thereafter, scaling of K_m and K_b and the spectral energy within the -1 power region is carried out following the inner and outer scaling proposed in the literature and a new scaling method proposed here. The latter scaling method is argued by the author due to its linkage to the turbulent kinetic energy budget for the open channel flow case, as derived from semi-empirical analyses. Finally, the author provides a discussion and inference of the prominent turbulent features that -1 power region captures within the context of the turbulent flow structure within open channel flow over a gravel bed.

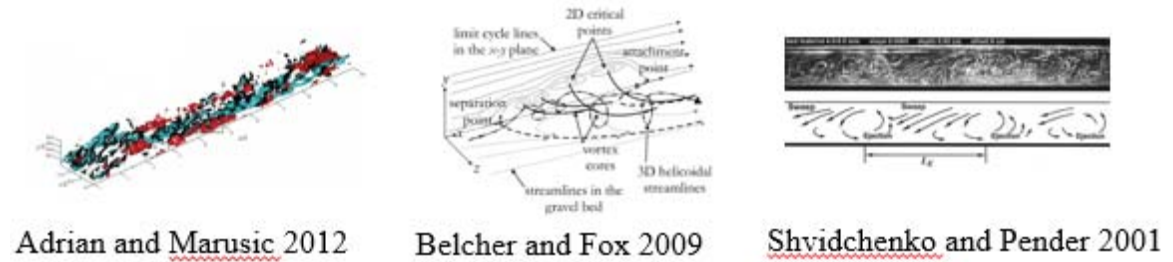
1.4 Thesis Layout:

The thesis is organized as follows. Chapter 1 provides the motivation for research of turbulence in rivers. In this chapter, a background about the research that has been done to investigate the -1 power law region is discussed, then the objectives of this study are presented. Chapter 2 provides the methods author used to collect and analyze data for the small flume. In this chapter, facility description and experimental designs are described first. Then, the methods used for preparing the flume for collecting data with Sontek micro ADV and Nortek Vectrino Profiler II are included. Finally the methods for post-processing the collected data and performing spectral analysis are described. Chapter 3 presents the results of data analysis for the small flume. Data validation, macroturbulence and bursting wavenumbers, and the existence and non-existence of -1 region and spectral parameters scaling are the results included in this chapter. Chapter 4 provides the methods used to collect data in the big flume and highlights the difference in the methods between the two flumes. Chapter 5 presents the results of data analysis for the big flume. Data validation, macroturbulence and bursting wavenumbers, spectral parameters scaling, and comparison of the results for the two flumes are included in this chapter. Chapter 6 provides a discussion about the turbulence hypotheses and eddy structures. Chapter 7 concludes this thesis and suggests the future work that can be done on this research topic.

CHAPTER 1 TABLES AND FIGURES

Figure 1.1. Visualization of coherent motions. (a) Macroturbulence structures. (b) Bursting structures

a



b

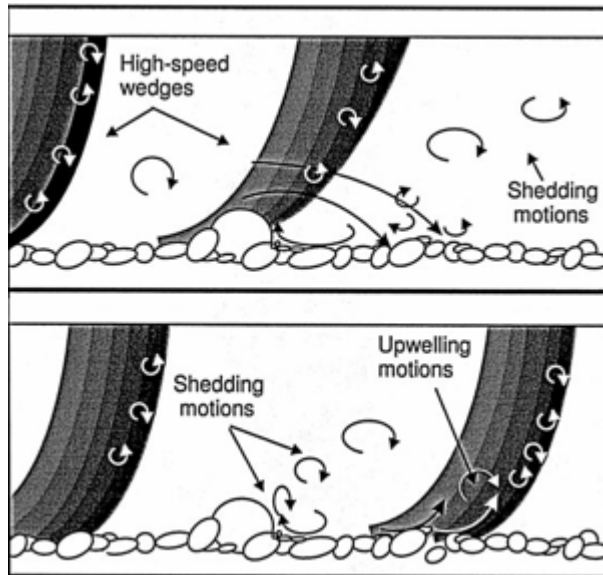


Figure 1.2. Macroturbulence and bursting structures with related bedload and suspended load transports

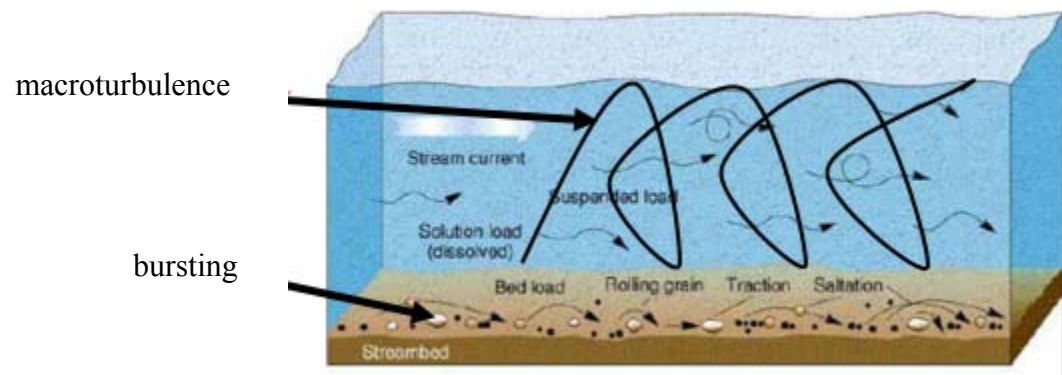
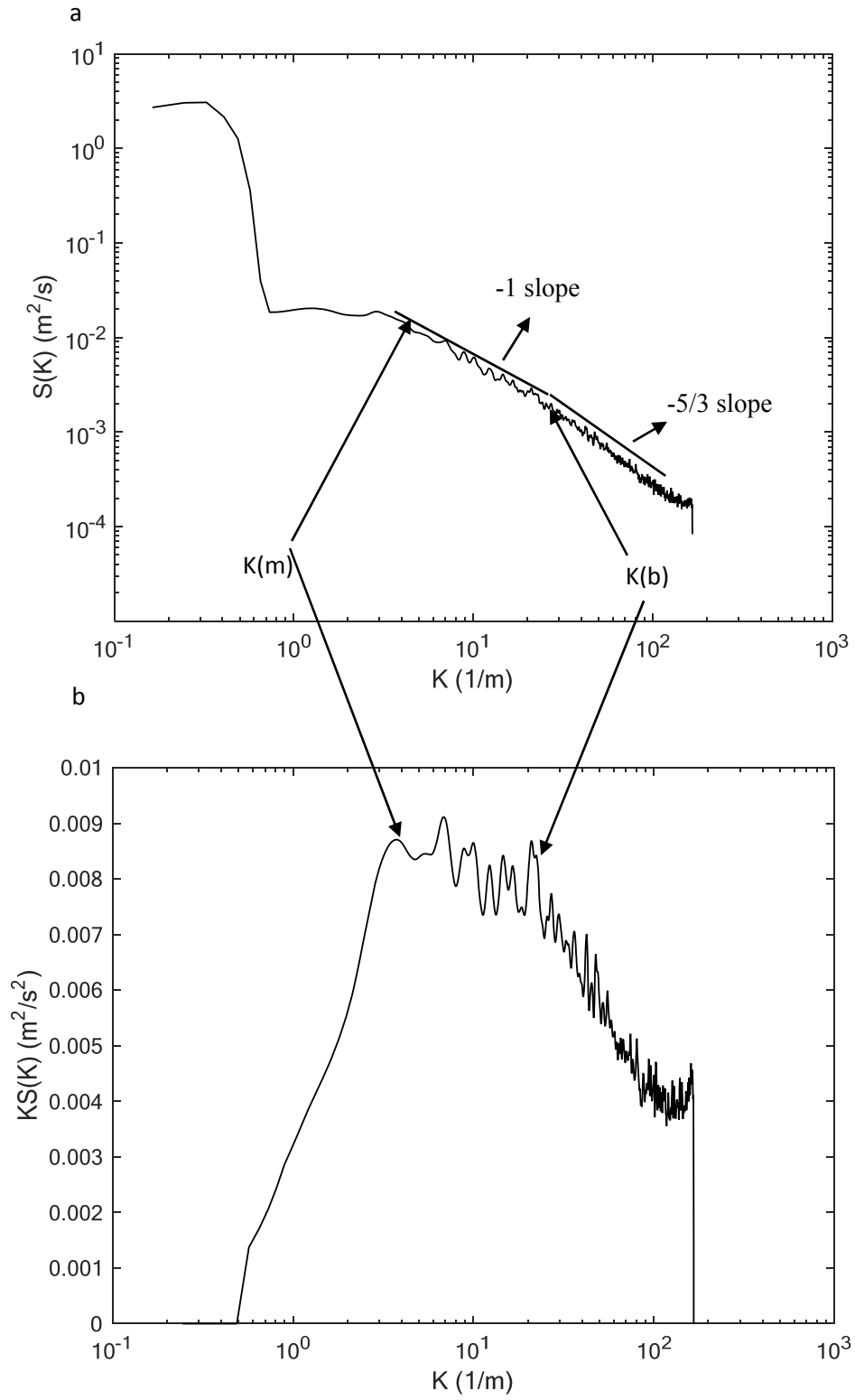


Figure 1.3. Conceptual figure of spectral regions. (a) Power spectral density form. (b) Variance preserving form



Chapter 2 Methods for the Small Flume

2.1 Experimental Design:

Experiments were designed with the intent to capture a wide range of hydraulic conditions within the laboratory flume to investigate the variation of the -1 slope region. Test variables are shown in Table 2.1. In the small flume, the author designed and carried out the 11 tests shown in Table 2.1 to investigate the turbulence production as described in the Chapter 1. The 11 tests included three different slopes and four different flow depths for each slope. We could not collect data for the flow depth of 0.2 m at the slope of 0.006 due to the limitation of the head-box. The basis for this design is discussed in the next paragraphs.

The focus was placed upon investigating uniform and fully developed turbulent open channel flow over the gravel beds. The laboratory flume was straight and fixed width with a rectangular cross section, and externally we could vary the bed slope (S), gravel particle roughness height (k_s), and volumetric discharge (Q) while flume width (B), gravitational acceleration (g), the fluid density (ρ), and viscosity (μ) were fixed (i.e., water at room temperature). For the present set of tests, the roughness height was kept fixed, and therefore the primary variables that could be adjusted externally were the bed slope and discharge. Therefore, in investigating the behavior of the -1 power region, we considered the following functional relationship in our design as

$$k_M, k_B, [kS]_{-1} = fn\{u_o, y, H, k_s, g, B, \nu\}, \quad (2)$$

where u_o is the velocity scale, y is the distance from the bed (m), H is the flow depth (m), and ν ($\frac{m^2}{s}$) is the kinematic viscosity. We assume consistency with Clauser's definition of

an equilibrium boundary layer, and therefore the friction velocity was chosen as the velocity scale that is assumed to be a constant (Clauser, 1952, 1954; Townsend, 1976). As mentioned, the roughness height was fixed for the study and the relative submergence was always greater than five such that a pronounced outer flow region existed for the study and the flow profile was not dominated by the roughness elements alone (Belcher and Fox, 2010). Gravitational influence upon the flow was incorporated into the study by varying the bed slope and hence the velocity and depth scales, although the flow was constrained to subcritical flow conditions. The width influence was kept relatively constant in that the aspect ratio (B/H) was less than or equal to six. Therefore, weak secondary motion existed in all of the tests although the secondary motion did not vary considerably in magnitude across tests, which was verified with velocimetry. Based on the conditions of the testing, the functional dependence of spectral variables to the independent variables was updated as

$$k_M, k_B, [kS]_{-1} = fn\{u_*, y, H, v\} . \quad (3)$$

The independent variables in Equation (3) provided the basis for scaling of the presumed dependent spectra response variables. Specifically the inner variables (y, v) and the outer variable (H) were coupled with the velocity scale to scale the spectra. Scaling of the -1 power region variables tested previous inner and outer scaling proposed in the literature (Perry and Chong, 1986; Kim and Adrian, 1999; Nikora, 2005) as well as outer scaling proposed here for the open channel case. In the literature, friction velocity is used to scale the energy of structures while y is used to scale the length of structures. This scaling method will be described later in section 2.6. We assume the energy of eddies in the streamwise direction is related to the velocity fluctuations or turbulent intensities. Based

on this we proposed a new scaling method which will be described in section 2.6. In order to vary the independent variables in Equation (3) and investigate our new scaling method, the 11 tests in Table 1 were carried out.

2.2 Experimental Setup:

Two different recirculating flumes with different roughness were used to simulate the conditions in rough open channel flows in the real world. The first flume (small flume with small roughness) is described in this chapter.

The small recirculating flume was 12 m long and 0.61 m width. The flume bed had immobile gravel roughness elements to provide hydraulic rough flow. The flume was made from fiberglass-resin panels and Plexiglas was used for its side walls. Photogrammetric microscopy technique is used to measure the particle size distribution. Flume had gravel roughness elements with $D_{84} = 0.0056\text{ m}$, standard deviation 0.0014 m and $D_{50} = 0.0044\text{ m}$ where D_{84} is the size that 84% of particles has a smaller size and D_{50} is the median size. In order to deliver water to the flume, we used a 40 HP pump with delivery pipes of size 8 inches. A headbox was used to dissipate turbulence from the inflowing pipe. Just downstream of the headbox, a honeycomb device with 12.7 cm long by 6.4 mm diameter was used to assist with providing rectilinear flow. Discharge was controlled by the gate-valve placed on the supply line which connected the pump to the head-box. Data collection were placed at approximately 7.5 m downstream of the inlet to provide the fully developed conditions. Also the testing section was away from the outfall to eliminate the possible effect of outfall on the fully developed and quasi-uniform conditions. The channel

discharged to the reservoir at approximately 5 m downstream of the pump that supplied the water from the reservoir into the channel. The outfall was controlled by bigger particle elements to provide the uniform conditions at the testing section. Flume slope was determined by placing the survey rod with an accuracy of 3.1 mm on the flat part of the side-wall which was believed to be straight. Elevation measurements were taken at the entrance of the flume, immediately after the honeycomb, and at the end of the flume, just before flow discharge to the outfall. To check the accuracy of bed slope, elevation measurements were taken at the middle of the flume as well. Flume slope was adjusted to the new slope by elevating the flume entrance and four supports along the flume.

Prior to testing, it was necessary to ensure that the pump was operating correctly and that the flow had stabilized within the flume. The procedure for operating the apparatus included the following steps. Both the gate-valve and outlet-valve should be closed. Then, air from the pipe connecting the source of water to the pump should be vacuumed. Use the vacuum line and wait until water comes out of the suction line valve. Once water comes out of the suction line valve, close the valve. After closing the valve, the flume is ready for running and turn the motor pump to the ON position and wait about 10 seconds. Then, open the gate-valve and wait until the flow stabilizes before taking any measurements. Stability is reached when variation in the average velocity values becomes minimum. Authors waited 1 hour for the flow to be stabilized. It is necessary to measure the depth of water in the reservoir during data collection. Depth of water in the reservoir should not change during data collection to keep the hydraulic parameters and flow conditions constant. Also flow depth in the flume should be measured at different sections close to testing section during data collection to guarantee the uniform flow.

2.3 Velocity Data Collection and Post-Processing:

Initially, instantaneous velocity data was collected with two instruments including a Sontek ADV and a Nortek Vectrino Profiler II ADV. Both instruments were used to provide reliable and repeatable data. The instrument comparison process was both arduous and important to maintain quality assurance of the turbulence data. Approximately four months of research were needed to gain confidence with the instruments. Thereafter, the Nortek Vectrino Profiler II with a maximum sampling frequency of 100 Hz was chosen for data collection. The Nortek was chosen due to its higher sampling frequency and ability to collect an entire instantaneous profile.

The Nortek Vectrino Profiler acoustic Doppler velocimeter, or just ADV from now on, measures the velocity of water for a range of 4 cm to 7.4 cm away from the probe transmitter. After some investigation of data quality and discussion with the manufacturer, we preferred to use the ‘sweet spot’, a point located 5 cm away from the probe transmitter, for data to be post-analyzed because the *Multi-instrument Turbulence Toolbox* (MITT), an open source code which we used for post-processing the data, does not provide a filtering option based on COR (correlation) and SNR (signal to noise ratio). The ‘sweet spot’ point has the highest COR and SNR and is more reliable. SNR values are above 15, a threshold at which instantaneous velocities are measured and turbulence quantities are calculated, and COR values are above 70, another threshold to guarantee the quality of data. Moreover, turbulent parameters calculated for a profile acquired by the ADV, 4-7.4 cm away from the probe, exhibit a shift in their trend at the sweet spot. In other words, for example, turbulent kinetic energy decreases from 7.4 to 5 cm and then it increases from 5 to 4 cm away from

the probe. Signals transmitted by the ADV converge best at the sweet spot which cause it to be the most reliable point in the whole 3.5 cm profile.

Author used a clamp attached to a rod to hold the instrument. Author secured the clamp to the 3 cm diameter rigid section of the probe near the ADV receivers. The author strongly recommends not securing the clamp to the flexible portion of the probe stem to prevent damage to the ADV. Author used a guide rod and extended it to the bed to prevent vibration of instrument to avoid noisy and unreliable data. Author secured the end of the guide rod into a predrilled hole in the bed. At the lowest location for collecting data, the guide rod could be extended 6 cm into the bed. Therefore, the instrumentation apparatus could be moved upward in the vertical distance of 6 cm. Depending on the flow depth at which author collected data, sometimes author had to stop running the flume and changes the position of the probe before collecting the data for another 6 cm.

Author collected all the velocity profile with the down-looking orientation except the upper 6 cm of the profile, which collected with the side-looking orientation. For the down-looking orientation, author used a level to orient the probe stem to the vertical. Then, author measured two points on the receiver from the wall. These two points should have equal distance from the wall to be sure that the stream-wise receiver is in the direction of the flow. For the side-looking orientation, author used a square to orient the probe stem so that it was vertical to the direction of the flow. Thereafter, the stream-wise receiver would be in the direction of the flow. Author also again measured the distance of two different points on the probe stem and changed the probe position until these two points had equal distance from the bed. Author ran the flume and measured the height of the screw on the gate-valve and depth of water in the reservoir to guarantee that the hydraulic parameters

would not change during the data collection. As previously mentioned, author waited 1 hour to ensure that the flow stabilized prior to testing.

Author used the control module to adjust both the probe and the guide rod by hand to a new vertical position. An interesting characteristic of the Nortek Vectrino Profiler II ADV is that it measures the distance of the probe from the bed for the down-looking orientation. Author used this characteristic to check the distance of the probe from the bed. Author collected all the possible points with the down-looking orientation, then changed the orientation to side-looking to collect the upper 6 cm of the profile.

In order to collect data with the ADV, author first installed the *Vectrino Profiler VI.32* software onto a PC and then installed *Java (JVM)* due to the fact that the ADV software requires this language to operate. To ensure that data quality was high, a transducer test was first performed prior to any testing, and the velocity amplitude and standard deviation were investigated. In addition, a probe check was always performed to produce long average amplitude vs. range profiles for each of the four beams before data collection begins; the author ensured that the four profiles from the four beams were roughly the same, with similar peaks and shapes at the same range.' (SW User Guide). The sampling rate was set to 50 Hz. Author collected data at each point for 30 minutes, at a total of 90,000 three dimensional velocity data per point. After collecting the data at a single point, the ADV probe was moved approximately 1 cm in the vertical to a new point, and data was collected. Approximately 13 points per profile were collected. As part of this research, 48.6 million velocity data were collected, analyzed.

In order to post-process the ADV data to ensure its quality and remove erroneous spikes due to acoustic reflections, the MITT (MacVicar et al. 2014), was used. MITT is an

open source code in MATLAB written by MacVicar. MITT codes can be found at the following link: (<http://www.mathworks.com/matlabcentral/fileexchange/47805-mitt>). Author exported the saved ADV data from the Vectrino Profiler software prior to importing it to MITT. Due to the large amount of data, the author recommends exporting data into the MATLAB format. Before we used the MITT to post-process our data, we created a CVS control file using the format described in MacVicar (2014) paper.

The main goal in using MITT codes was to clean our data and remove noise and spikes from them. After author chose the options to organize the data, he used the ‘Clean raw time series’ options to despiking the data. Different filtering and despiking methods are provided in MITT, including the standard deviation method (MacVicar et al. 2014); the one side skewness method (Macvicar et al. 2014); the phase space method (Goring and Nikora 2002); and the velocity correlation method (Cea et al. 2007). The author did not find substantial differences between the despiking methods; therefore, the phase space method was used because it not only works well for despiking the data but also is independent of any coefficients used in ‘Standard deviation’ and ‘One side skewness’ methods (Goring and Nikora 2002). The phase space method is based on plotting the velocity components against their derivatives and removing spikes, which are the points lying outside of an ellipsoid (Goring and Nikora 2002). The ‘freeze good data’ option within MITT was used with the phase-space threshold method for despiking because it keeps the good data, which is the data adjacent to the spikes. If the ‘freeze good data’ option is not activated, then data that is adjacent to the spikes would be determined as spikes, and therefore MITT will remove them. Author used the option provided in MITT to replace the detected spikes. This option replaced spikes with the linear interpolation for the points before and after the

spikes. Filtering was also investigated for the datasets, and the low pass third order Butterworth was tested. This method is based on removing the Doppler or white noises above the Nyquist frequency (one half of the sampling rate) (Macvicar et al. 2014). The author did not use the filtering option because it did not change data that much, and consequently author preferred to manipulate data as little as possible. After the analysis, the MITT output a file (.mat format) contained the clean data for further investigation of turbulence parameters and spectra.

2.4 Analyses of Time-Average Parameters: Velocities, Reynolds Stresses and Energy Terms:

Author calculated the average turbulence parameters to understand more about the hydraulic parameters and turbulent processes that occurred in different flow conditions. The average turbulence parameters are those derived from Reynolds-averaging (i.e., time-averaging), the conservation of momentum, and mechanical energy equations. Author developed a MATLAB code to analyze and calculate the average turbulent parameters of the clean data acquired by MITT.

In order to calculate the average turbulent parameters correctly, it is very important to consider the coordinate system of the instruments. The Nortek Vectrino II Profiler ADV follows the right hand coordinate system. According to the instrument's manuals, the Z direction is the direction from the transmitter toward the probe stem. Also, the stream-wise receiver should always be in the flow direction, and author can use the right hand rule to find out the positive direction of the other axis. Author put the stream-wise receiver in the

negative direction of the flow and used the following equations to convert the instrument's coordinate systems into our flow field coordinate system. In the coordinate system of the fluid, u is the stream-wise direction of instantaneous velocity where the positive direction is in the direction of the streamwise mean, v is the vertical direction of instantaneous velocity where positive is in the upward vertical, and w is the span-wise direction of instantaneous velocity where the positive value follows the right hand convention. For the down-looking orientation, author converted the instrument's coordinate systems (V_x, V_y, V_z) to the coordinate system of the fluid (u, v, w) using the following conversions: $u = -V_x$, $w = -V_z$, $v = V_y$. For the side-looking orientation, author used the following conversions: $u = -V_x$, $v = V_y$, $w = -V_z$. Author implemented these changes in the developed MATLAB code for analyzing the ADV data.

After converting the data to the flow's coordinate system, author calculated average turbulent parameters for the sweet spot from each reading. Mean velocities arise from the perturbation equation as:

$$u = U + u', \quad v = V + v', \quad w = W + w' \quad (4)$$

$$U = \frac{1}{n} \sum_{i=1}^n u_i, \quad V = \frac{1}{n} \sum_{i=1}^n v_i, \quad W = \frac{1}{n} \sum_{i=1}^n w_i \quad (5)$$

The first parameter is U , which is the average stream-wise velocity. The second parameter is V , which is the average vertical velocity. The third parameter is W , which is the average span-wise velocity. The fourth parameter is the velocity magnitude which we calculated using the following equation.

$$V_{mag} = \sqrt{U^2 + V^2 + W^2} \quad (6)$$

Author also calculated the time-average stress parameters, or normal and shear Reynolds stresses, that arise from derivation of the Reynolds Average Navier Stokes (RANS) equation. The RANS equation is give as:

$$\frac{\partial \bar{u}_i}{\partial t} + \bar{u}_j \frac{\partial \bar{u}_i}{\partial x_j} = g_i - \frac{1}{\rho} \frac{\partial \bar{p}}{\partial x_i} - \frac{\partial \overline{u'_i u'_j}}{\partial x_j} + \frac{\partial}{\partial x_j} (\nu \frac{\partial \bar{u}_i}{\partial x_j}) \quad (7)$$

Streamwise Reynolds normal stress is related to the stream-wise velocity fluctuations, and author used the following equation for this parameter:

$$RMS(u) = [\frac{1}{n} \sum_{i=1}^n (u_i - U)^2]^{0.5} \quad (8)$$

Vertical Reynolds normal stress is related to the vertical velocity fluctuations, and author used the following equation to calculate this parameter:

$$RMS(v) = [\frac{1}{n} \sum_{i=1}^n (v_i - V)^2]^{0.5} \quad (9)$$

Lateral Reynolds normal stress is related to the span-wise velocity fluctuations, and author used the following equation to calculate this parameter:

$$RMS(w) = [\frac{1}{n} \sum_{i=1}^n (w_i - W)^2]^{0.5} \quad (10)$$

The next three parameters are the shear stress parameters. Author used the following equation to calculate the first Reynolds shear stress:

$$Primary\ Reynolds\ Stress = \frac{1}{n} \sum_{i=1}^n (u_i - U)(v_i - V) \quad (11)$$

Author calculated the secondary Reynolds shear stresses using the following equations:

$$Secondary\ Reynolds\ Stress = \frac{1}{n} \sum_{i=1}^n (u_i - U)(w_i - W) \quad (12)$$

$$\text{Secondary Reynolds Stress} = \frac{1}{n} \sum_{i=1}^n (v_i - V)(w_i - W) \quad (13)$$

The vorticity equation provides further interpretation of the turbulent flow, and therefore the anisotropy arising within the vorticity equation was calculated. The vorticity equation for steady and uniform open channel flow is given as:

$$\bar{u}_2 \frac{\partial \bar{\omega}_1}{\partial x_2} + \bar{u}_3 \frac{\partial \bar{\omega}_1}{\partial x_3} = \frac{\partial^2}{\partial x_2 \partial x_3} (\overline{u'^2_3} - \overline{u'^2_2}) + \left(\frac{\partial^2}{\partial x_3^2} - \frac{\partial^2}{\partial x_2^2} \right) (-\overline{u'_3 u'_2}) + \frac{\partial}{\partial x_j} \left(\nu \frac{\partial \bar{\omega}_1}{\partial x_j} \right) \quad (14)$$

Within the vorticity equation, anisotropy is given as:

$$\text{Anisotropy} = \frac{1}{n} \sum_{i=1}^n (v_i - V)^2 - \frac{1}{n} \sum_{i=1}^n (w_i - W)^2 \quad (15)$$

The vorticity equation is used to describe the secondary flows in open channels. It is believed that the difference between the first and second right hand side (RSH) terms in the equation above caused the secondary flows to generate. The first RHS term is anisotropy which is related to vorticity generation and the second RHS term is related to vorticity dissipation.

Terms of the Reynolds averaged mean and turbulent kinetic energy (MKE and TKE) equations were also investigated due to the fact that it is believed in the literature that energy-based consideration is a suitable way to analyze the coherent structures in the turbulent flow. The first equation is the MKE equation, and the second one is the TKE equation given as:

$$\begin{aligned} \frac{\partial}{\partial t} \left(\frac{\overline{u_i^2}}{2} \right) + \bar{u}_j \frac{\partial}{\partial x_j} \left(\frac{\overline{u_i^2}}{2} \right) = & g_i \bar{u}_i - \frac{\partial}{\partial x_j} \left[\frac{1}{\rho} \bar{u}_i \bar{p} + \bar{u}_i \overline{u'_i u'_j} - \nu \frac{\partial}{\partial x_j} \left(\frac{\overline{u_i^2}}{2} \right) \right] + \overline{u'_i u'_j} \frac{\partial \bar{u}_i}{\partial x_j} - \\ & \nu \left(\frac{\partial \bar{u}_i}{\partial x_j} \right)^2 \end{aligned} \quad (16)$$

$$\begin{aligned} \frac{\partial}{\partial t} \left(\frac{\overline{u'_i u'_i}}{2} \right) + \bar{u}_j \frac{\partial}{\partial x_j} \left(\frac{\overline{u'_i u'_i}}{2} \right) = & -\overline{u'_i u'_j} \frac{\partial \bar{u}_i}{\partial x_j} - \frac{\partial}{\partial x_j} \left[\frac{1}{\rho} \overline{p' u'_j} + \frac{\overline{u'_i u'_i u'_j}}{2} - \right. \\ & \left. \overline{v u'_i} \left(\frac{\partial u'_i}{\partial x_j} + \frac{\partial u'_j}{\partial x_i} \right) \right] - \frac{\nu}{2} \sum_{i,j} \overline{\left(\frac{\partial u'_i}{\partial x_j} + \frac{\partial u'_j}{\partial x_i} \right)^2} \end{aligned} \quad (17)$$

The equations above consider all three directions of the flow, but author focused on the stream-wise direction. The form of the equations used in this study is shown below. The first equation is the MKE equation.

$$V \frac{\partial}{\partial y} \left(\frac{\bar{u}^2}{2} \right) + W \frac{\partial}{\partial z} \left(\frac{\bar{u}^2}{2} \right) = gSU + \overline{u'v'} \frac{\partial \bar{u}}{\partial y} + \overline{u'w'} \frac{\partial \bar{u}}{\partial z} - \frac{\partial}{\partial y} [\bar{u} \overline{u'v'}] - \frac{\partial}{\partial z} [\bar{u} \overline{u'w'}] \quad (18)$$

The terms on the left hand side (LHS) of the equation are related to the convection of mean kinetic energy by the secondary flows. The first term on the RHS of the equation is related to the energy input by gravity. The sum of the next two terms, $\overline{u'v'} \frac{\partial \bar{u}}{\partial y} + \overline{u'w'} \frac{\partial \bar{u}}{\partial z}$, are the negative terms of energy production that take energy from the mean flow. The last two terms on the right hand side, $\frac{\partial}{\partial y} [\bar{u} \overline{u'v'}]$ and $\frac{\partial}{\partial z} [\bar{u} \overline{u'w'}]$, are related to the turbulent energy transport by the mean flow.

The form of the TKE energy equation used in this study is shown below.

$$V \frac{\partial}{\partial y} \left(\frac{\overline{u'^2}}{2} \right) + W \frac{\partial}{\partial z} \left(\frac{\overline{u'^2}}{2} \right) = -\overline{u'v'} \frac{\partial \bar{u}}{\partial y} - \overline{u'w'} \frac{\partial \bar{u}}{\partial z} - \frac{\partial}{\partial y} \left[\frac{\overline{u'^2 v'}}{2} \right] - \frac{\partial}{\partial z} \left[\frac{\overline{u'^2 w'}}{2} \right] \quad (19)$$

The terms on the LHS of the equation are related to the convection of TKE by the mean flow. The first two terms on the RHS of the equation, $\overline{u'v'} \frac{\partial \bar{u}}{\partial y}$ and $\overline{u'w'} \frac{\partial \bar{u}}{\partial z}$, are related to

the production terms that add turbulent energy to the flow. The last two terms on the RHS of the equation, $\frac{\partial}{\partial y} [\frac{\overline{u'^2 v'}}{2}]$ and $\frac{\partial}{\partial z} [\frac{\overline{u'^2 w'}}{2}]$ are related to the turbulent energy transport.

Author first calculated the different terms above, then fitted a line to calculate the derivatives with regard to y or z direction. For the terms $\frac{U^2}{2}$ and U , author fitted a logarithmic line because he noticed that they follow the log law, as he compared them to the laws to check their quality. For the term $\frac{\overline{u'^2}}{2}$ author fitted an exponential line and then calculated the derivative. For the other terms, author fitted a polynomial and then calculated the derivatives. For those terms with the derivative in regard to the z direction, author used the data he collected with the side-looking orientation. As it is mentioned before, the Nortek vectrino Profiler II measures the velocity of water for a range from 4 to 7.4 cm away from the probe. Author used the range 4.5-5.5 cm of this profile in the side-looking orientation to calculate the derivatives with regard to the z direction. Sometimes when author plotted the average turbulent parameters for the whole velocity profile that he collected by down-looking and side-looking orientation, he noticed a shift, for some parameters, between the down-looking and side-looking data. This shift could be due to the fact that when he turned the probe to the side-looking orientation, the probe stem could act like an obstacle in the flow and changed the flow conditions. Author observed the shift between the down-looking and side-looking data, mostly, in the steeper bed slope, that he had higher Reynolds numbers and more turbulent flow. Author believed that down-looking data was the corrected ones because less disturbance was in the flow (Picek 2008). Author applied a correction factor, a multiplier, to the side-looking data to remove the shift between down-looking and side-looking data. He applied the correction factors just to the

average velocities and turbulent intensities, if needed, and calculated other parameters, like TKE and anisotropy, based on the modified average velocities and turbulent intensities.

2.5 Spectral Analyses:

Author performed the spectral analysis to get a better understanding of different sized coherent structures in the flow and to investigate the ‘-1’ power law region. The following equation is the continuous Fourier transform which converts the time domain into the frequency domain,

$$F_k = \frac{1}{L} \int_0^L f(x) e^{-2\pi i k \frac{x}{L}} dx \quad (20)$$

where F_k is the frequency domain and $f(x)$ is the time domain.

Author used the discrete Fourier transform (DFT), which is defined by the following equation, to transform the time domain into the frequency domain and perform the spectral analysis,

$$X_k = \sum_{n=0}^{N-1} x_n e^{-i2\pi k \frac{n}{N}}, k = 0, \dots, N-1 \quad (21)$$

where x_n is the time series that converted to the frequency domain, X_k . For this study, x_n is the velocities data.

The transformation of the time domain into the frequency domain by performing spectral analysis is used to better understand the coherent structures in the flow. Four different regions are recognized in open channel flows with non-moving beds. The first region is related to the range of the largest eddies and has a 0 slope in power spectral density plots. The second region is related to the range of intermediate eddies, where energy production and cascade energy transfer co-exist, and follows the -1 slope in power spectral

density plots (see Figure 1.1). This region has a constant energy all over its range, from the small eddies to the large eddies. The right hand side boundary of this region is related to the bursting phenomena occurring in the flow, and the left hand side boundary of this region is related to the large eddies, with the high level of energy, known as macroturbulence. The third region, known as the inertial subrange, is related to the range of relatively small eddies where only energy transfer occurs and follows the slope of -5/3 in power spectral density plots. The last region, known as viscous subrange, is related to the range of the smallest eddies, where energy dissipates.

In order to better understand the structures in the flow, frequency values should be converted into the wave-number values. The authors used ‘Taylor’s Frozen Hypothesis’ to convert the frequencies into the wavenumbers. ‘Taylor’s Frozen Hypothesis’ is an assumption that the velocity of eddies is much smaller than the mean flow velocity, and they convect downstream by the mean flow velocity. It is believed that the wavenumbers calculated from this hypothesis deviate from the true wavenumbers as the eddies get larger, and underestimates the true wavenumbers (Kim and Adrian 1999). This deviation would not affect the energy of coherent structures in the flow but it would change the size of structures. It affects the size of macroturbulence more than the size of bursting structures. In other words, the relative size of large eddies to the small eddies gets bigger than the true value when ‘Taylor Frozen Hypothesis’ is used. At this moment, this hypothesis is the only way to convert frequencies to length scales, and future work is needed to calculate the true wavelengths for larger eddies. The author used the following equation to convert frequencies into the wavenumbers,

$$K = \frac{2\pi f}{U} \quad (22)$$

where K is the wave number, U is the average velocity, and f is the frequency.

There are different algorithms to calculate the DFT. Author developed a MATLAB code based on `pwelch` function to do the spectral analysis. `Pwelch` is a function in MATLAB that estimates the power spectral density (PSD) of a given signal using the Welch's method. Welch's method is the modified version of the periodogram method developed by P.D. Welch (Welch, 1967). In this method, the signal is segmented into different groups with the same length. It is possible for sections to overlap. Then a weighted factor (*window*) is multiplied to each data point in each segments. The Fourier transforms of each segment are calculated, and K modified periodograms, if we have k segments, are obtained. The spectral estimate is the average of these periodograms. The window function basically performs analyses upon the raw data to reduce the FFT leakage. Leakage is the information gained from spectra at the wrong frequencies. The form of `Pwelch` function we used is as follows:

$$[p_{xx}, f] = \text{pwelch}(x, \text{window}, \text{noverlap}, nfft, fs) \quad (23)$$

By default, `pwelch` divides the original signal into eight groups with 50% overlap. It uses the Hamming window by default. If an empty vector `[]` is used for $nfft$, then `pwelch` adopts the default value, which is the greater value between 256 and the next power of two greater than the length of each segment. The length of p_{xx} and f depends on $nfft$. If $nfft$ is even, then the length of p_{xx} would be equal to $nfft/2+1$. Otherwise, the length of p_{xx} would be equal to $(nfft+1)/2$. The length of f is equal to the length of p_{xx} . The units of f is Hz, and the unit of power spectral density (PSD) is power per Hz, m^2/s for our study. fs is the sampling frequency and if an empty vector `[]` is used, fs would be equal to 1 Hz by default.

We recommend to use following values for `pwelch` parameters described above.

Window Size: we decided to use 3000 for the *window size* because not only this length of *window* cover the necessary information but also make the spectral representation clearer and smoother. The *window* separates the time series into the sections in which the length of each section is equal to the length of *window*. For this study, we collected 90000 data for each point and by choosing 3000 for the *window size*, we separated our data into 30 sections. Spectral analysis was performed on each section and the average of these calculations are reported as the final result of the spectral analysis for that point.

Window Type: We also recommend to use the Hanning window because it has less leakage to the next frequencies compare with other windows like Hamming and rectangular. The Hanning window follows the following distribution:

$$\text{Hanning window} = 0.5 - 0.5\cos\left(\frac{2pn}{N}\right) \quad (24)$$

Although Hanning window has a small leakage to the next bins but its main lobe is twice as wide as the main lobe of rectangular window. In our case, we focus on studying the different regions of spectral corresponding to different frequencies. Based on this, it is much more important for us to have less leakage in other frequencies associated with their adjacent frequencies rather than a good representation of a specific frequency.

Nooverlap: We recommend to not using any overlaps since it would smooth our signals more than what is needed.

nfft: We recommend to use the default value for this parameter which is as stated above the greater value between 256 and the next power of two greater than the length of each segments.

f_s : This parameter should be your sampling frequency which in our case is 50 Hz.

We could either plot the spectral values in the power spectral density form or variance preserving form. If we plot the outputs of pwelch function (pxx, f) in a log-log scale, we would get the power spectral density form. If we multiply the outputs of pwelch function, the spectra and frequency values, and then plot the new values vs frequency values in a semi-logarithmic plot, we would get the variance preserving form. The vertical axis in the variance preserving form shows the energy of structures in the flow while the vertical axis in the power spectral density form shows the energy density of structures in the flow. In order to gain more information from the spectra plots about the different structures in the flow, we preferred to use the wave number values instead of frequency values for both the traditional and variance preserving forms. The wave numbers can be calculated by the equation 20.

We smoothed our spectral data with a function, ‘fastsmooth’, written in MATLAB. This function applies the low pass filtering to smooth the data. The form of this function is shown below:

$$yy = \text{fastsmooth}(pxx, width, type) \quad (25)$$

where pxx is the spectral results acquired from pwelch function, $width$ is the smooth width and $type$ determines the smoothing type. Three smoothing types are provided in ‘fastsmooth’ function which are described below:

- *Type 1*: This $type$ gives a rectangular moving average. For example for 3-point smoothing, $w = 3$, it gives the following value for the point j

$$S_j = \frac{Y_{j-1} + Y_j + Y_{j+1}}{3} \quad (26)$$

- *Type 2*: This *type* gives a triangular moving average. It is like rectangular smoothing which applied two times into the signal. In other words, if we apply *type 1* smoothing into the signals and then again apply *type 1* smoothing into the smooth signal, the results would be equal to the results of *type 2* smoothing or triangular smoothing. For example for 3-point smoothing, it gives the following value for point j :

$$S_j = \frac{Y_{j-2} + 2Y_{j-1} + 3Y_j + 2Y_{j+1} + Y_{j+2}}{9} \quad (27)$$

- *Type 3*: This *type* gives a pseudo-Gaussian smoothing data which is equivalent to the rectangular smoothing that applied three times into the signal. For example, for 3-point smoothing, it gives the following value for point j :

$$S_j = \frac{Y_{j-3} + 3Y_{j-2} + 6Y_{j-1} + 7Y_j + 6Y_{j+1} + 3Y_{j+2} + Y_{j+3}}{27} \quad (28)$$

We used *type 3* in ‘fastsmoothing’ function with $w=10$ to smooth the spectral results.

We performed smoothing sensitivity to investigate the effect of the smoothing by this function on the spectral values. We will show the results in the section 3.

2.6 Spectral scaling:

In this study, we used different spectral scaling methods from the literature and we developed a new scaling method based on the equilibrium boundary layer assumption. We used Nikora spectra scaling method stemmed from the work of Perry (Nikora 2005, Nikora and Goring 2000, Perry and Chong 1982, Perry and Abell). In this method, they used friction velocity as a scaling parameters for spectral energy density and also, they scaled the length scale of small eddies with y , distance from the bed. Their justification to scale the length of eddies with inner variable y , was based on the fact that at a distance y from the bed, detected small eddies have a length equal to the distance from the bed. They believe it is not possible to detect eddies by the probe if they have a smaller length scales from the distance from the bed and if they have a bigger length scale, then they are not the smallest eddies. This scaling has the following form (Perry and Chong 1982):

$$S(k_1 y)/u^{*2} = f(k_1 y) \quad (29)$$

which can be rewritten in the following form (Nikora 2005, Nikora and Goring 2000):

$$US(f) = C y u^{*2} \quad (30)$$

where k_1 is the wavenumber ($k_1 = f/U$), y is the distance from the bed, f is the frequency, u^* is the friction velocity and C is a constant.

We used this scaling method to scale our spectral plots in both outer and inner regions.

Another scaling method which was used in this study, was the scaling method Kim and Adrian used in their paper (Kim and Adrian 1998). In this method, they scaled the energy of structures with the friction velocity. They scaled the length of eddies with y for inner

region and H for outer region. This scaling method is the same as Perry or Nikora's scaling method and is shown below:

$$KS(K) = Cu^{*2} \quad (31)$$

In this study, we carried out 11 tests to investigate if the energy of structures in the flow is related to other parameters besides the friction velocity. We considered the equilibrium boundary layer theory for outer region to scale the energy of structures with new parameters. We assumed the energy of eddies in the streamwise direction is related to the velocity fluctuations or turbulent intensities and developed the following scaling method:

$$KS(K) = C(\exp(-\frac{y}{H})u^*)^2 \quad (32)$$

This scaling method stemmed from the work of Nezu and Nakagavaw. Nezu and Nakagavaw (1993) developed an equation, by assuming the equilibrium boundary layer theory, for turbulent intensity. They applied the $k-\epsilon$ turbulence model to open-channel flows by neglecting the viscous diffusion term to derive the following equation:

$$G = \epsilon + \frac{d}{dy} \left(\frac{V_t}{\sigma_k} \frac{dk}{dy} \right) \quad (33)$$

where V_t is the eddy viscosity. The second term in RHS of equation above are related to the turbulent diffusion. σ_k is equal to 1 in the standard $k-\epsilon$ turbulence model.

They assume equilibrium boundary layer where energy production is equal to energy dissipation to conclude the term in the parentheses in equation (33) is constant. Consequently, they conclude the following equation by approximate eddy viscosity by

$$\left(\frac{U_*^2}{\kappa} \right) (u_* h):$$

$$\left(\frac{1}{\kappa}\right) \left(\frac{d\kappa}{d\xi}\right) = \text{const} \equiv -2C_k \quad (34)$$

where C_k is a constant and $\xi = y/h$. We can rearrange the equation above to the following form:

$$\left(\frac{d\kappa}{\kappa}\right) = -2C_k d\xi \quad (35)$$

If we integrate the equation above and applying the boundary conditions, the following equation can be yielded:

$$\frac{\kappa}{u_*^2} = D \exp(-2C_k \xi) \quad (36)$$

The equation above can be used to yield the following equation which is the base for the proposed scaling method in this study.

$$\frac{w'}{U_*} = D_u \exp(-C_k \xi) \quad (37)$$

CHAPTER 2 TABLES AND FIGURES

Table 2.1. Experimental tests conditions for small flume.

Run	S	k_s (m)	Q ($\frac{m^3}{s}$)	ρ ($\frac{kg}{m^3}$)	B (m)	g ($\frac{m^2}{s}$)	u^* ($\frac{m}{s}$)	H (m)	y (m)	B/H	H/k_s	$Re(\times 10^4)$	K^+	Fr	$\mu (\times 10^{-3})$
1	0.0002	0.0112	0.021	998.23	0.61	9.81	0.0122	0.1	0.001-0.08	6.10	8.93	2.6	67.78	0.35	1.002
2	0.0002	0.0112	0.046	998.23	0.61	9.81	0.0135	0.133	0.001-0.11	4.59	11.87	5.3	75.20	0.50	1.002
3	0.0002	0.0112	0.068	998.23	0.61	9.81	0.0146	0.167	0.001-0.147	3.65	14.91	7.2	81.17	0.52	1.002
4	0.0002	0.0112	0.085	998.23	0.61	9.81	0.0154	0.2	0.001-0.13	3.05	17.86	8.4	85.92	0.50	1.002
5	0.0017	0.0112	0.038	998.23	0.61	9.81	0.0354	0.1	0.001-0.08	6.1	8.93	4.7	197.49	0.64	1.002
6	0.0017	0.0112	0.062	998.23	0.61	9.81	0.0393	0.133	0.001-0.11	4.59	11.87	7.0	219.25	0.67	1.002
7	0.0017	0.0112	0.092	998.23	0.61	9.81	0.0424	0.167	0.001-0.147	3.65	14.91	9.7	236.55	0.70	1.002
8	0.0017	0.0112	0.12	998.23	0.61	9.81	0.0449	0.2	0.001-0.18	3.05	17.86	12.2	250.38	0.72	1.002
9	0.006	0.0112	0.057	998.23	0.61	9.81	0.0666	0.1	0.001-0.08	6.1	8.93	7.1	371.45	0.95	1.002
10	0.006	0.0112	0.085	998.23	0.61	9.81	0.0738	0.133	0.001-0.11	4.59	11.87	9.7	411.89	0.92	1.002
11	0.006	0.0112	0.120	998.23	0.61	9.81	0.0843	0.167	0.001-0.147	3.65	14.91	12.7	470.30	0.92	1.002

Figure 2.1. Experimental setup for the small flume



Chapter 3 Results for the Small Flume:

3.1 Validating Turbulence Data, Time-Average Parameters and Secondary Currents:

It is recognized that the uniform, turbulent open channel flow over gravel conditions for which we are investigating have a number of well-defined mean characteristics including, a near logarithmic distribution of the streamwise velocity in the vertical, or a slight modification thereof, a near-linear distribution of the primary Reynolds shear stress for the outer region, weak exponential decay of the Reynolds normal stresses with depth, and weak secondary motion indicated by weak but non-zero mean vertical and mean transverse velocities and the presence of anisotropy away from the wall (Nezu and Nakagawa 1993). Therefore, the time-average parameters were investigated with respect to previous literature results to validate the quality of the turbulence data.

In order to check the quality of our data, the first step was to estimate the friction velocity. We used three different methods to calculate the friction velocity (Nezu and Nakagawa 1993, Pons 2007). In the first method, we used the following equation to calculate the friction velocity where the friction velocity is estimated via the momentum equation for one dimensional, steady flow (Jain equation in sediment transport technology book).

$$u^* = \sqrt{gRS} \quad (38)$$

where R is the hydraulic radius, S is the slope and g is the gravitational acceleration. This method is the easiest way to calculate the friction velocity. The second way to calculate the friction velocity is to fitting a line to the log-layer of the velocity profile and estimate the friction velocity. In order to do this, we first found the logarithmic layer of the velocity

profile. If we plot $u^+ = u/u^*$ vs $y^+ = \frac{yu^*}{\nu}$ in a semi logarithmic scale, the log-layer would be linear. After we found the log-layer, we used our data and the following equation to fit a line and estimate the friction velocity.

$$\frac{U}{u^*} = \frac{1}{\kappa} \ln \left(\frac{y}{k_s} \right) + 8.5 \quad (39)$$

where κ is the von Karman constant and is equal to 0.41. k_s is the equivalent roughness height and is equal to $2D_{84}$. The third method to calculate the friction velocity is to use the primary Reynolds stress. In this method we used our primary Reynolds stress data ($-\overline{u'v'}$) and the following equation to fit a line and calculate the friction velocity.

$$-\overline{u'v'} = u^{*2} \left(1 - \frac{y}{h} \right) \quad (40)$$

The results of friction velocity estimated from these three method are shown in Table 3.1 and Figure 3.1. As it is shown friction velocity has different values when calculated from different methods and our results are in agreement with other studies where different values for friction velocities are reported (Pons 2007, Kendall 2006). The first method is the easiest way to calculate the friction velocity but it does not count for the spatial variation in resistance near the bed and when the channel slope is so small it underestimates the friction velocity significantly. The second method was introduced by Clauser (1956) to account for the spatial variation in resistance near the bed. Using this method depend on assuming a constant for κ , von Karman constant, which different values are reported for this constant in literature for different conditions. For example for the clean water, κ is equal to 0.41, the value we used in this study, but for the heavily sediment water, it is equal to 0.2 (Cui 2011; Zanoun 2003). This problem causes the friction velocity estimated by the Clauser method to not be reliable and mostly it overestimate the true value for the

friction velocity (Kendall and Koochesfahani, 2006). The authors preferred to use the third method to estimate the friction velocity, as recommended by Nezu and Nakagawa (1993), because it does not suffer from the other two methods' problems and also 'Primary Reynolds stress' is a turbulence quantity (Nezu and Nakagawa 1993). The only requirement for this method is the ability to measure two dimensional flow velocities, which was accomplished with our ADV.

We scaled time-average turbulent parameters with inner and outer variables to not only validate the quality of our data with the laws developed for the same condition but also understand better the behavior of the flow described by these parameters. In the first step, we scaled the stream-wise velocity with inner and outer variables as shown in Figure 3.3. Scaling the stream-wise velocity with the friction velocity, which is an inner variable, would cause the non-scaling stream-wise velocity to collapse on each other as shown in Figures (3.3 a) and (3.3 b). This result was expected due to the fact that all our velocity profiles follow nicely the law developed for the hydraulically rough flows. This law is shown below:

$$\frac{U}{u^*} = \frac{1}{\kappa} \ln\left(\frac{y}{k_s}\right) + b + \frac{2\Pi}{\kappa} \sin^2\left(\frac{\pi y}{2H}\right) \quad (41)$$

where u^* is the friction velocity that can be calculated in three ways as described above. For this comparison we used the friction velocity and we calculated using the log-layer of the velocity profile. κ is the von Karman constant and is equal to 0.41. k_s is the equivalent roughness height and is equal to $2D_{84}$. For flume the flume with the small roughness height, this was equal to 1.14 cm. b is equal to 8.5 for hydraulically rough conditions. Π is the wake parameter. The last term in the equation above is added to consider the wake. We noticed that most of our data do not have a wake and in those profiles that we noticed a

weak wake, the wake parameter, Π , was equal to 0.23 approximately. This fact that we had no wake or small wake would lead to use the following equation instead of equation (32) for the small flume.

$$\frac{U}{u^*} = \frac{1}{\kappa} \ln \left(\frac{y}{k_s} \right) + b \quad . \quad (42)$$

Since κ , k_s and b were constant for the small flume, scaling the stream-wise velocity with friction velocity would remove the variations in non-scaling velocity profiles.

We also used outer and mixed variables to scale the stream-wise velocity as shown in Figures (3.3 c) and (3.3 d). Our purpose to perform these scaling was to check if the outer region, far away from the bed, is dependent on outer variables or the mixed variables. Based on the equilibrium turbulent boundary layer which was suggested by George and Castillo (1997) and investigated more by Belcher and Fox (2010), the velocity profile can scale by outer variables as follows:

$$(U_{max} - U)/U_{max} \quad (43)$$

Based on this theory, in the equilibrium condition all velocity profiles and turbulent length scales maintain the same x dependence. The results for this scaling is shown in Figure (3.3 c). Also, we scaled velocity profiles with mixed variables with the following equation to check if the inner variables affect the outer region.

$$(U_{max} - U)/u^* \quad (44)$$

The results for the mixed variables are shown in Figure (3.3 d).

In the next step, we scaled the primary Reynolds stress and streamwise Reynolds normal stress with inner and outer variables. First we scaled primary Reynolds stress with friction velocity estimated by the third method, the one that estimates friction velocity by using primary Reynolds stress data. The results for this scaling is shown in Figure (3.4 a).

Then we compare the scaled primary Reynolds stress with the law developed for these conditions as follows:

$$-\overline{u'v'} = u^{*2} \left(1 - \frac{y}{h}\right) \quad (45)$$

This equation is for uniform open channel flow and derived from the combination of Navier-Stokes equations. (Nezu and Nakagawa, 1993). As shown in Figure (3.4 a), primary Reynolds stress attained its maximum value at approximately $y/H = 0.2$ for all cases.

Next, we scaled the streamwise Reynolds normal stress with inner and outer variables as shown in Figures (3.4 a-f). First we scaled the streamwise Reynolds normal stress with different friction velocities estimated by different methods and compared the results to law developed for turbulent intensities as follows:

$$\frac{RMS(u')}{u^*} = D_u \exp\left(\frac{-y}{H}\right) \quad (46)$$

where D_u is an empirical coefficient. In each scaling we used a fitting line to find the coefficient. D_u varies between 2 to 4.6, depending on the friction velocity we used. Streamwise Reynolds normal stress is a turbulence quantity and the best friction velocity that could be used to scale the $RMSu$ was the one estimated by the third method. Our results which are shown in Figure 3.4 support this idea. We also scaled $RMSu$ with U and U_{max} and the results are shown in figure (3.4 e, 3.4 f).

$$\frac{RMS(u')}{\bar{U}} = D_u \exp\left(\frac{-y}{H}\right) \quad (47)$$

$$\frac{RMS(u')}{U_{max}} = D_u \exp\left(\frac{-y}{H}\right) \quad (48)$$

The empirical coefficients for these scaling were 1.93 and 0.14 respectively. As shown in figure (3.4 c and f), $RMSu$ scaled better with inner variables (u^*) than outer variables (U_{max}).

We plotted the secondary velocities without scaling in Figure 3.5. These velocities are related to the secondary currents in the flow. We used the vertical average velocity to calculate some of the energy terms in equations 16,17,18. Finally we scaled four other turbulent parameters with friction velocity calculated by fitting a line to the primary Reynolds stress data. These results are shown in Figure 3.6. For the secondary Reynolds stresses, RMS_v and RMS_w , we compared the scaled results to the law suggested by Nezu and Nakagawa as follows:

$$\frac{RMS(v')}{u^*} = D_v \exp\left(\frac{-y}{H}\right) \quad (49)$$

$$\frac{RMS(w')}{u^*} = D_w \exp\left(\frac{-y}{H}\right) \quad (50)$$

We used the scaled secondary Reynolds stress and fit a line to find the empirical coefficients, D_v and D_w . These coefficients were found to be 1.22 and 1.75 respectively. Using friction velocity as a scaling parameters reduced the variation in distribution of secondary Reynolds stresses and the data to collapse on each other except for test 11. As shown in figure 3.6c and 3.6d, TKE and anisotropy were scaled nicely with friction velocity.

3.2 Selecting Wavenumbers for Macroturbulence and Bursting:

After post-processing and validating the turbulence dataset and its time-average parameters, emphasis was placed upon the sensitivity and selection of K_m and K_b and a classifications of the -1 power region were observed. The original power spectra plots were used for visualization of the -1 region. Also, authors used a smoothing function, 'fastsmooth' function, to smooth the original power spectra plots for visualization of the

region. An example of the original and smoothed spectra plots in both the power spectral density and variance preserving form are shown in Figure 3.7 for identifying K_m and Figure 3.8 for identifying K_b .

After extensive investigation, the authors found that it was best to use the four plotting methods together as shown in Figure 3.7 to identify K_m , and similarly for identifying K_b . As it is clear from the non-smoothed plots (Figures 3.7a and 3.7b), there are so many spikes in the second region in the variance preserving form. The authors removed these spikes by using the ‘fastsmooth’ function with *type 3* and $w=10$. Also, we can notice that S_m in the non-smoothed plots in the variance preserving form has approximately the same values as the average of the second region energy values. This is why authors believe S_m in the smoothed plot is a very good representation of the true S_m because energy values in the smoothed plots are obtained after applying the moving average filtering to the energy values in the non-smoothed plots. The authors also believe S_b in the smoothed plots is the representation of the true S_b . Sometimes, K_m in the smoothed plots is a very good representation of true K_m in the non-smoothed plots. But often, the lower value for K_m existed for the smoothed plots. This is important to note because as shown in Figure 3.7b, the K_m value will fall away from the -1 power region if smoothing is used. Therefore, the researcher has the potential to mis-label the location of K_m .

Also, smoothing can cause K_b to have smaller value than the true K_b as shown in Figure 3.8. As it is mentioned above, smoothing is performed by using moving average filtering. This filtering replace the energy value for a point by its adjacent points energy values. This causes the true K_b to have smaller energy value in the smoothed plots because

the energy values just before the true K_b in the non-smoothed plots are almost constant while the energy values after the true K_b in the non-smoothed plots are decreased. Therefore, the researcher has the potential to mis-label the location of K_b if not considering the non-smoothed plots besides the smoothed ones in K_b identification.

We applied the above method, and we consider all four plots, power spectral density and variance preserving form in smoothed and non-smoothed plots, to better estimate K_m , K_b , S_m and S_b . The method was performed for all data. In this study, we selected K_m and K_b from the smoothed plots by considering the non-smoothed plots. We selected S_m and S_b from the non-smoothed plots by considering the selected K_m and K_b .

There have been a lot of works done to determine the number of required data should be collected that can interpret reliable facts about the coherent motions in the flow. In this study, author performed sensitivity analysis to investigate adequate number of data should be collected to get reliable value for the wavenumbers and energies of macroturbulence and bursting motions. Author collected 90000 data for each point with a sampling frequency of 50 Hz to study and analyze large scale and smaller scale motions. He identified the wavenumbers and energies of macroturbulence and bursting structures by the method explained above. Then, he applied the same method for smaller number of data to determine the minimum number of data that give the same values for the wavenumber and energy of macroturbulence and bursting structures. As it is shown in table 3.2 or figure 3.9 authors found that about 7 minutes (20000 data in this study) of data collection for smaller scale motions and about 17 minutes (50000 data in this study) of data collection for large scale motions are needed to get a reliable value with the maximum 5 percent error.

3.3 Existence and Non-Existence of the Spectral Production Region:

Existence or non-existence of the -1 power region was investigated. About 15% of the points collected did not contain a -1 power region (see Figure 3.10). These were for the weakest apparent production and transport, as inferred by the high flow depth and lower energy gradients. For example, we noticed the non-existence of -1 power region for some points in 5 tests out of 11 tests shown in table 2.1. These points were located in the outer region of those 5 tests where the energy gradients are low. For example, there were no -1 power region for $y = 14$ cm and 14.7 cm in test 7 or $y = 8, 9.1, 9.5, 12, 14$ and 14.7 cm in test 3. The reason for the non-existence of -1 power region in these cases may be explained by the lower energy gradients and relatively stronger secondary motions that transfer the energy.

3.4 Scaling of the Wavenumbers and Energy for Macroturbulence, Bursting and the -1 Power Region Plots:

We scaled the wavenumber or length scale of macroturbulence and bursting with outer, H , and inner, y , variables. These scaling are shown in figure 3.11. As it is shown in figure 3.11, k_b scaled nicely with inner variables while it is better to use outer variables to scale k_m . In general, for the regions close to the bed, it is better to use inner variables to scale both the macroturbulence and bursting length scale while in the regions close to the surface, these lengths scale better with outer variables.

Figure 3.12. shows the energy spectral of macroturbulence and bursting structures with inner and outer variables. Figure 3.12a shows the non-scaling of the energy spectral

for all 11 tests. In figure 3.12b, Kim and Adrian method (1999) is applied to scale the energy spectra of macroturbulence and bursting. This method uses the friction velocity as an inner variable to scale the energy of structures. This method is like the Nikora's method used by Nikora in his paper (Nikora 2005). Nikora method is in power spectral density form. Kim and Adrian method is in variance preserving form and this method is used here to be consistent with other scaling method in this study. In figure 3.12c, we used $RMSu^2$ as a scaling parameter. We used this scaling method because we believed the energy of the structures in the streamwise direction are related to the velocity fluctuations in this direction. In figure 3.12d, we used equation 37 to relate the $RMSu$ to the flow parameters and modify the scaling method in figure 3.12d.

In order to better visualize the scaling effect on the wavenumber and energy of macroturbulence and bursting structures, we showed the variance preserving spectral plots for different scaling parameters for all 11 tests in figures 3.13 and 3.14. In figure 3.13, we used inner variable, y , to scale the wavenumber of spectral plots for $y/H \leq 0.1$ because we believed, from figure 3.11, the structure length scales or the wavenumbers of macroturbulence and bursting scale best with y in the regions close to the bed. We scaled the energy of the spectral plots with the parameters described above except we did not use $RMSu$ as a scaling parameter and instead we used equation 37 to scale the energy values. As it is shown in figure 3.13, both Kim and Adrian method and our method work best for scaling the energy of structures in the inner region (figure 3.13b and c).

In figure 3.14, we used the same scaling parameters to scale the energy of structures for $y/H > 0.1$. In this figure, we used the outer variable, H , to scale the wavenumber of

macroturbulence or bursting structures. As it is shown in this figure, our new method (figure 3.14c) works best for scaling the energy of structures in $y/H > 0.1$.

CHAPTER 3 TABLES AND FIGURES

Table 3.1. Results of the friction velocity estimated from the different methods.

Test	S	H (m)	$u^* = \sqrt{gRS} \left(\frac{m}{s}\right)$	u^* using log-law $\left(\frac{m}{s}\right)$	u^* using Reynolds Stress $\left(\frac{m}{s}\right)$
1	0.0002	0.1	0.01215	0.0322	0.0223
2	0.0002	0.133	0.01348	0.052	0.0387
3	0.0002	0.167	0.01455	0.0529	0.0424
4	0.0002	0.2	0.0154	0.0564	0.0469
5	0.0017	0.1	0.0354	0.063	0.048
6	0.0017	0.133	0.0393	0.0693	0.0557
7	0.0017	0.167	0.0424	0.0555	0.06
8	0.0017	0.2	0.04488	0.1092	0.0735
9	0.006	0.1	0.06658	0.1158	0.0841
10	0.006	0.133	0.07383	0.1027	0.0812
11	0.006	0.167	0.0843	0.1092	0.0922

Table 3.2. Sensitivity of macroturbulence and bursting wavenumber and energy to the number of data collected.

Number of data	K_m	K_b	$K_m S_m$	$K_b S_b$
90000	3.745	21	0.009076	0.008998
1000	30.32	69.86	0.007364	0.006215
2000	n/a	n/a	n/a	n/a
3000	n/a	n/a	n/a	n/a
4000	14.27	22.05	0.007925	0.007768
5000	14.14	23.14	0.007431	0.007386
6000	14.21	24.54	0.007315	0.007349
7000	14.2	24.53	0.00722	0.007248
8000	7.101	17.43	0.008244	0.00808
9000	7.772	16.19	0.008416	0.008272
10000	9.702	16.82	0.008764	0.008298
20000	6.162	20.43	0.008671	0.008175
30000	6.166	20.45	0.008511	0.008145
40000	4.385	20.3	0.008539	0.008268
50000	3.9	21.45	0.008451	0.00833
60000	3.911	21.02	0.008467	0.008308
70000	3.746	21.09	0.009072	0.008555
80000	3.745	20.84	0.009099	0.008799

Figure 3.1. Comparison of the friction velocity from the three methods. (a) Comparison of second and third method. (b) Comparison of first and second method. (c) Comparison of first and third method

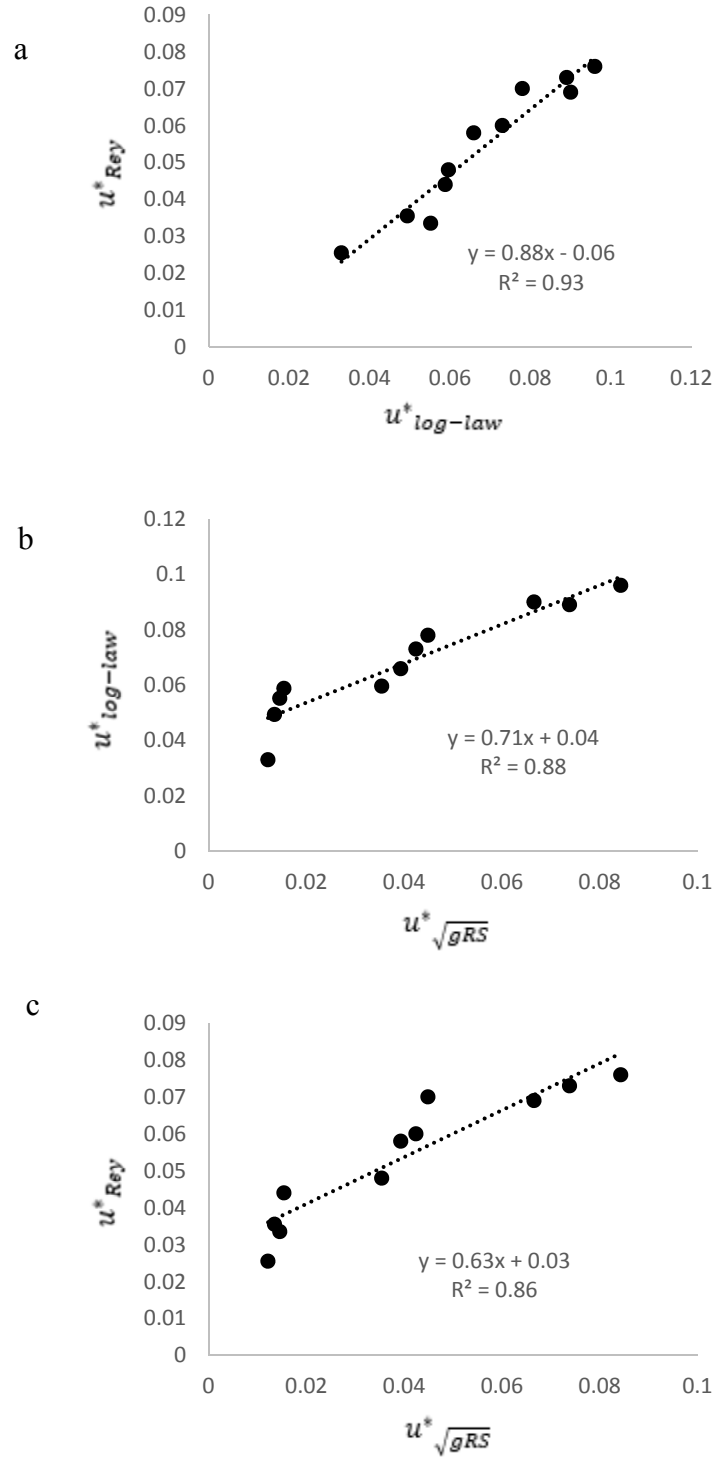


Figure 3.2. Example of parameter fitting to estimate the friction velocity for test 7. (a) shows the linear region identified for fitting the friction velocity via the logarithmic law. (b) shows an example of log law fitting. (c) shows fitting of the friction velocity using the primary Reynolds stress.

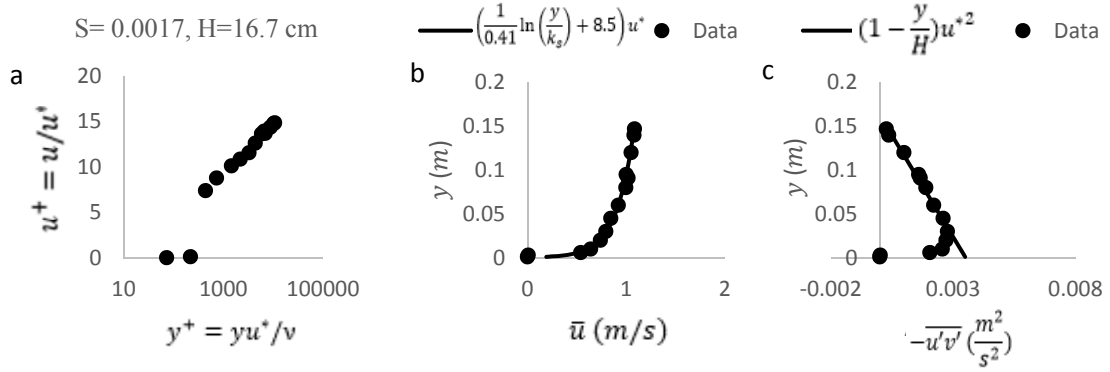


Figure 3.3. Streamwise velocity distributions for the datasets including: (a) no scaling (b) inner scaling and the law of the wall, (c) outer scaling with the freestream velocity and (d) outer scaling with the friction velocity.

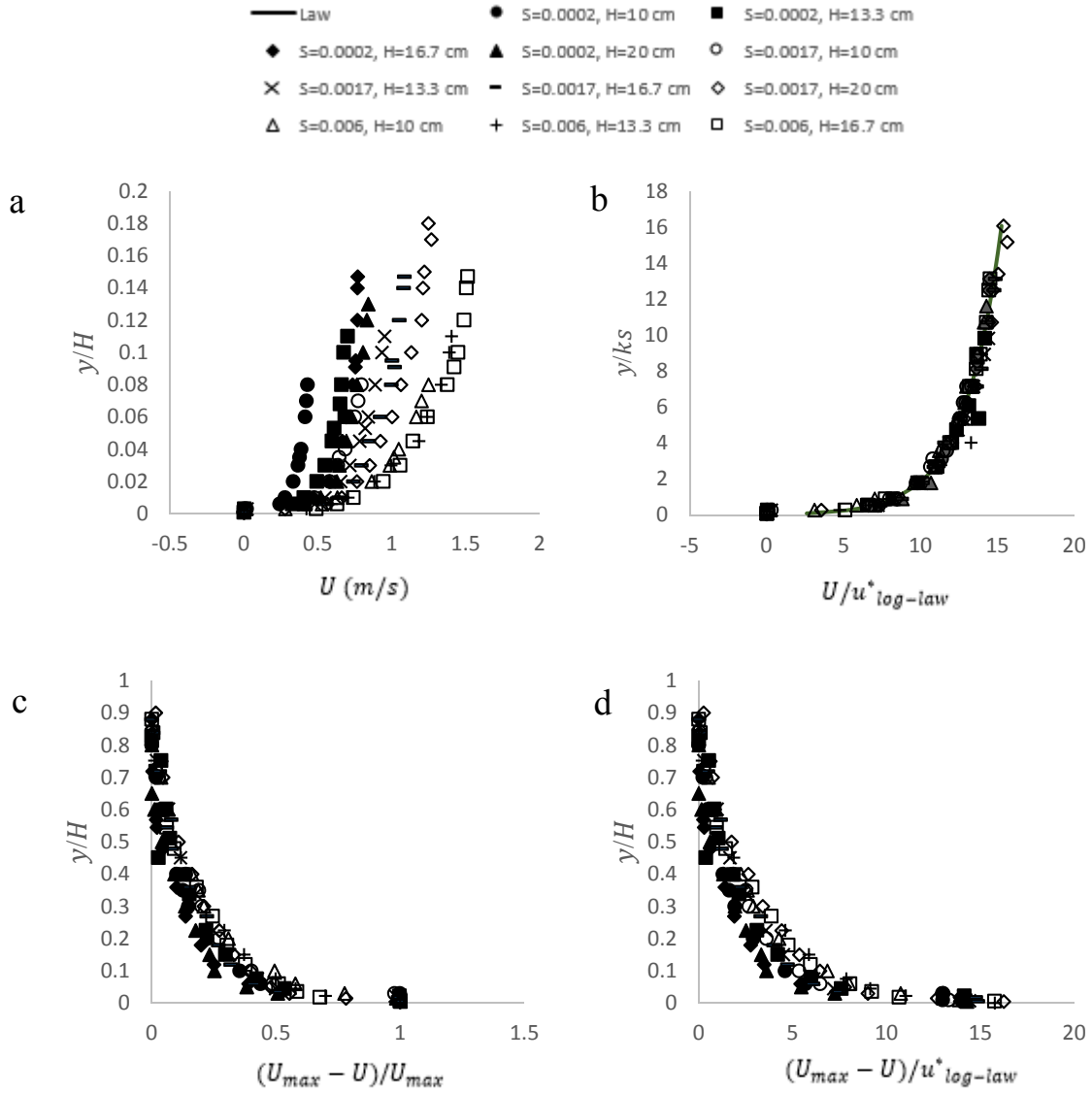


Figure 3.4. (a) Primary Reynolds shear stress and (b-f) streamwise Reynolds normal stress scaled with (b) the friction velocity estimated from the logarithmic law method, (c) the friction velocity estimated from the Reynolds shear stress data, (d) the friction equal to \sqrt{gRS} , (e) average streamwise velocity, (f) maximum streamwise velocity

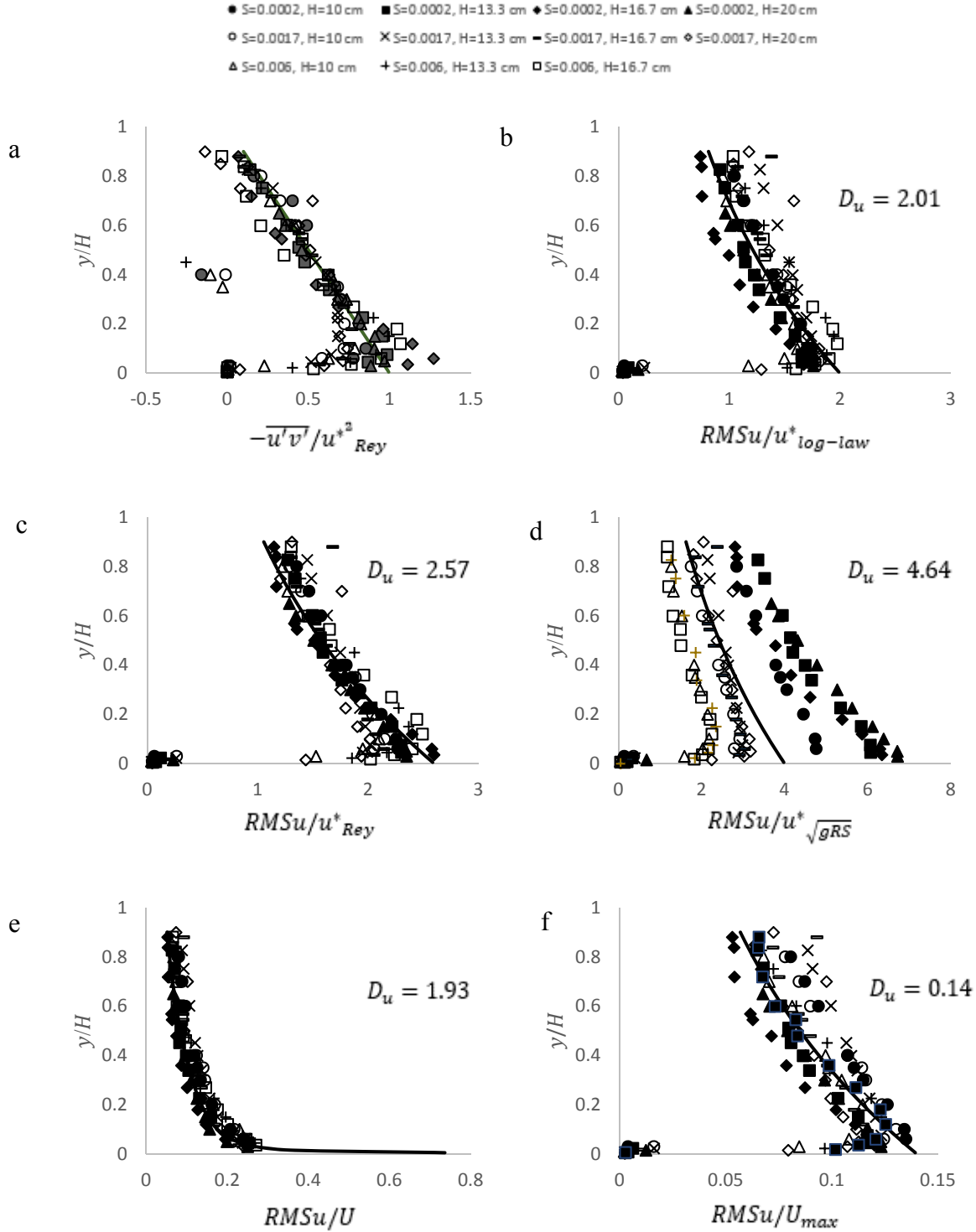


Figure 3.5. Secondary velocities. (a) vertical velocity, (b) lateral velocity

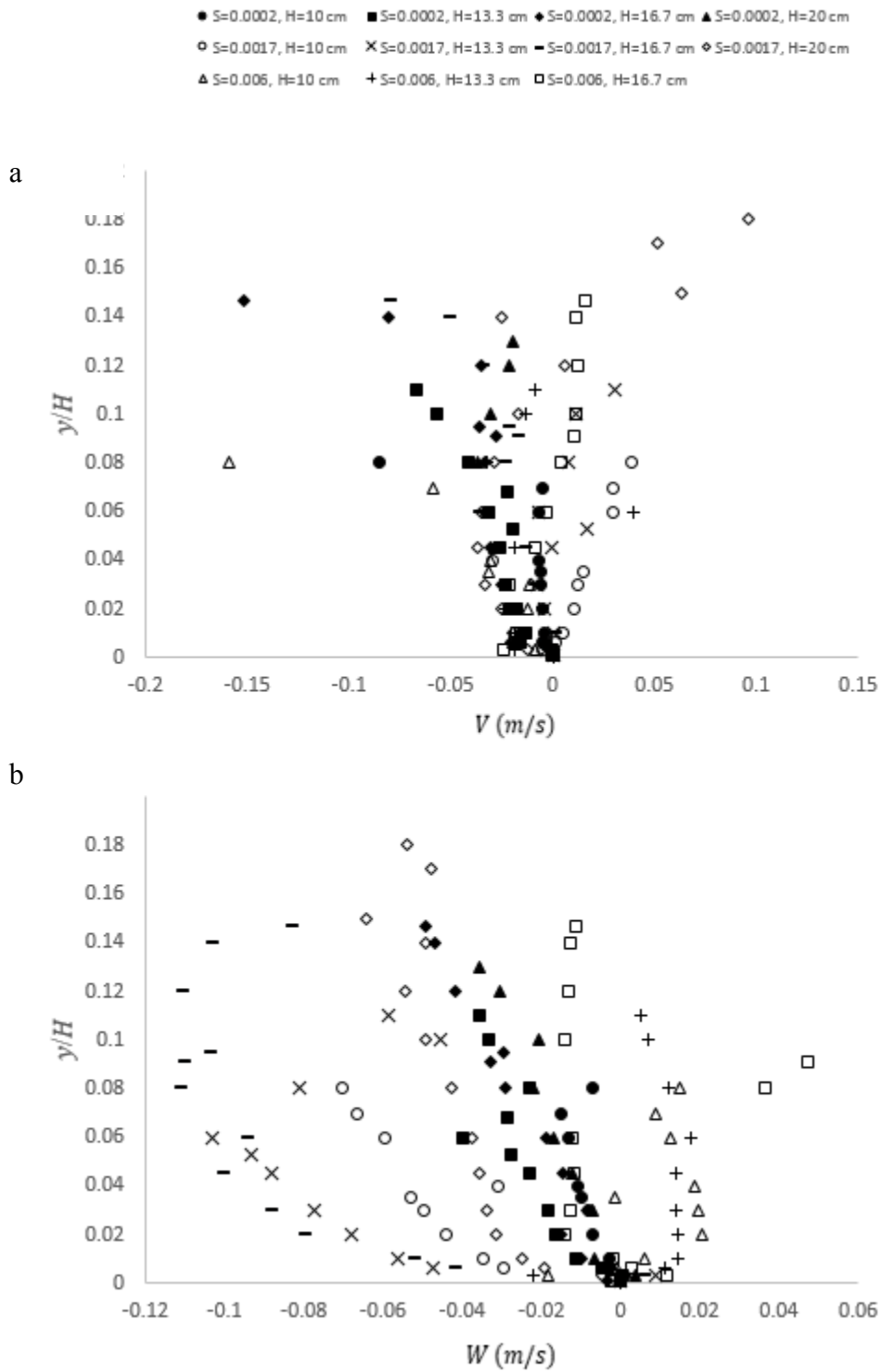


Figure 3.6. (a, b) Secondary Reynolds normal stresses (v, w) scaled with the friction velocity estimated via the primary Reynolds stress method and the exponential law plotted for the secondary terms; (c) turbulent kinetic energy normalized with friction velocity squared, and (d) anisotropy normalized with friction velocity squared.

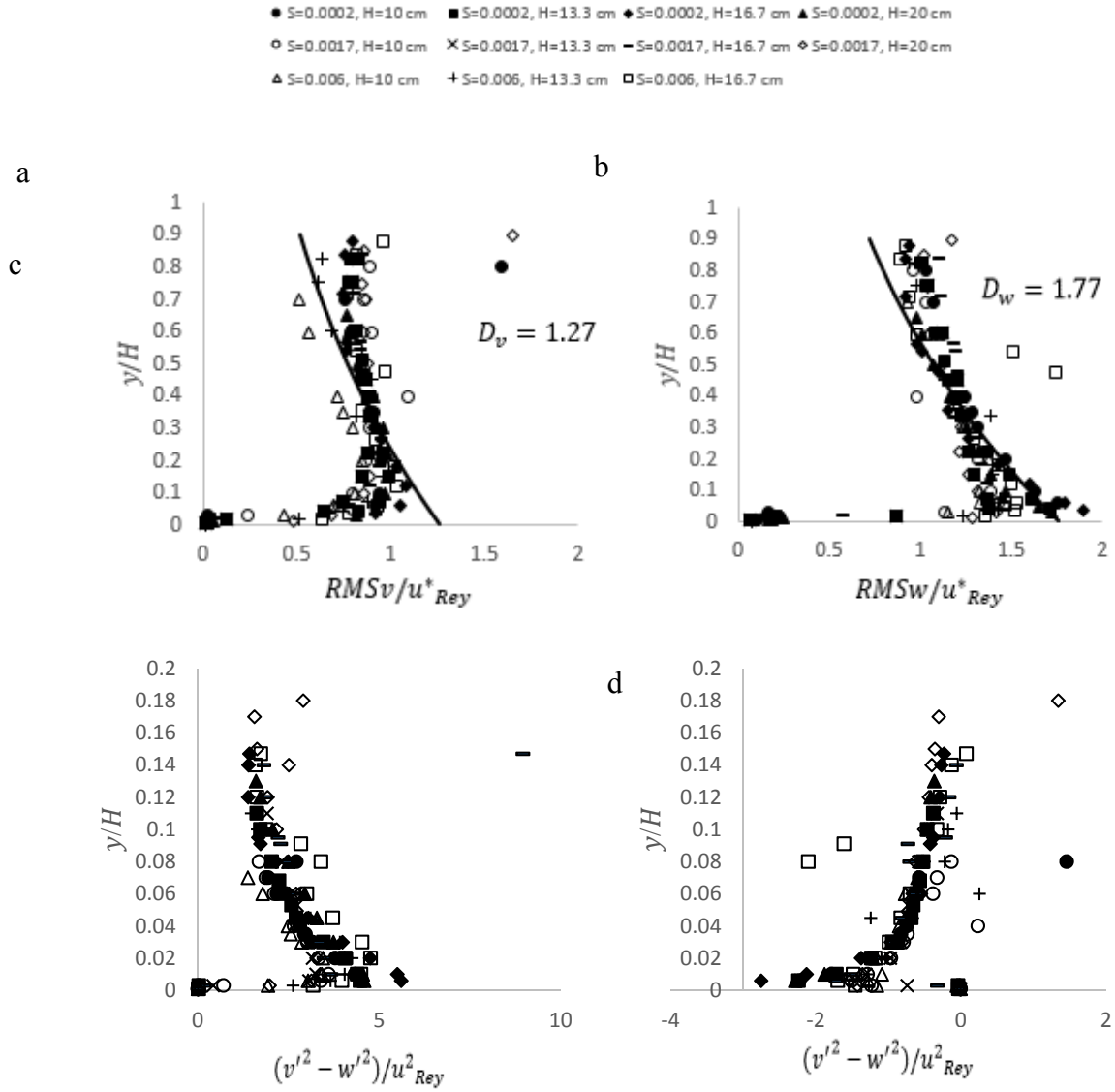


Figure 3.7. Method for identification of k_m

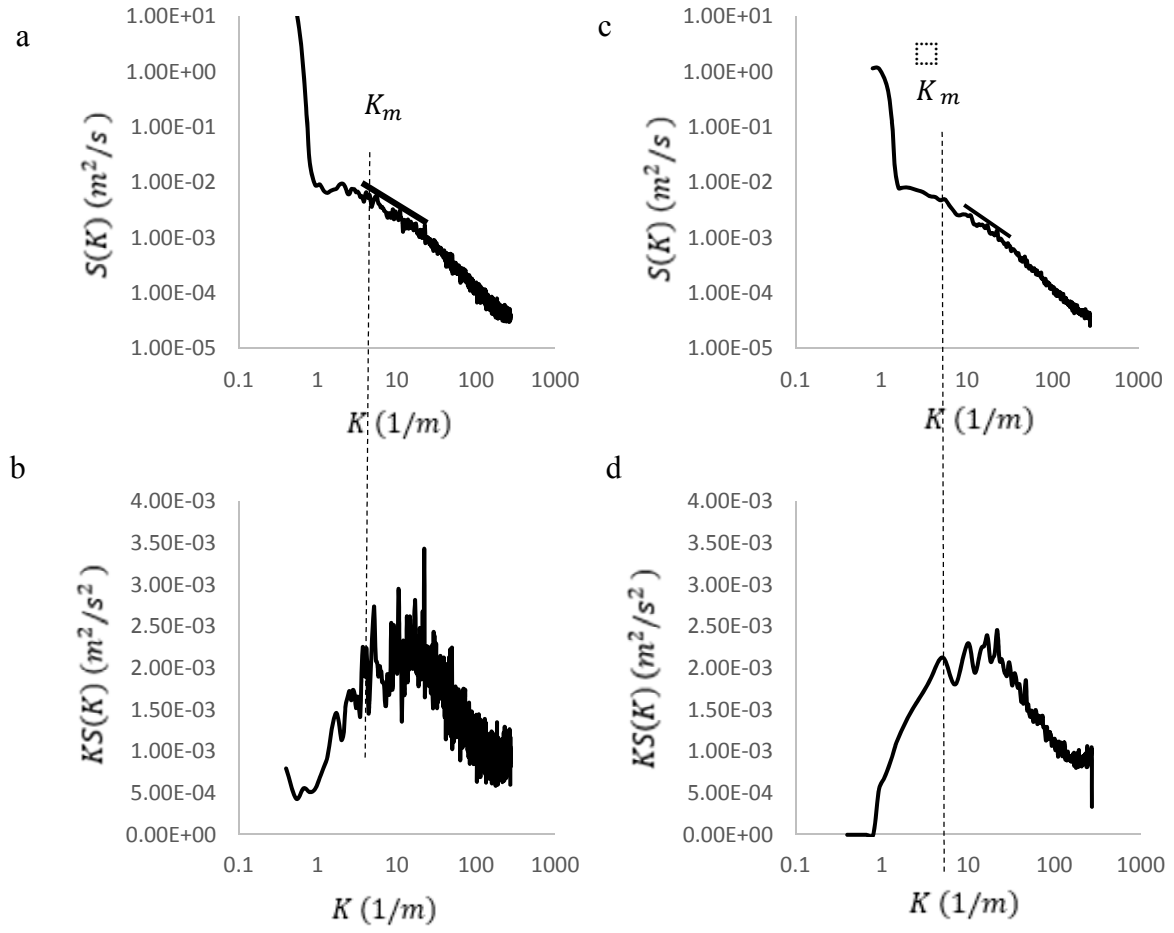


Figure 3.8. Method for identification of k_b

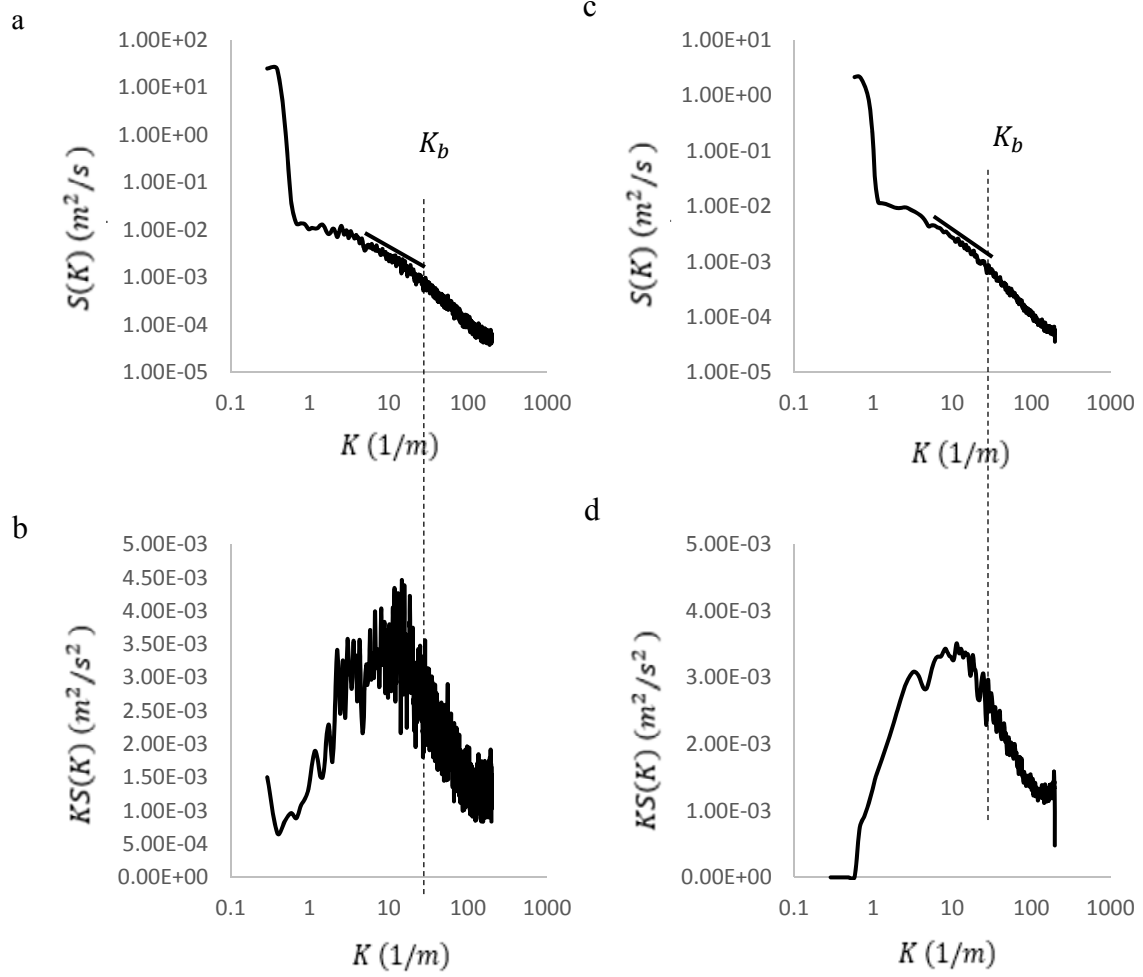
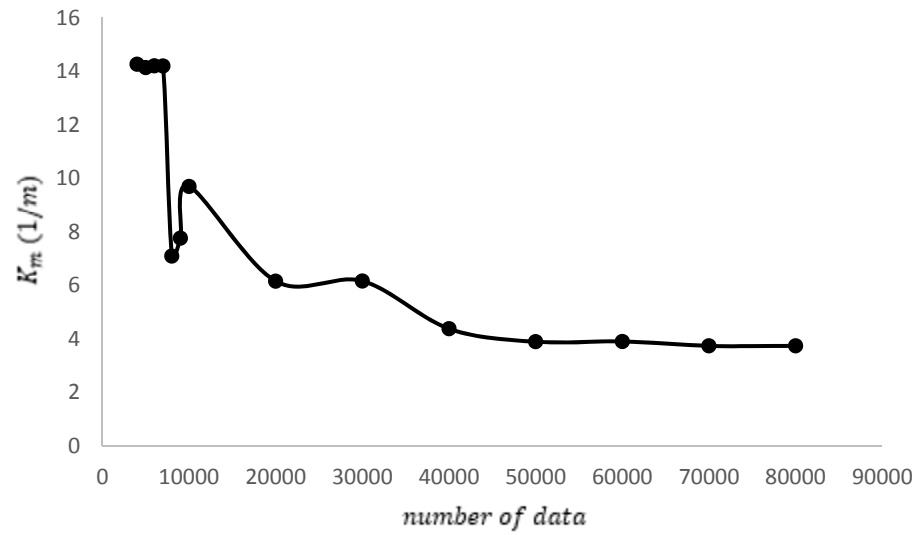


Figure 3.9. Sensitivity analysis about the number of data required to get reliable information about macroturbulenc and bursting structures. (a) analysis for macroturbulence, (b) analysis for bursting

a



b

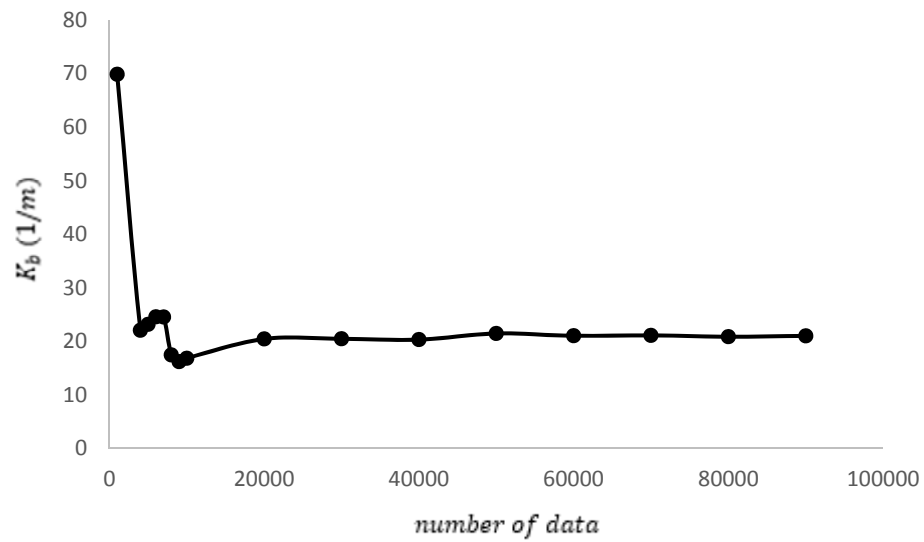


Figure 3.10. Example of spectral results showing no -1 power region.

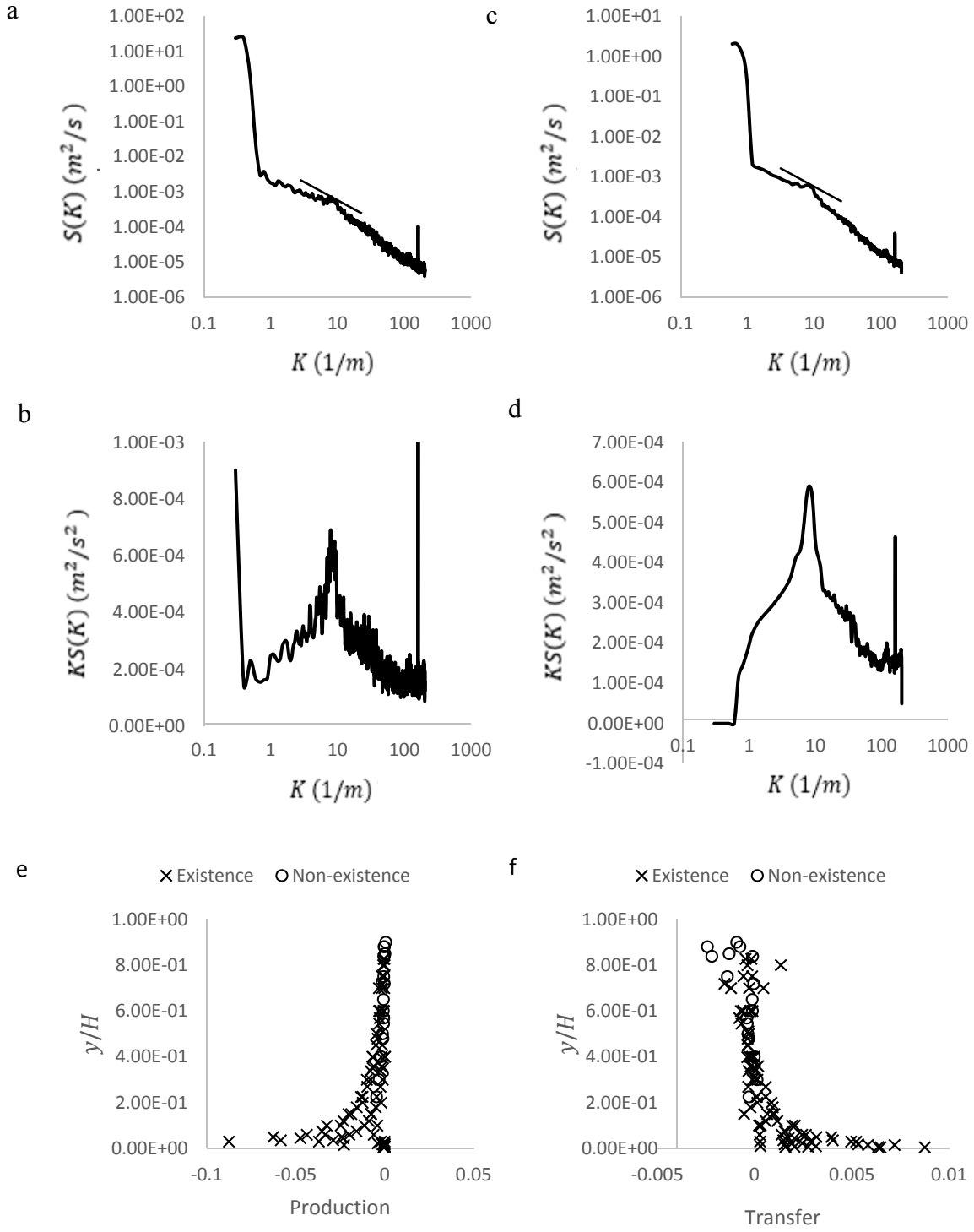


Figure 3.11. Scaling K_m and K_b with inner and outer variables. (a) Scaling K_m with H , (b) Scaling K_m with y , (c) Scaling K_b with H and (d) Scaling K_b with y

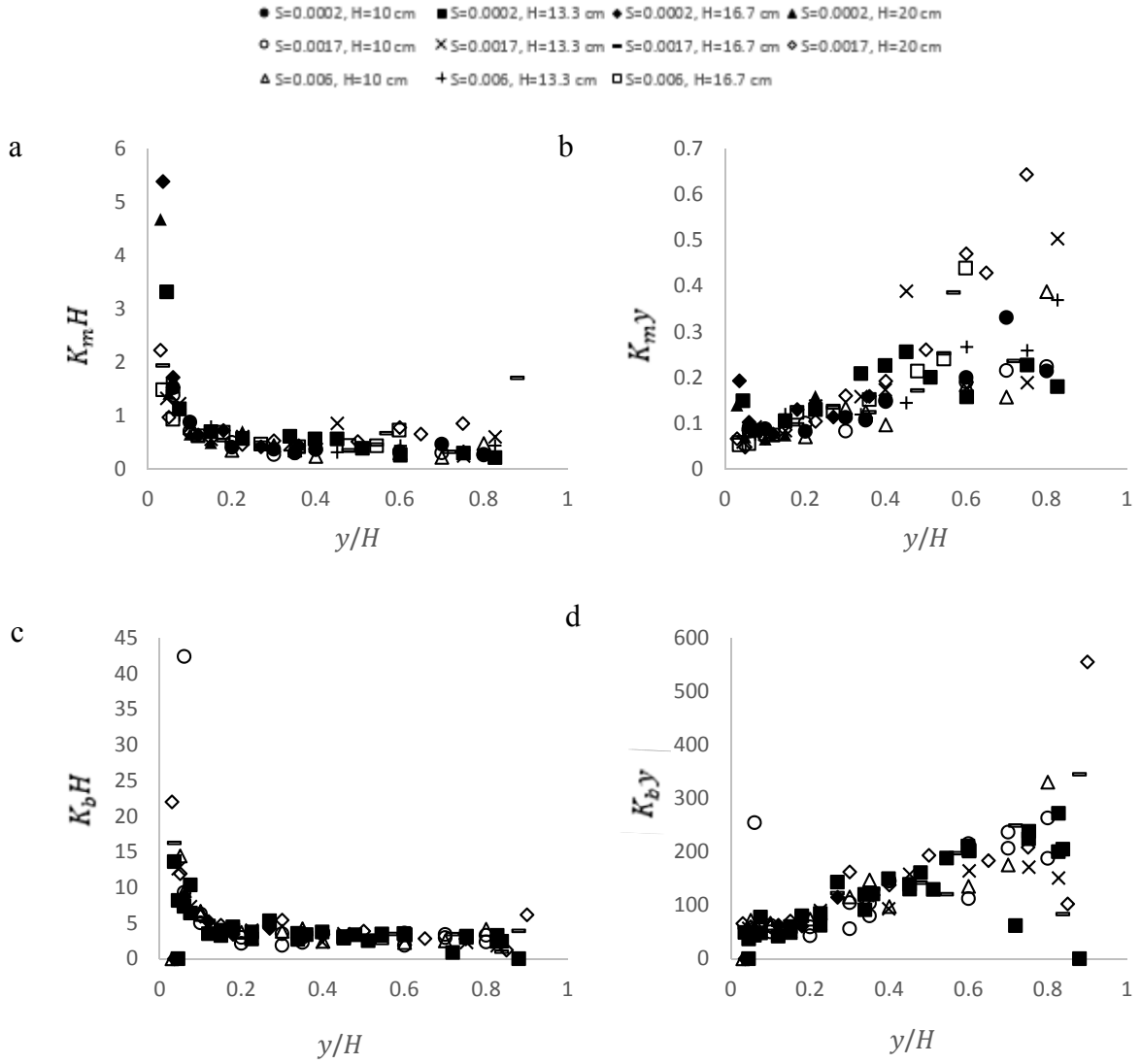


Figure 3.12. Scaling energy spectral with inner and outer variables. (a) non-scaling, (b) Scaling with Nikora method, (c) Scaling with Kim and Adrian method (d) Scaling with $RMSu^2$ and (e) Scaling with our method

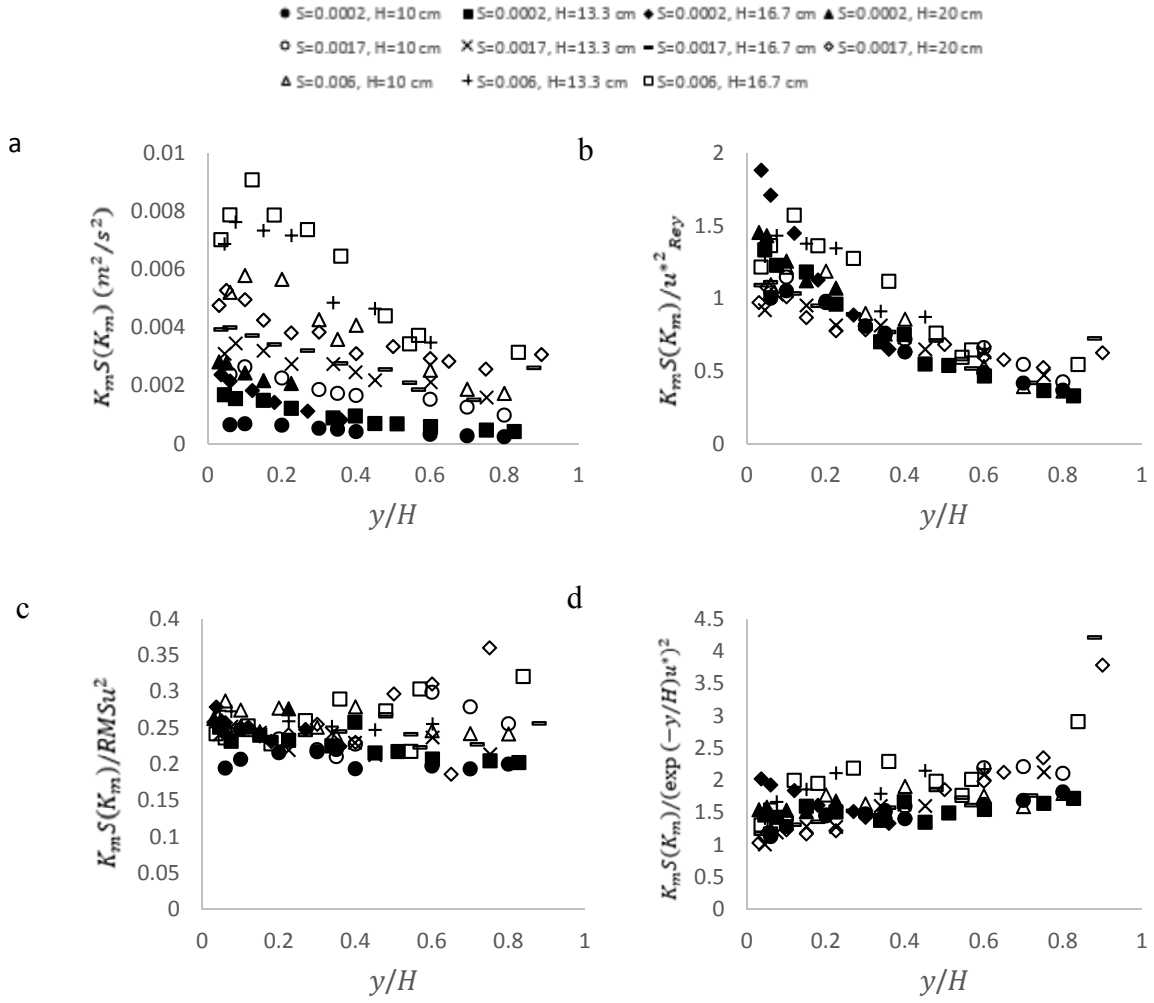


Figure 3.13. Scaling spectral energy and wave-numbers with inner and outer variables for $y/H \leq 0.1$. (a) non-scaling, (b) Scaling with Nikora method, (c) Scaling with Kim and Adrian method (d) Scaling with our method

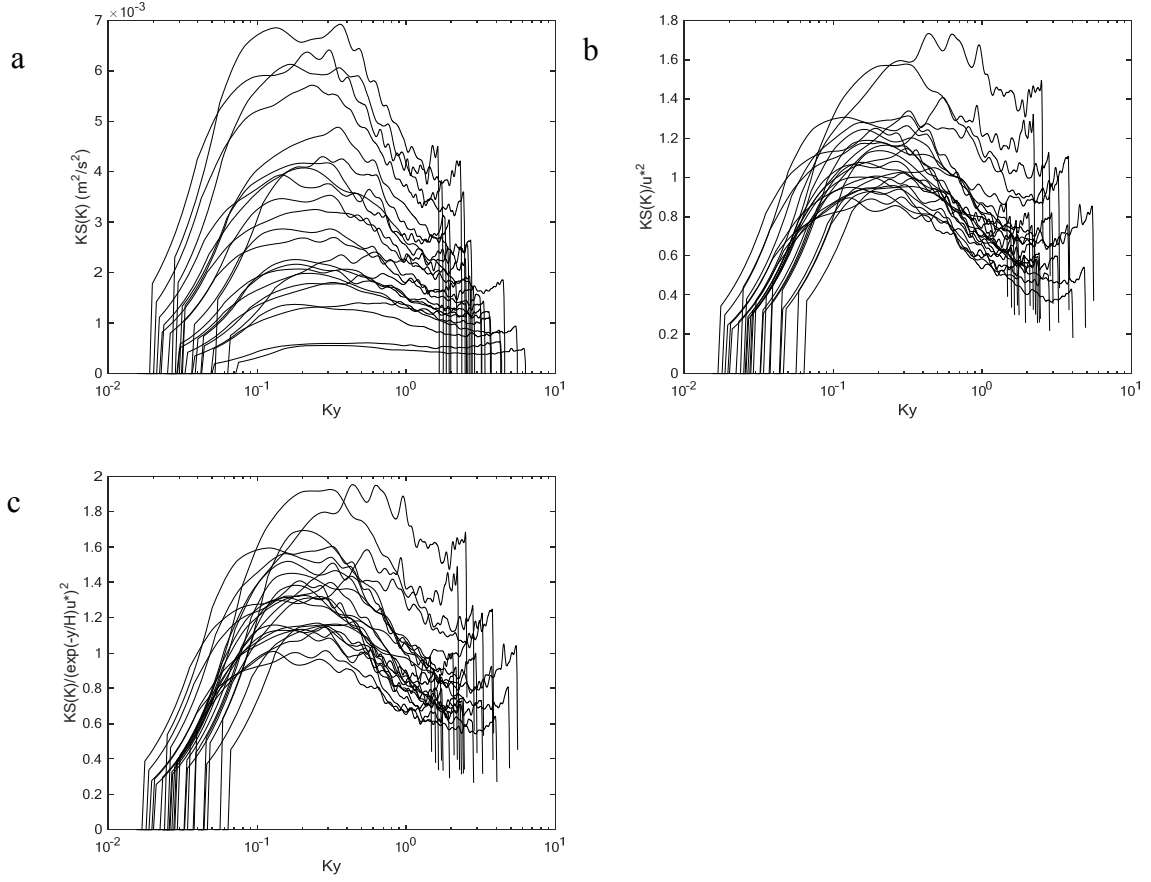
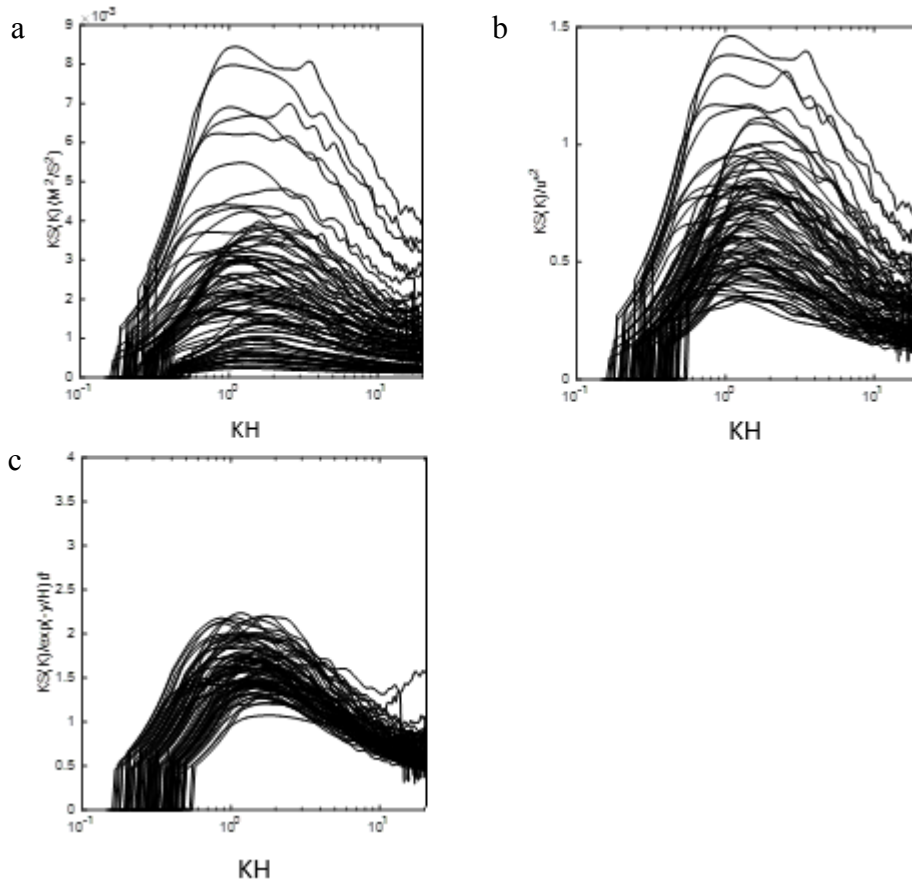


Figure 3.14. Scaling spectral energy and wave-numbers with inner and outer variables for $y/H > 0.1$. (a) non-scaling, (b) Scaling with Kim and Adrian method (c) Scaling with our method



Chapter 4 Methods for Large Flume:

4.1 Experimental Design:

Experiments were designed in the big flume with large roughness with the intent to capture the variation of -1 slope region in a more hydraulically rough open channel flow. Our goal to collect the data in the big flume was to compare the variation of -1 slope and hydraulic parameters which are shown in the table 4.1 to better understand the possible reasons that could lead to different conditions in rivers. In the big flume, the authors designed and carried out four tests shown in Table 4.1 to investigate the turbulence production differences in a flume with different roughness from the small flume. The four tests include one slope and three different flow depths. Two tests are carried out at the same flow condition, the same slope and the same flow depth, but in the different location along the flume (test 1 and 4). Test 4 was placed 3 cm downstream of test 1. Authors could not collect data for the flow depth of 0.2 m due to the limitation of the pump.

All four tests were designed to have the uniform and fully-developed flow like the tests in the small flume. As the same in the small flume, we could vary bed slope (S), gravel particle roughness height (ks), and volumetric discharge externally while the fluid density (ρ) and viscosity (μ), flume width (B) and gravitational acceleration were fixed. The roughness height was kept constant in all four tests but it has a different value from the tests in the small flume. Like the small flume, the relative submergence was always greater than five and the aspect ratio was less or equal to six that lead to the same functional dependence of spectral variable to the dependent variables as

$$k_M, k_B, [kS]_{-1} = fn\{u_*, y, H, v\} . \quad (51)$$

As it is stated initially in this section, our main goal to collect these four tests in the big flume was to compare the results of two flumes. We designed the same conditions in the big flume compare to the small flume but with different slope and gravel particle roughness height to include the effect of gravel particle roughness height in the variation of the -1 power region variables. The functional dependence of spectral variables to the independent variables when the results of the two flumes were compared was updated as

$$k_M, k_B, [kS]_{-1} = fn\{u_*, ks\} \quad (52)$$

4.2 Experimental Setup:

As it is mentioned in section 2.2, we used two different flumes with different roughness to simulate conditions in rough open channel flows. The small flume was described in section 2.2 and the big flume is described in this section. The big recirculating flume was 16 m long and 0.61 m width. The flume bed had mobile gravel roughness elements but in the designed tests that carried out no particle movements were seen. Particle size distribution of bed materials were determined by averaging all measured three diameters of particles. The big flume had gravel roughness elements with $D_{84} = 0.0487 \text{ m}$, geometric standard deviation 0.0126 m and $D_{50} = 0.039 \text{ m}$. We used a 7.5 HP pump to deliver water from the tank to the flume through 6 inches Pipes. Like the small flume, discharge was controlled by the gate-valve that placed on the supply line which connected the pump to the head-box. Channel discharged to a tank with capacity of about 10 m^3 . Water elevation in the tank was measured during the tests to guarantee the same

flow conditions during data collection. In order to provide the fully developed conditions, data collection were placed at approximately 10 m downstream of the inlet. Also testing section was away from the outfall to eliminate the effect of outfall on the fully developed and quasi-uniform conditions. Prior to bed slope measurement and data collection, bed materials were padded to remove any significant ridge or troughs in the bed roughness elements. Then the flume slope was determined by placing the survey rod on a flat plate over the bed elements. Measurements were taken at every 0.4 m and a linear fitting line is used to calculate the flume slope from the measured points. Flume slope were adjusted to the desired slope by adding or removing material. At each section that the materials were added or removed, padding was required to provide the uniform condition all over that section. After adjusting the flume slope, roughness height was determined by averaging 100 measurements of particle distance to the top surface of particles.

4.3 Velocity Data Collection and Post-Processing:

We used the same methodology as described in section 2.3 to collect and post-process the data in the big flume.

4.4 Analyses of Time-Average Parameters: Velocities, Reynolds Stresses and Energy

Terms:

We used the same methodology as described in section 2.4 to analyze the time-average parameters in the big flume.

4.5 Spectral Analyses:

We used the same methodology as described in section 2.5 to perform the spectral analysis.

CHAPTER 4 TABLES AND FIGURES

Table 4.1. Experimental tests conditions for the big flume

Run	S	k_s (m)	Q ($\frac{m^3}{s}$)	ρ ($\frac{kg}{m^3}$)	B (m)	g ($\frac{m^2}{s}$)	u^* ($\frac{m}{s}$)	H (m)	y (m)	B/H	H/k_s	Re ($\times 10^4$)	K^+	Fr	μ ($\times 10^{-3}$)
1	0.0003	0.0161	0.021	998.23	0.61	9.81	0.0122	0.1	0.001-0.08	6.10	8.93	2.6	67.78	0.35	1.002
2	0.0003	0.0161	0.046	998.23	0.61	9.81	0.0135	0.133	0.001-0.11	4.59	11.87	5.3	75.20	0.50	1.002
3	0.0003	0.0161	0.068	998.23	0.61	9.81	0.0146	0.167	0.001-0.147	3.65	14.91	7.2	81.17	0.52	1.002
4	0.0003	0.0161	0.085	998.23	0.61	9.81	0.0154	0.2	0.001-0.13	3.05	17.86	8.4	85.92	0.50	1.002

Figure 4.1. Experimental setup for the big flume



Chapter 5 Results for Large Flume:

5.1 Validating Turbulence Data, Time-Average Parameters and Secondary Currents:

We performed the same procedure as the small flume (section 3.1) to the big flume to validate the data collected for this flume.

We used the same methods as described for the small flume to calculate the friction velocity for the big flume. Friction velocity values and plots are shown in Table 5.1 and figure 5.1. Unlike the small flume, friction velocity estimated by using the log layer of velocity profile are smaller than the friction velocity estimated by the Reynolds number for the big flume. One possible reason for this difference between two flumes could be due to κ , von Karman constant. We used the same κ value for both flumes but it could be possible for the big flume to have a smaller value for κ . Again we preferred to use the friction velocity estimated by the primary Reynolds stress data for our analysis and scaling because not only the primary Reynolds number is a turbulence quantity but also this method of estimation is not dependent on any constants.

In the next step after calculating the friction velocity for the big flume, we scaled the time-average turbulence parameters to the laws developed for the same condition as ours. First we scaled the streamwise velocity with inner and outer and mixed variables to investigate the dominant parameters that affect the velocity profile as shown in figure 5.3. As it is shown in figure 5.3b, velocity profiles can be scaled nicely with friction velocity and U_{max} which is an outer variable is dependent on friction velocity. The close dependency of U_{max} on friction velocity causes the scaling with U_{max} to reduce the variance in the distribution of velocity data as well as the scaling with friction velocity.

Then we scaled the primary Reynolds stress and streamwise Reynolds normal stress with inner and outer variables as shown in figure 5.4. In figure 5.4a, we compared the scaled primary Reynolds stress with the law as shown in equation 36. As it is shown in figure 5.4a, primary Reynolds stress attained its maximum value at approximately $y/H = 0.2$.

Figure 5.4b-f shows the streamwise Reynolds normal stress with inner and outer variables. First, like the small flume, we scaled the streamwise Reynolds normal stress with three friction velocity estimated by different ways and compared the results to the law shown in equation 37. As shown in figure 5.4 and compare this figure to figure 3.4, the empirical coefficient which is found by fitting line is approximately equal for the streamwise Reynolds normal stress scaled by the friction velocity estimated by the primary Reynolds stress data. This finding support the method using primary Reynolds stress data as the best way to estimate the friction velocity. Like the average streamwise velocity, scaling the streamwise Reynolds normal stress with U_{max} reduces the variation in distribution of normal stress as well as scaling with the friction velocity. We used equation 38 and 39 to scale the streamwise Reynolds normal stress with outer variables as shown in figure 5.4e and 5.4f. The empirical coefficient for these scaling were 3.72 and 0.24 respectively.

Figure 5.5 shows the secondary velocities for the big flume without scaling. This figure is shown on the purpose of investigating the secondary currents exist in the flow.

Scaled secondary Reynolds normal stresses, TKE and anisotropy are shown in figure 5.6. These plots show the strong dependency of average turbulent parameters on the inner variable, friction velocity estimated by the primary Reynolds stress here.

5.2 Selecting Wavenumbers for Macroturbulence and Bursting:

We used the same method as described in section 3.2 to find the wavenumbers got macroturbulence and busting structures.

5.3 Scaling of the Wavenumbers and Energy for Macroturbulence, Bursting and the -1 Power Region Plots:

We used the same inner and outer variables used in the small flume to scale the wavenumbers of macroturbulence and bursting in the big flume. The results of these scaling are shown in figure 5.7. Like the small flume, wavelengths of macroturbulence and busting are better scaled with y for the inner regions and for outer regions it is better to use H as the scaling parameter. One difference between the results of these two flumes was related to the depth of inner region that can be scaled with y . For the small flume, it was better to scale the wavelengths with y for $y/H \leq 0.1$ and scale with H for $y/H > 0.1$ while for the big flume it was better to scale the wavelengths with y for $y/H \leq 0.4$ and scale with H for $y/H > 0.4$. This difference is related to the different roughness height that affect the shedding processes and eddy formation. Also, when the macroturbulence and bursting get their constant lengths for both flumes ($y/H > 0.1$ for the small flume and $y/H > 0.4$ for the big flume), the wavenumbers for both the macroturbulence and bursting are twice big for the big flume compare to the small flume. This means the length scales of macroturbulence and bursting structures in the small flume are twice larger than in the big flume. Again this difference can be related to the different roughness height that cause the generation of eddies from the bed with different angles.

Like the small flume, in figure 5.8. we showed spectral energy of macroturbulence and bursting structures scaled with different methods. As it is shown in figure 5.8, $RMSu^2, u^{*2}_{Rey}$ and our new method are the best parameters to scale the energy of macroturbulence and bursting structures. Like the small flume, in order to better visualize the scaling effect on the wavenumbers and energy of macroturbulence and bursting structures, we showed the variance preserving spectral for different scaling parameters for all three tests in figure 5.9 and 5.10. Based on figure 5.7, we chose $y/H=0.4$ as the threshold for scaling the wavenumbers with inner variable, y , or outer variable, H . Figure 5.9 shows inner scaling for wavenumbers and three different scaling for spectral energy. Like the small flume, both our method and Kim and Adrian method (figure 5.9b and c) are the best methods to scale the inner region. For outer region (figure 5.10), our scaling works best although it is not good as for the small flume. The reason could be related to the white noise in the spectral plots.

CHAPTER 5 TABLES AND FIGURES

Table 5.1. Results of the friction velocity estimated from different methods for the big flume.

Test	S	$H (m)$	$u^* = \sqrt{gRS} (\frac{m}{s})$	u^* using log-law ($\frac{m}{s}$)	u^* using Reynolds Stress ($\frac{m}{s}$)
1	0.0003	0.1	0.01488	0.0227	0.0316
2	0.0003	0.133	0.01651	0.028	0.0387
3	0.0003	0.167	0.01782	0.039	0.0547
4	0.0003	0.1	0.01488	0.0235	0.02

Figure 5.1. Comparison of the friction velocity from the three methods. (a) Comparison of second and third method. (b) Comparison of first and second method. (c) Comparison of first and third method

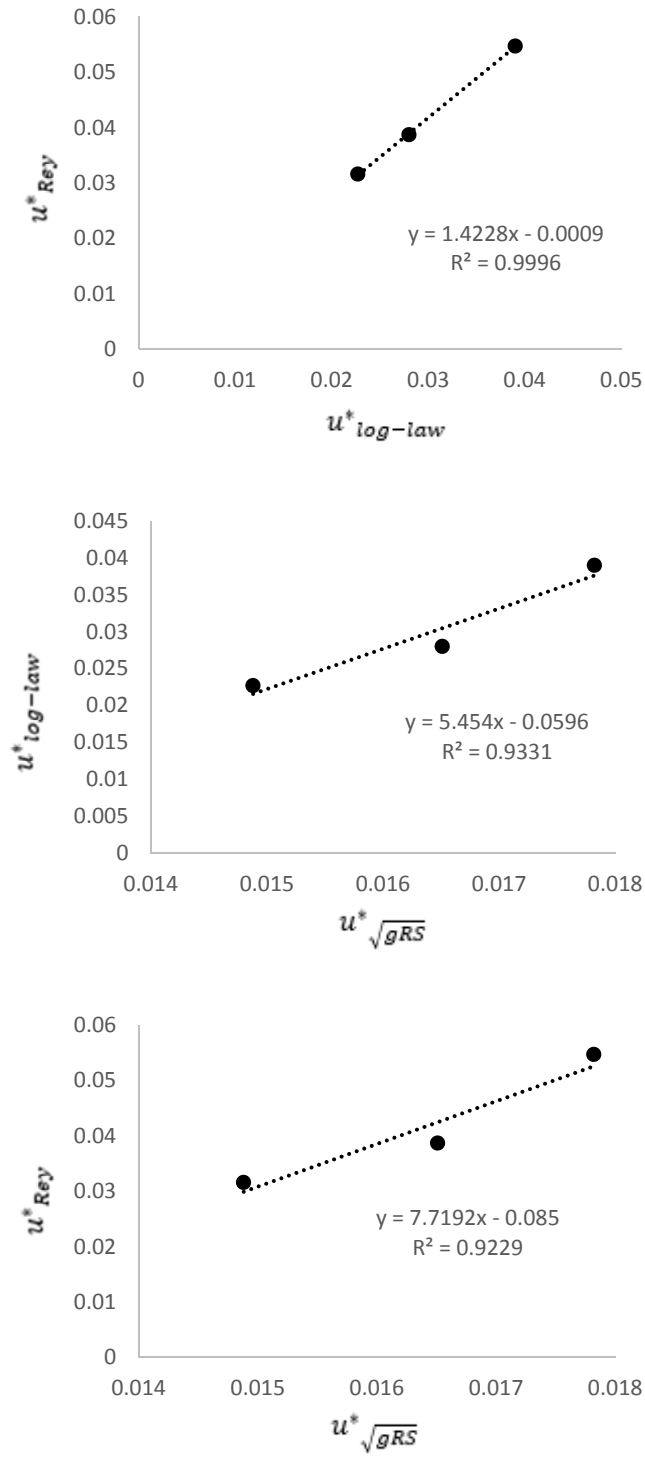


Figure 5.2. Example of parameter fitting to estimate the friction velocity. (a) shows the linear region identified for fitting the friction velocity via the logarithmic law. (b) shows an example of log law fitting. (c) shows fitting of the friction velocity using the primary Reynolds stress.

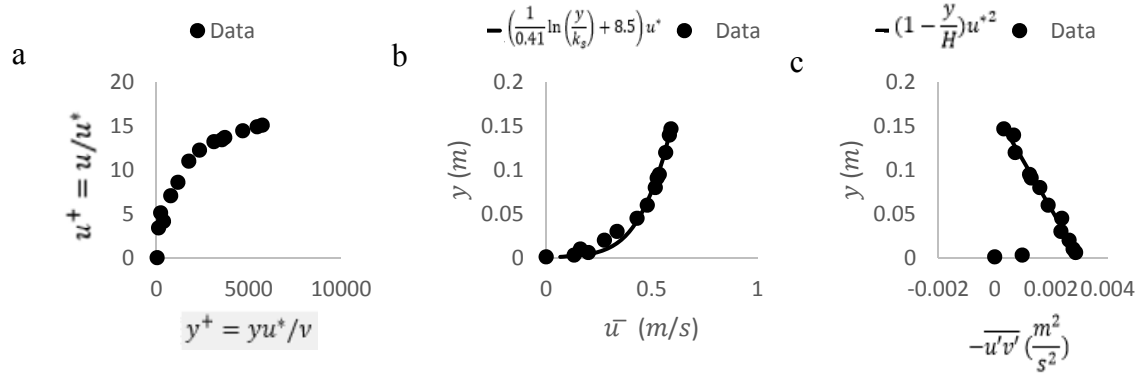


Figure 5.3. Streamwise velocity distributions for the datasets including: (a) no scaling (b) inner scaling and the law of the wall, (c) outer scaling with the freestream velocity and (d) outer scaling with the friction velocity.

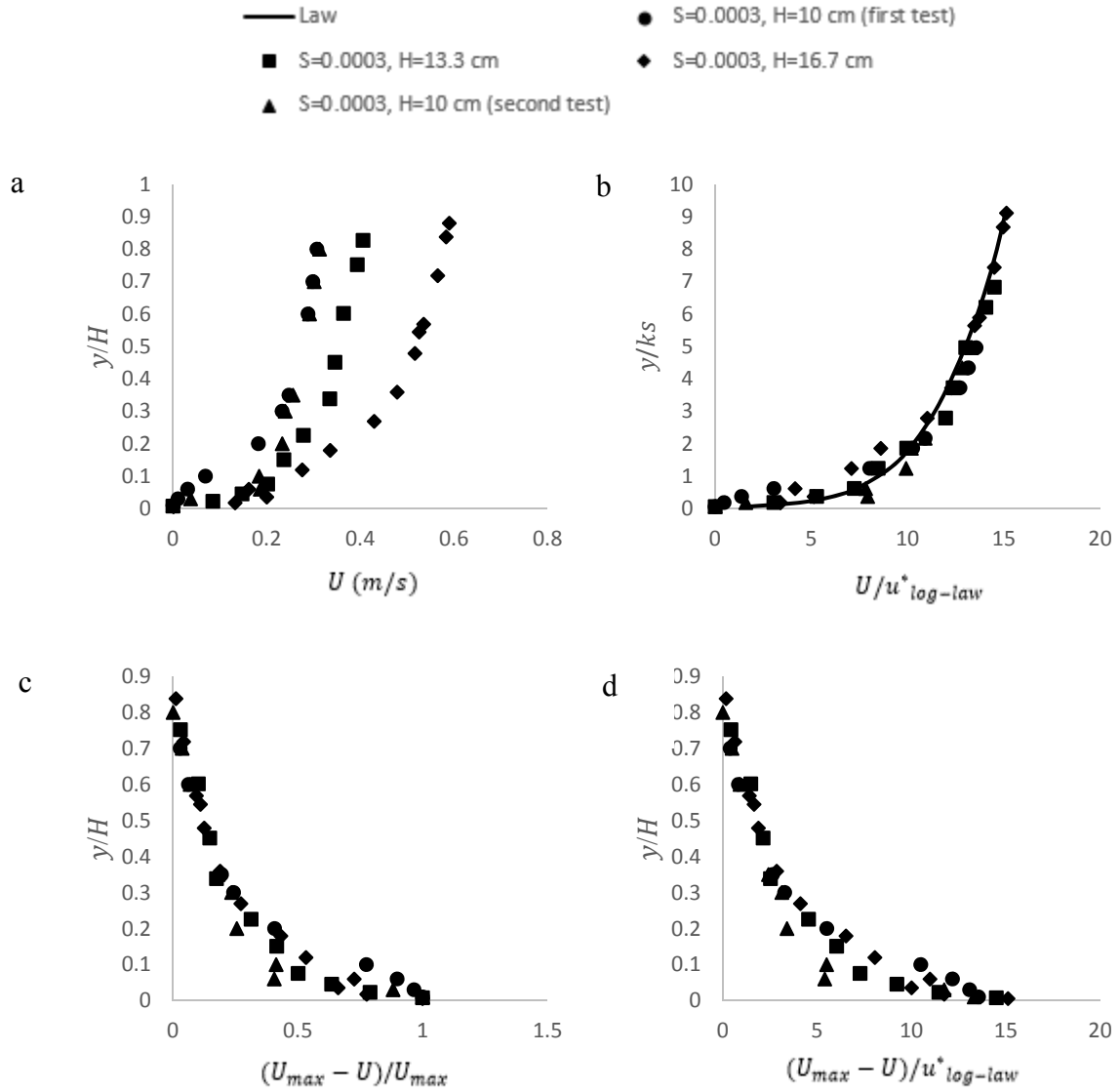


Figure 5.4. (a) Primary Reynolds shear stress and (b-f) streamwise Reynolds normal stress scaled with (b) the friction velocity estimated from the logarithmic law method, (c) the friction velocity estimated from the Reynolds shear stress data, (d) the friction equal to \sqrt{gRS} , (e) average streamwise velocity, (f) maximum streamwise velocity

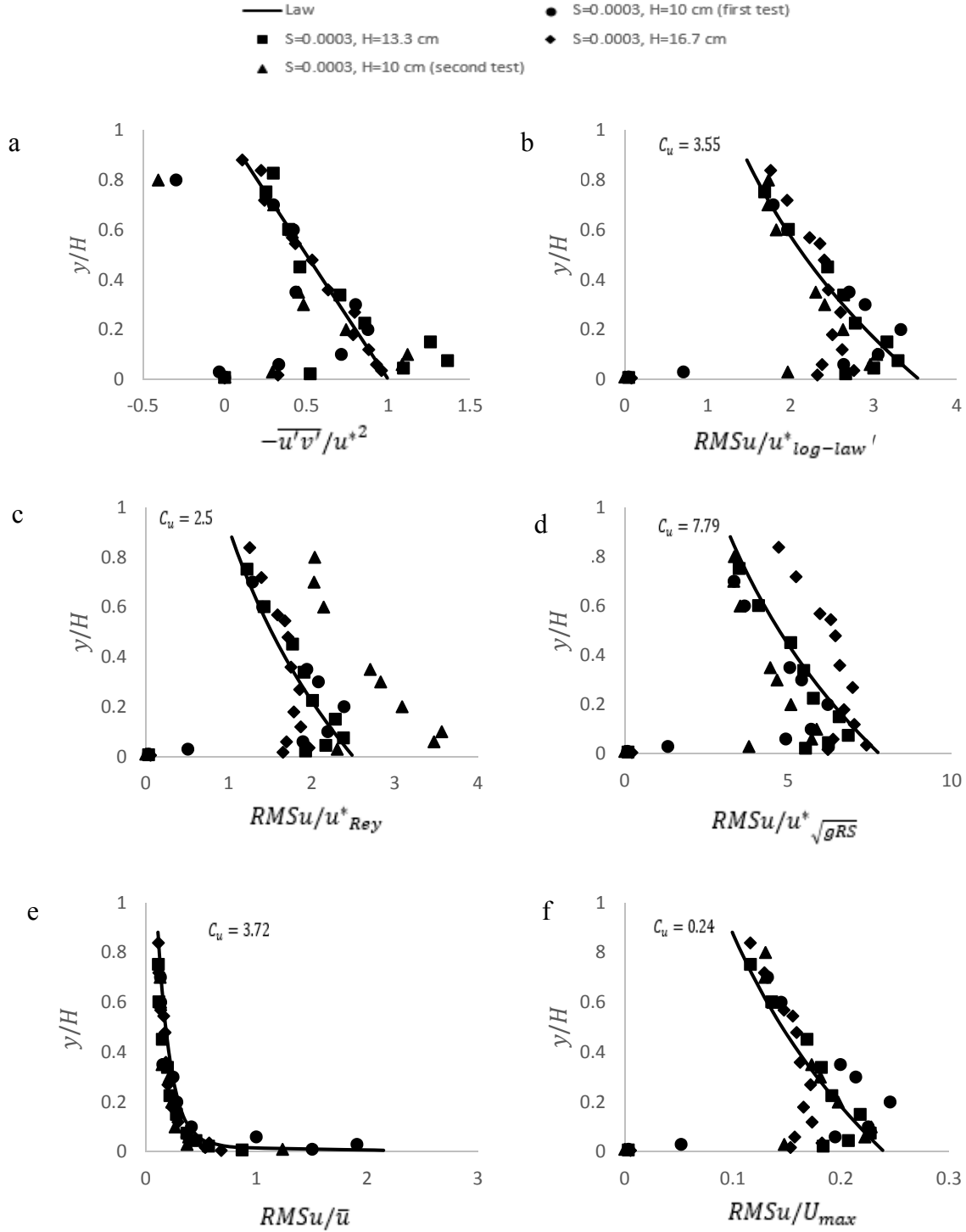


Figure 5.5. Secondary velocities. (a) vertical velocity, (b) lateral velocity

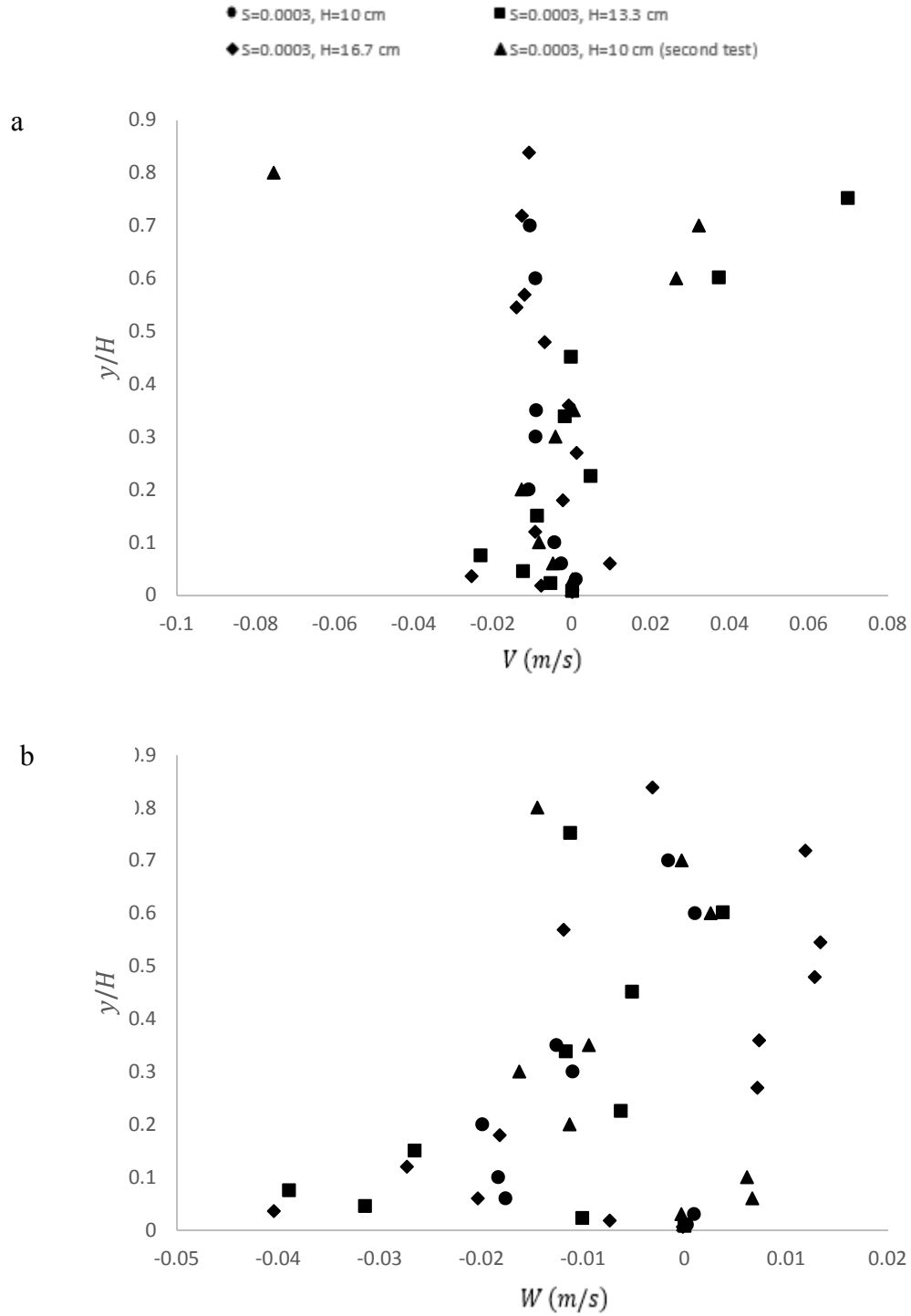


Figure 5.6. (a, b) Secondary Reynolds normal stresses (v, w) scaled with the friction velocity estimated via the primary Reynolds stress method and the exponential law plotted for the secondary terms; (c) turbulent kinetic energy normalized with friction velocity squared, and (d) anisotropy normalized with friction velocity squared.

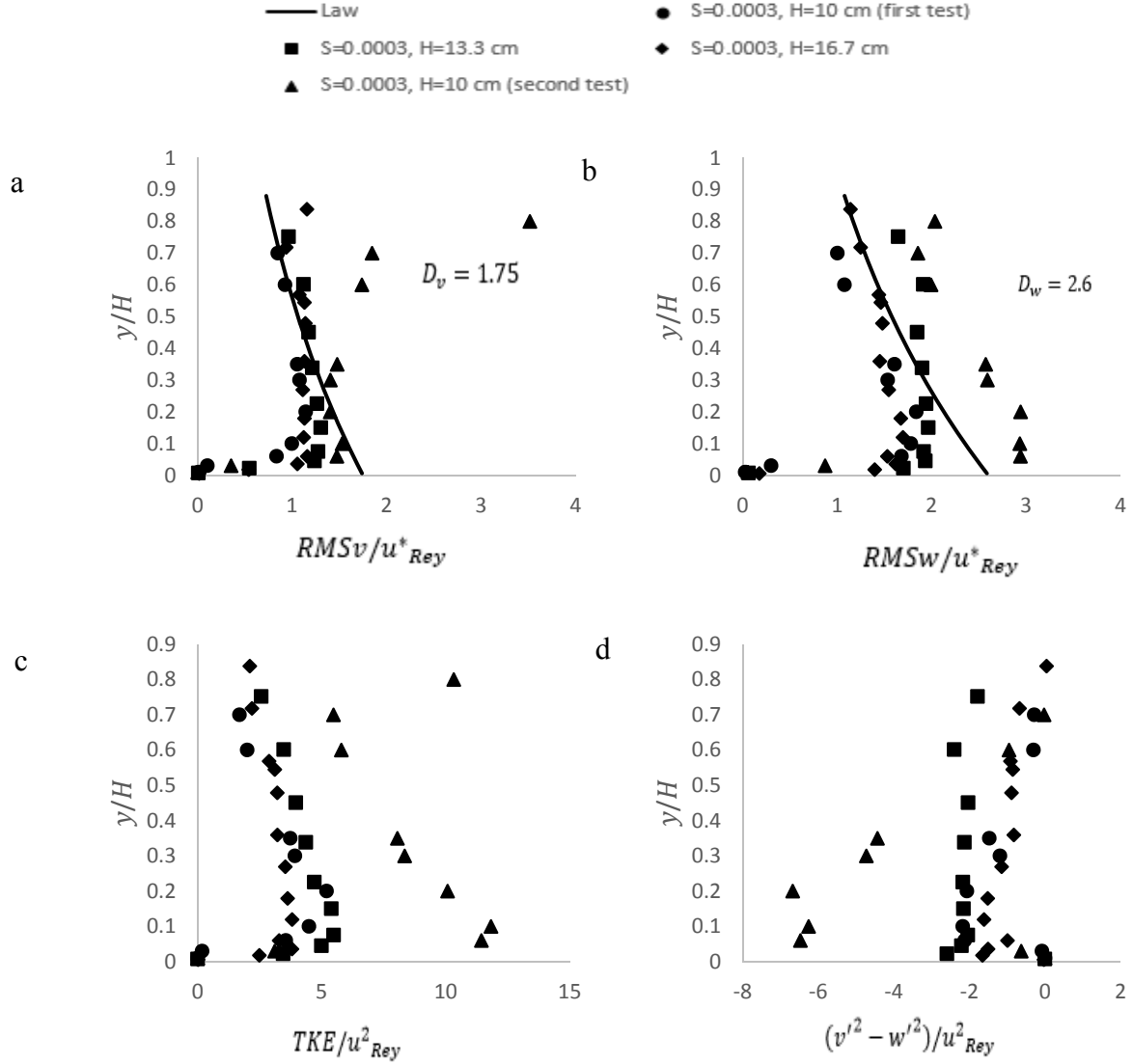


Figure 5.7. Scaling K_m and K_b with inner and outer variables. (a) Scaling K_m with H , (b) Scaling K_m with y , (c) Scaling K_b with H and (d) Scaling K_b with y

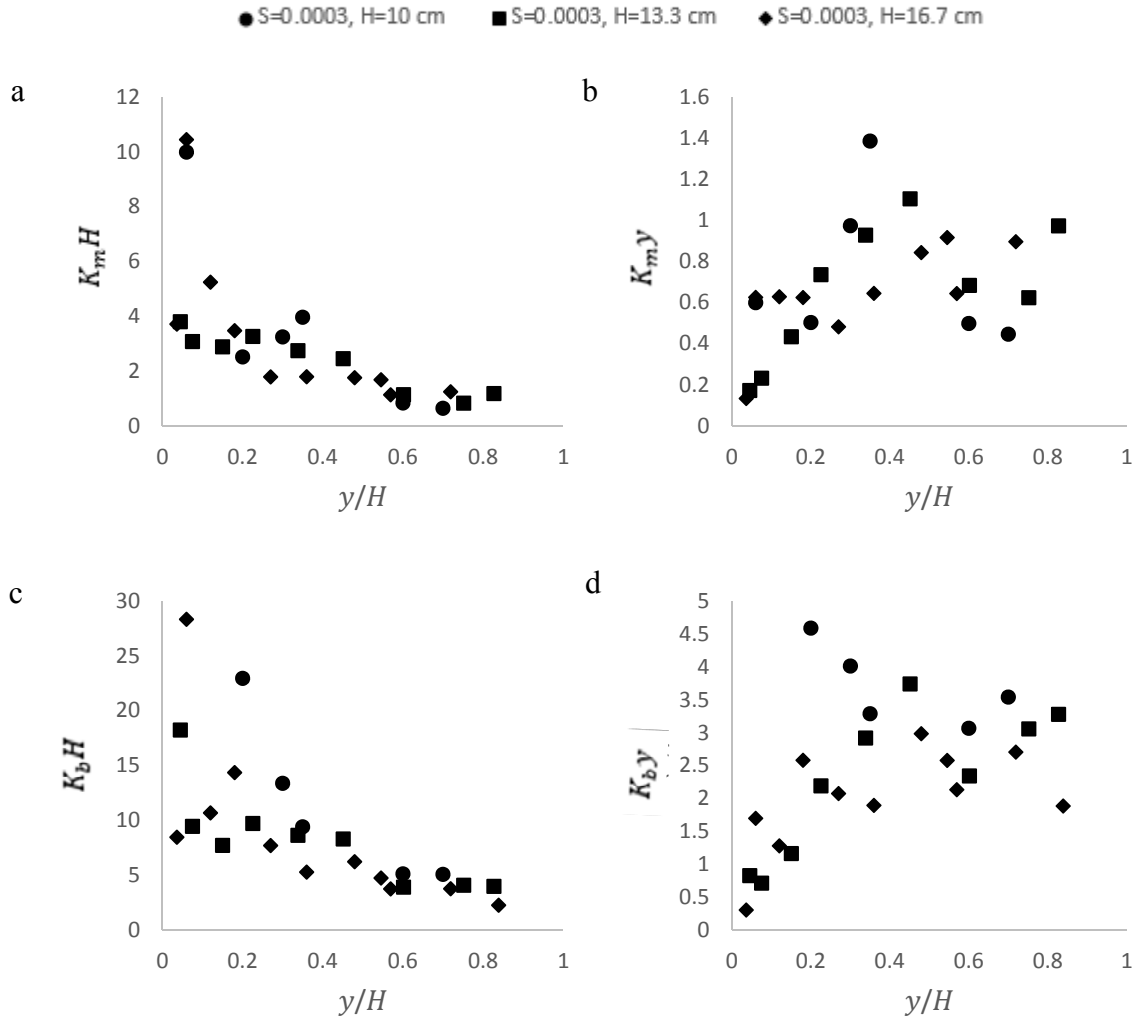


Figure 5.8. Scaling energy spectral with inner and outer variables. (a) non-scaling, (b) Scaling with Kim and Adrian method (c) Scaling with $RMSu^2$ and (d) Scaling with our method

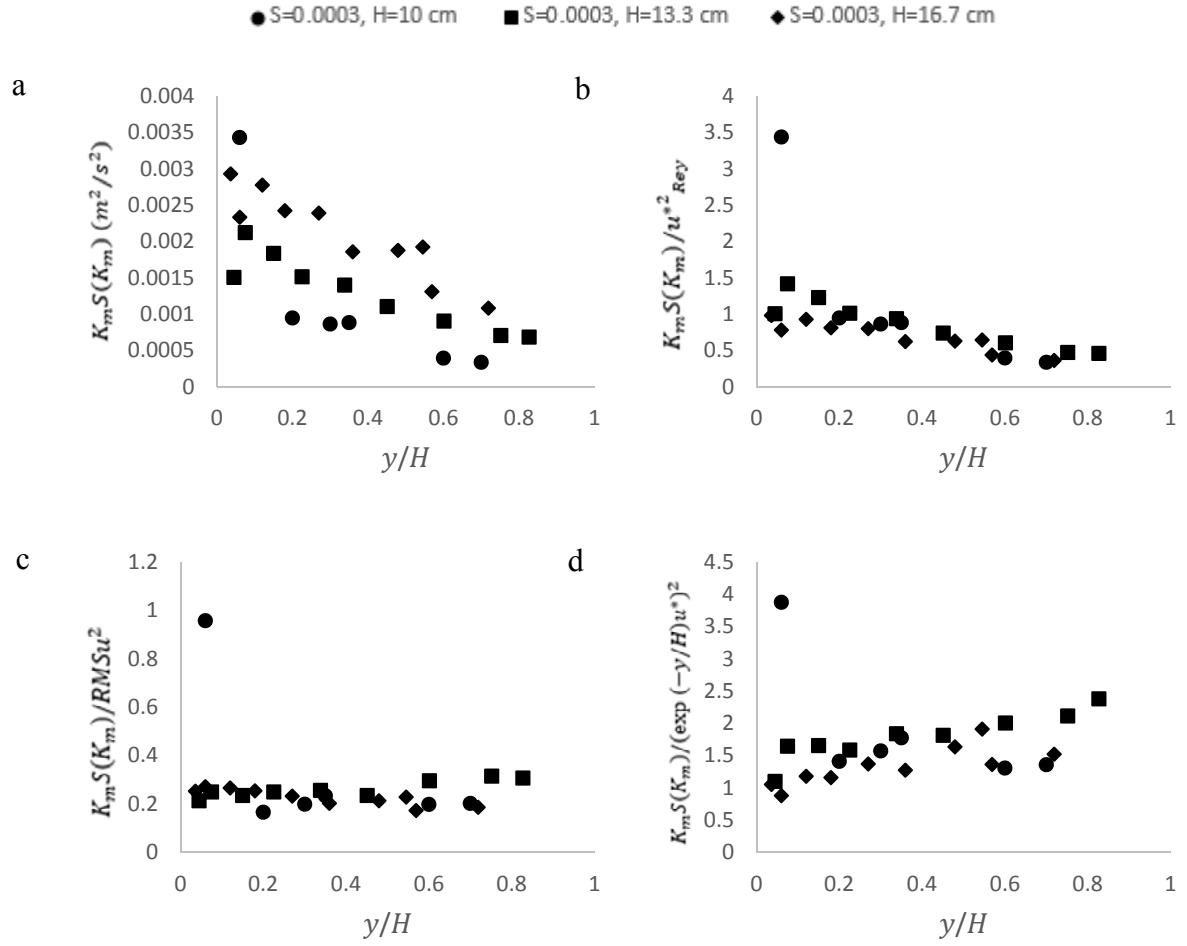


Figure 5.9. Scaling spectral energy and wave-numbers with inner and outer variables for $y/H \leq 0.4$. (a) non-scaling, (b) Scaling with Kim and Adrian method (c) Scaling with our method

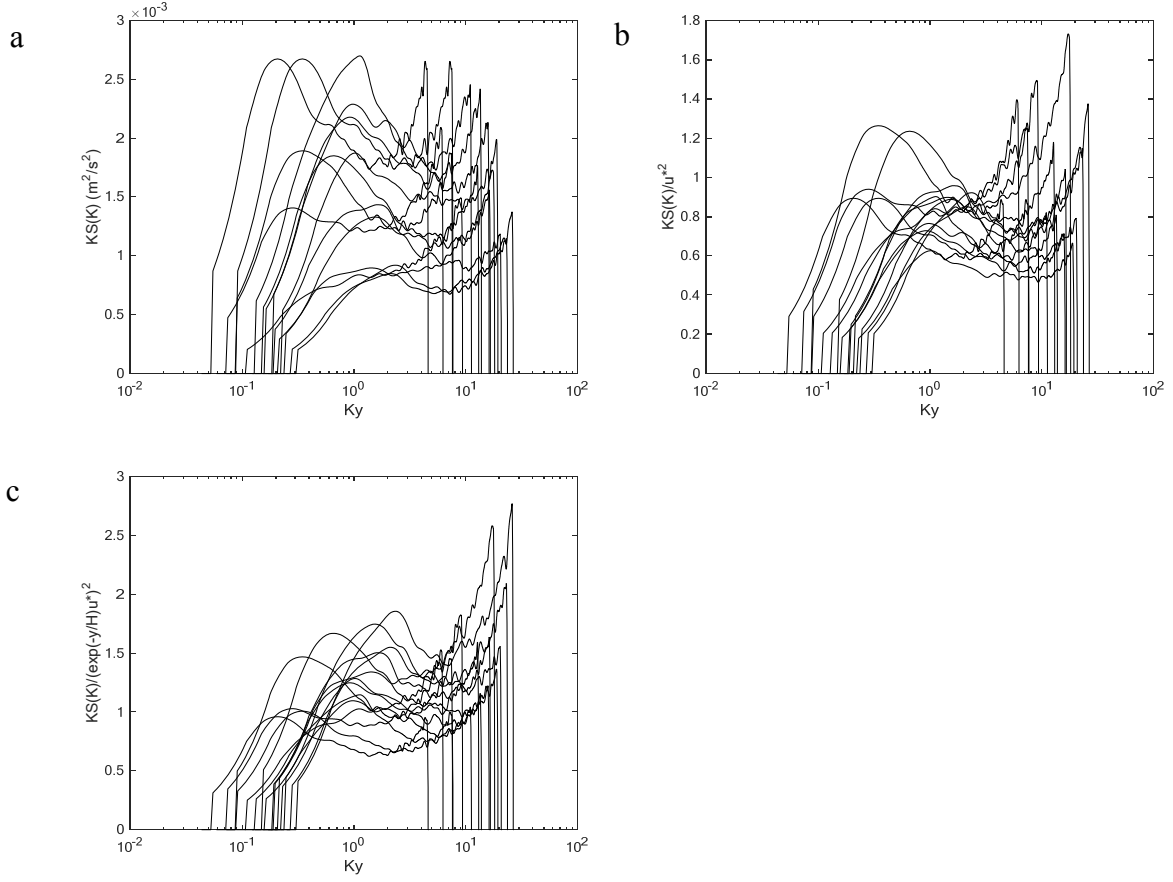
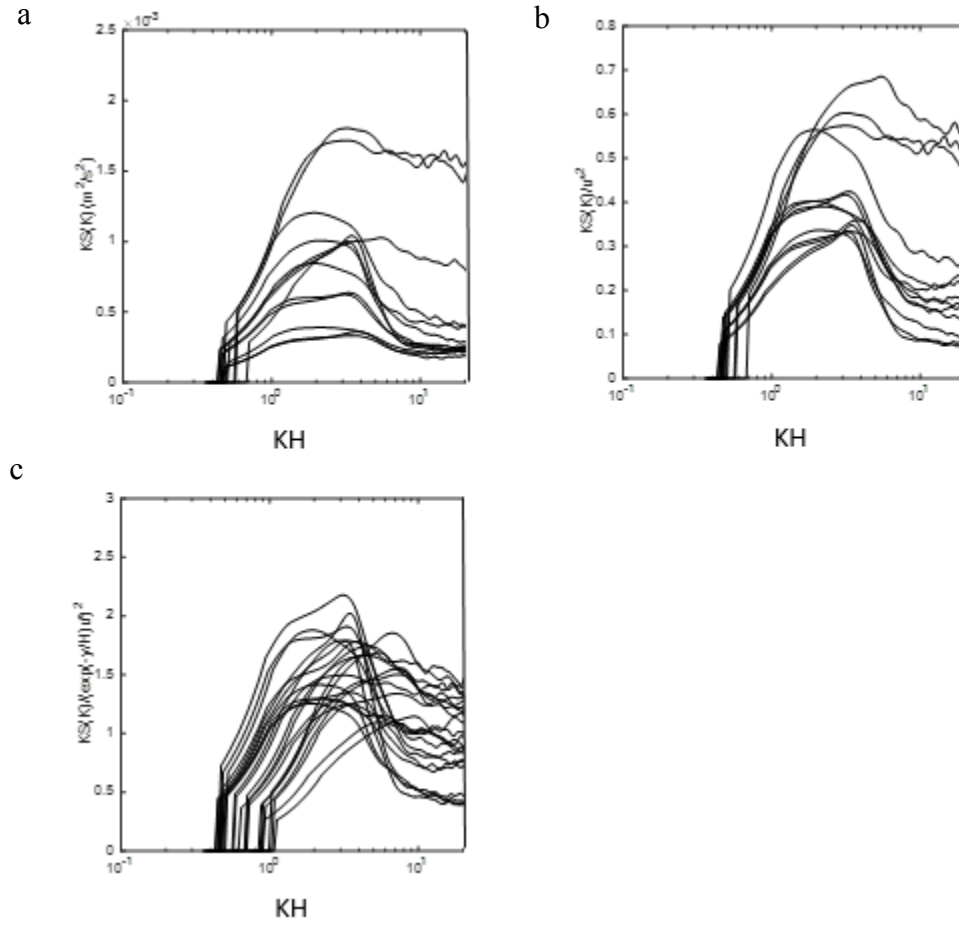


Figure 5.10. Scaling spectral energy and wave-numbers with inner and outer variables for $y/H > 0.4$. (a) non-scaling, (b) Scaling with Kim and Adrian method (c) Scaling with our method



Chapter 6 Comparison the results of two flumes:

In this section, we compare the results of two flume for time-average turbulence and spectral parameters. In figure 6.1 scaled streamwise velocity for both flumes are compared. As shown in figure 6.1a both flumes follow the developed equation for rough open channel flows (equation 34) which validates the quality of data collected for both flumes. It is worth to notice in figures 6.1 that both flumes agree to the equilibrium boundary layer for the outer region ($y/H > 0.5$) when scaled with inner or outer variables.

In figure 6.2, we compared the scaled primary Reynolds stress and streamwise Reynolds normal stress for both flumes. As shown in this figure, friction velocity estimated by the primary Reynolds stress data is the best parameter to scale the primary Reynolds stress and streamwise Reynolds normal stress. We may also conclude from this figure that von Karman constant could be smaller than 0.41 for the big flume.

Figure 6.3 shows comparison of other parameters for two flumes. As shown in this figure, secondary Reynolds normal stresses and consequently turbulent kinetic energy values are bigger for the large flume. This can be due to the stronger secondary currents in the large flume or may the secondary velocities are contaminant with noise in the large flume. Anisotropy is also bigger for the large flume which may support the hypothesis of stronger secondary currents exist in flumes with bigger roughness.

We noticed in figures 3.12, 3.13, and 3.14 that there is a strong relation between the spectral energy and streamwise Reynolds normal stress. We plotted the average level of energy in the ‘-1’ power law region vs. $RMSu^2$ in figure 6.4 to show this relation. Average energy is the average energy of macroturbulence and bursting structures. In figure

6.4b, we scaled both the vertical and horizontal axis with U^2 to make them dimensionless. In this figure, we can notice that the average level of energy in the '-1' power law region has always the same relation to the $RMSu^2$ ($energy = 0.25 RMSu^2$). This relation is not dependent on the bed roughness and is held for all conditions with different roughness.

Figure 6.5 demonstrates as the flow depth increase the size of large eddies increases. This figure shows the effect of bed roughness on the angle of bursting. For example, in the large flume, eddies are forced to burst in a steeper angle than the small flume. The angle of shedding is steeper near the bed due to the effect of bed roughness and decrease as eddies move toward the surface. In this regard, the effect of flow depth on the size of large scale eddies is more significant in channels with bigger roughness. In other words, if flow depth is doubled and flow depth is not much higher than the roughness height to diminish the effect of roughness, large scale eddies grow more in channels with bigger roughness compare to the channels with small roughness. This phenomenon is shown in figure 6.5 where the straight line for the big flume is steeper than the straight line for the small flume.

CHAPTER 6 TABLES AND FIGURES

Figure 6.1. Comparison of streamwise velocity distribution for two flumes: (a) inner scaling and the law of the wall, (c) outer scaling with the freestream velocity and (d) outer scaling with the friction velocity.

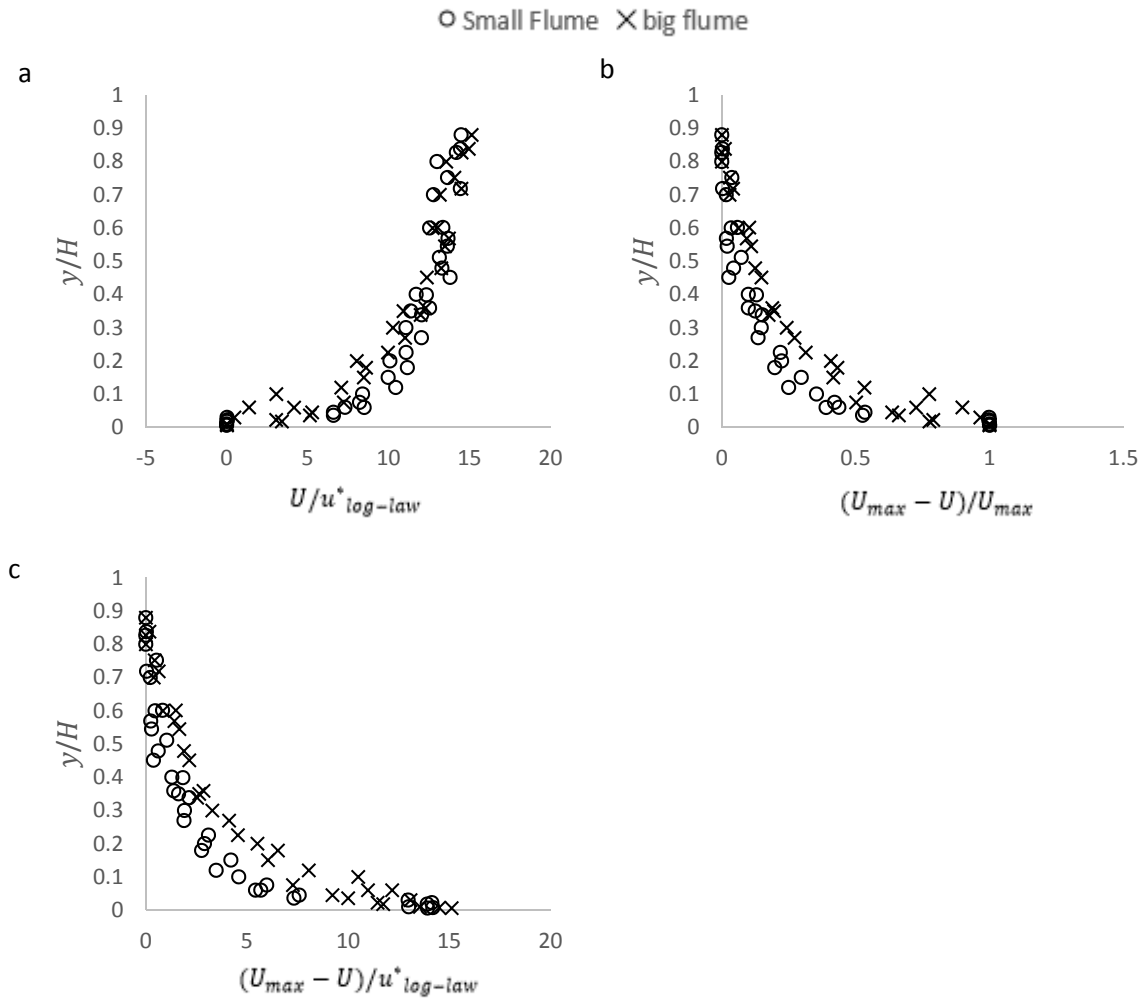


Figure 6.2. Comparison of two flumes (a) Primary Reynolds shear stress and (b-f) streamwise Reynolds normal stress scaled with (b) the friction velocity estimated from the logarithmic law method, (c) the friction velocity estimated from the Reynolds shear stress data, (d) the friction equal to \sqrt{gRS} , (e) maximum streamwise velocity

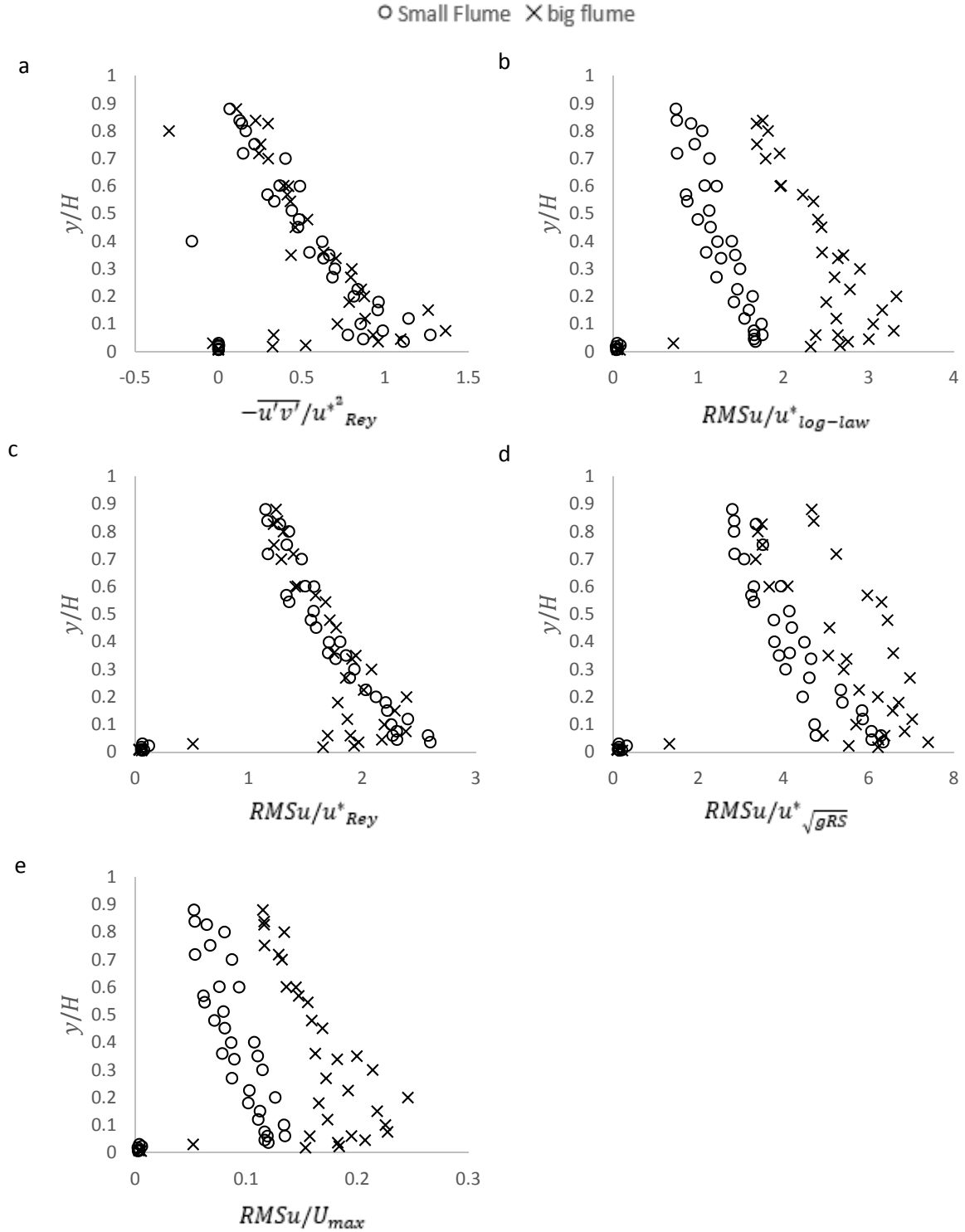


Figure 6.3. Comparison of two flumes. (a, b) Secondary Reynolds normal stresses (v, w) scaled with the friction velocity estimated via the primary Reynolds stress method; (c) turbulent kinetic energy normalized with friction velocity squared, and (d) anisotropy normalized with friction velocity squared; Secondary velocities. (e) vertical velocity, (f) lateral velocity

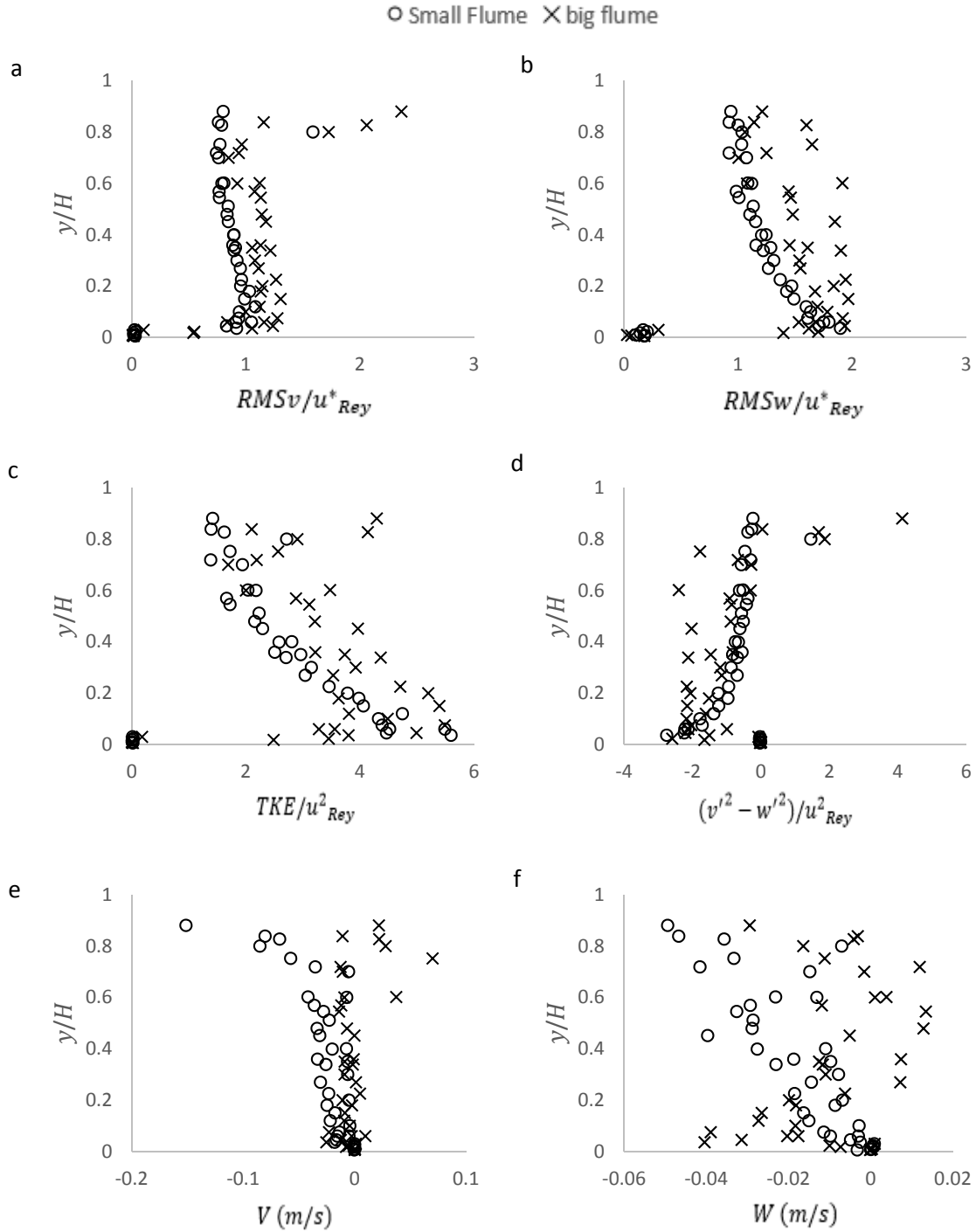


Figure 6.4. Relationship between average energy of macroturbulence and bursting structures in ‘-1’ power region and streamwise Reynolds normal stress. (a) non-scaling for small flume, (b) scaled for small flume, (c) non-scaling for big flume, (d) scaled for big flume

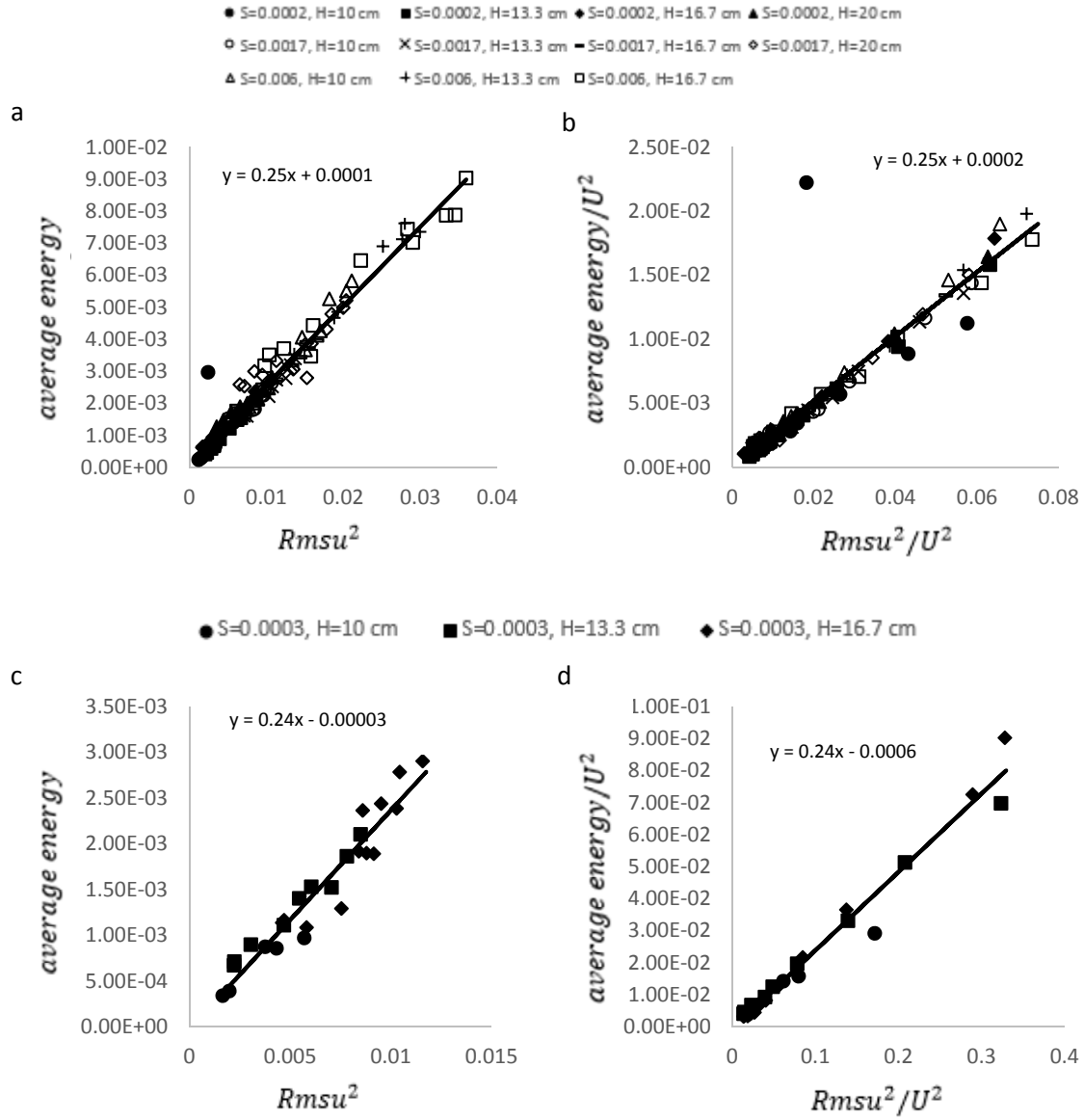
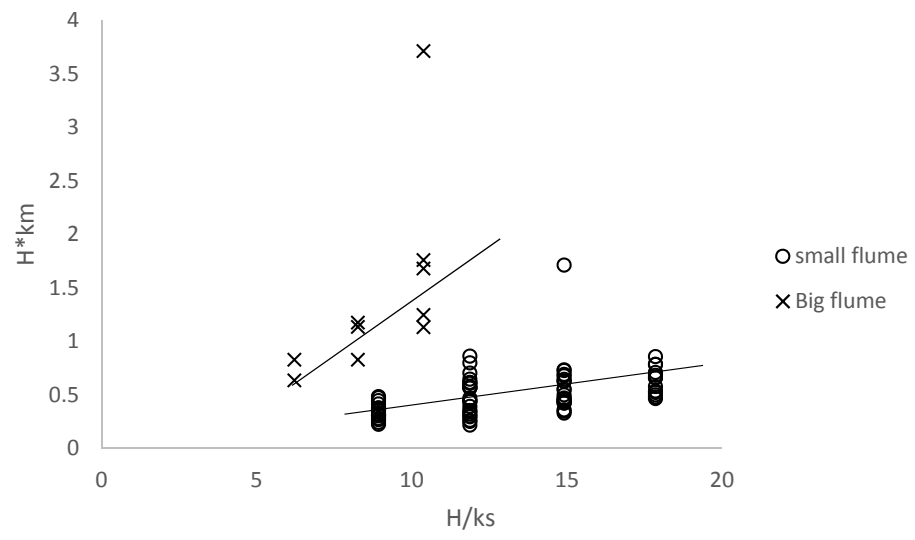


Figure 6.5. Plot of $K_m H$ vs H/K_s for both flumes



Chapter 7 Discussion

As we interpret the results of this research, we point towards the most apparent summarized features of the results that provide context and meaning to the turbulence data including the following (1) The test results for time average parameters are consistent with open channel flow of water over a rough gravel bed scenario that admits to an equilibrium boundary layer for the outer region. (2) Turbulence production also admits to the definition of an equilibrium boundary layer for the outer region due to the new scaling of the -1 power region used in this study. (3) For fixed roughness type the scales of K_m and K_b reach similarity in the outer region, regardless of external energy input or aspect ratio of the open channel flow suggesting that the form of macroturbulence and bursting behave similarly for different hydraulic conditions. (4) The energy production scales associated with K_m and K_b show dependent upon the roughness characteristics, even in the far-wall outer region of the flow. (5) Results of this study provide an approach to calculate the streamwise turbulence kinetic energy of bursting and macroturbulence which show a linkage of this work to applications. (6) The methods used in this study might be considered and built upon in future research. We elaborate on each of these points in the paragraphs of the discussion that follows.

All of the laboratory tests with their experimental conditions and results of this research are consistent with open channel flow of water over a rough gravel bed scenario that admits to an equilibrium boundary layer for the outer region of the flow in which the flow is uniform and fully-developed. That is, the majority of the flow profiles, with the exception of within the roughness layer, $y/H < 0.1$, or sometimes close to the free surface, exhibit features of an equilibrium boundary layer. The turbulence characteristics admit to

Townsend's Reynolds similarity hypothesis (Townsend, 1976) which further reflects the equilibrium boundary layer definition brought by Clauser (1952, 1954) and later revisited with the asymptotic invariance principle by George and Castillo (1997). An equilibrium boundary layer exhibits self-similarity and the boundary layer equation does not depend on the x-coordinate (Clauser, 1952; Townsend, 1976; George and Castillo, 1997). Such an equilibrium boundary layer is balanced in terms of turbulence energy generation and dissipation and show constant velocity and length scales, where the friction velocity is derived as a constant for Clauser's equilibrium definition and the freestream velocity is derived as constant for George and Castillo's equilibrium definition.

The outer region of the flow ($y/H > 0.1$) reflects such approximate equilibrium definitions as both the friction velocity and freestream velocity were shown to scale the velocity defect for both roughness types (see Figures 3.3 and 5.3). Further, the friction velocity is shown to scale the primary Reynolds stresses and the behavior is consistent of that for a uniform open channel flow (see Figures 3.4 and 5.4). Also, the idea is further supported by the fact that the friction velocity scales well the total turbulent kinetic energy as well as streamwise, vertical and transverse components alone (see Figures 3.4, 3.6, 5.4, 5.6). The single energy components also obey reasonably well the laws derived from the production-dissipation model for turbulent kinetic energy in an equilibrium boundary layer (see Figures 3.4, 3.6, 5.4, 5.6). The equilibrium boundary layer concept is shown to be fairly consistent even in light of the weak secondary motion within the present study which is highlighted by observation of the secondary velocities (Figures 3.5, 5.5) and turbulence anisotropy away from the wall (see Figures 3.6 and 5.6).

A new contribution of this research is that the turbulence energy production also admits to the definition of an equilibrium boundary layer for the outer region. The energy associated with turbulence production that is indicated by the -1 power region of the spectra as well as the turbulent energy associated with bursting and macroturbulence best collapse when scaled with the scaling law derived from the turbulence energy model for an equilibrium boundary layer (Figures 3.11, 3.13, 5.8, 5.10). In this manner, the spectral energy production associated with the turbulent motions admits to Townsend's Reynolds similarity hypothesis (Townsend, 1976) which further reflects the equilibrium boundary layer definitions brought by Clauser (1952, 1954) and George and Castillo (1997). Collapse of the turbulence energy of the production region and thus that associated with bursting and macroturbulence is further surprising in that the energy of the scales does not appear to be dependent upon roughness conditions (see Figure 3.11 compared to Figure 5.8) for the open channel flow over a gravel bed studied in this paper. In this manner, the fluid dynamics can be predictable based on the mixed variables (u^* , y and H) used in the scaling method. Since the energy production scales are constant, the results admit to both equilibrium boundary layer and wall similarity hypothesis. While the former is reflected by the derivation of the scaling procedure, the latter is reflected by the fact that the bed surface conditions only impact the energy of the vortical scales as an indirect influence of the shear stress, the boundary layer height and the distance from the wall (Townsend, 1976). The corroboration of the turbulence kinetic production energy with Townsend's hypothesis will be convenient for applications, as will be discussed later.

Taken together, the fact that the turbulence production scales of macroturbulence and bursting (K_m and K_b) in the outer region are not dependent upon external energy input

(point 3 above, see Figures 3.10, 5.7) but are dependent upon surface conditions (point 4 above, see Figure 3.10 compared to Figure 5.7) leads us to suggesting a revision to Townsend's wall similarity hypothesis for the case of open channel flow over gravel beds. Townsend's wall similarity hypothesis (1976) suggest that vortical motions above the near-wall layers are independent of bed surface conditions except for the indirect influence of variations in roughness upon the friction velocity and boundary layer extent. This is shown to not be true in this study. K_m and K_b reach constants in the outer region for individual roughness types across hydraulic conditions but these constants are different depending on the roughness type (see Figure 3.10 compared to Figure 5.7). Rather, for the gravel bed conditions, a more likely hypothesis is that the turbulence motions above the roughness layers are similarly dependent upon surface conditions regardless of external mean energy input ($gS_e u^-$ or $u_*^2 u^- H^{-1}$) or channel aspect ratio so long as turbulent energy production and/or turbulent energy transfer remain non-zero within the flow. In this manner, the flow structure would be hypothesized to exhibit similarity if a gravel bed channel experienced changes in flow discharge and hence stage yet maintained the same channel bed morphology. However, if bed surface conditions change, so too might the similarity dependence of the macroturbulence and bursting scales, at least in the streamwise direction. Our results tend to be corroborated by the results of Amir and Castro (2011) where the authors showed that for fully rough turbulent boundary layers with $h/\delta > 0.15$ (where h is the roughness height in their study and δ is the boundary-layer thickness) that the entire flow is affected by the turbulence in the near-wall region as well as the outer region scaling for the velocity deficit by Fox and Stewart (2014) where the authors show the dependence of the flow structure on the bed characteristics for gravel bed conditions.

With our revised hypothesis in mind for gravel bed conditions, and as mentioned earlier, we tend to conceptualize the nature of the vortical structure of macroturbulence and bursting to be consistent across the range of gravel bed roughness conditions, but likely just show variation in their production angles when moving away from the bed. That is, the structure of turbulence of the open channel flow across a range of gravel sizes has tended to corroborate the conceptual model that includes the shedding and then bursting of hairpin-like packets that are organized within larger macroturbulence vortical motions across the flow depth and extending longitudinally (Schvidchenko and pending 2001; Roy et al., 2004, Fox et al., 2005; Hurther et al., 2007; Belcher and Fox, 2009). The lack of collapse for different bed roughness heights but yet the similarity dependence of the macroturbulence and bursting scales in the streamwise direction for a given roughness is interpreted to reflect the production angle of the processes. Belcher and Fox (2010, JHR) show using proper orthogonal decomposition and topological investigation that the bifurcation line associated with the macroturbulence extends from the plane of the bed at an angle on the order of 10° for a roughness height consistent with the small roughness type used here of $D_{50}=4.8$ mm. On the other hand, Roy et al. (2004) show that the macroturbulence structure extends from a gravel bed on a considerably larger angle equal to 25° for a larger roughness height equal with $D_{50}=38$ mm. The increase in production angle with roughness height agrees with the increase of K_b and K_m results with roughness height in this study because the streamwise length of the vortical motion would be ‘seen’ by the velocimetry probe for a shorter duration as the production angle increases. The variation of the production angle and hence K_b and K_m as dependent on roughness is still important in application because this in essence would dictate the relative time in which

the fluid is impacting an environmental process such as the transport time of a sediment particle by the turbulent structure vertically.

As an extension of the result of this study and comparison with the literature of coherent structures, we surmise the high connectivity of the bursting and macroturbulence motions within the flow. The existence of the small- and large-scales has definitely been associated with an organization of turbulence, such as the hierarchical organization of eddy packets into very large scale vortical structures (Liu et al., 2001). This type of organizational arrangement has sparked the long discussion of the chicken-or-the-egg concept: does shedding beget macroturbulence or does macroturbulence beget shedding? We tend to rather hypothesize the structure of bursting and macroturbulence in gravel bed rivers as the same structure in which the small- and large-scale motions are rather the manifestation of parts of the overall structure. It seems to us that perhaps this concept is inferred by Roy et al. (2004). We offer a couple of supporting, or at the least non-refuting, evidence of this high connectivity to the same structure. The fact that the turbulent kinetic energy of macroturbulence and bursting are equal to one another as realized in the variance-preserving form of the spectra plots and -1 region of the spectral energy density is really fascinating to these authors (see Figures 1.1, 3.7, 3.8). An interpretation of the constant energy region is that the bimodal spectra defined by Kim and Adrian (1999) reflects the bursting and macroturbulence that are in fact sharing the same turbulent kinetic energy because they are different regions of the same highly connected structure. The work of Belcher and Fox (2009) for gravel bed using turbulence decomposition and topological analysis via critical point theory further corroborates the connectivity concept as the source/sink analysis of the macroturbulence and bursting vortical components suggest the

transfer of turbulent momentum from the large scale to the small scale and vice versa. The flow visualization of D While external source energy (i.e., potential energy) and sink energy (i.e., turbulence dissipation) are well recognized in gravel bed rivers, mechanisms that would tend assist with fueling the transport and sharing of energy between the bursting and macroturbulence scales of the turbulence structure are less clear but would be associated with: (i) shedding and the hydrodynamic lift of shed connected vortices to directly insert and then transport vertically turbulent energy (Robinson, 1991), (ii) helicity of macroturbulence as well as the time-averaged motions associated with secondary currents that will help to transfer energy in three dimensions (Nikora, 2012, textbook), and (iii) the less studied manifestation of turbulence associated surface waves that causes fluctuations at the free surface of gravel bed changes and therefore while derived at the bursting scale would tend to result in instantaneous non-uniform flow that has been suggested to cause secondary energy production at the macroturbulence scale (Horoshenkov et al., 2013; Stewart and Fox, 2015).

As one further comment on the similarly hypothesis, we point out that the turbulence wavenumber scales (K_m and K_b) in the outer region exhibit the dependence on bed surface conditions alone, and that is they do not exhibit dependence on relative submergence. We checked this idea and we found that relative submergence that ranges from 6 to 36 for our testing does not drive systematic variation of K_m and K_b in the outer region. Obviously, others have shown the variation of vortical structures around a particle as indicative of the near-bed roughness region of a gravel bed river (Papanicolaou et al., 2011) for relative submergence less than 5, however this is a different fluid's question as studied in the present context.

In practice and for a given roughness, the results of this study provide an approach to calculate the streamwise turbulence kinetic energy of bursting and macroturbulence which show a linkage of this work to applications. The scaling of the turbulent kinetic energy and constant that is reached can be used to derive an equation for energy prediction. Further, the expressions can be re-arranged for the wavenumber scales to produce equations for the periodicity of bursting and macroturbulence. This concept is derived as

$$S_{B,M} = u_*^2 \left[\exp\left(-\frac{y}{H}\right) \right]^2 \frac{H}{c_{B,M}}, \quad (53)$$

and

$$T_{B,M} = \frac{H 2\pi}{U c_{B,M}}. \quad (54)$$

where $c_{B,M}$ are the constants that are reached in the outer region for K_b and K_m and are dependent upon roughness height. These equations are shown in Figure 7.1 and 7.2. In this manner, the bursting period (T_B) found in our results is found to be centrally located and agree very well with the range requested by Nezu and Nakagawa (1993), yet we remind the reader of the variation with roughness height. Application of these results is thus suggested for conditions that resemble the bed conditions of this study.

We admit that more research is needed across a wider range of roughness conditions to extend this study; here we only consider two roughness types. It will be important for gravel bed researchers if the present work can be extended to find a function for how K_b and K_m vary as a function of roughness height. Likely the physics of this variation is related to the angle that the macroturbulence structure makes with the streambed. For example, Belcher and Fox (2010, JHR) show using proper orthogonal decomposition and

topological investigation that the bifurcation line associated with the macroturbulence extends from the plane of the bed at an angle on the order of 10° for a roughness height consistent with the small roughness type used here of $D_{50}=4.8$ mm. On the other hand, Roy et al. (2004) show that the macroturbulence structure extends from a gravel bed on a considerably larger angle equal to 25° for a larger roughness height equal with $D_{50}=38$ mm. Further investigation for a wider range of roughness would be helpful to set scales for K_b and K_m .

In addition, the work here could be improved by further spatially-averaging of the time-series data in order to account for further variation of the bed particles across the reach of the flow section. Spatial variability of the flow structure is recognized to sometimes be pronounced laterally and longitudinally across the bed, especially when investigating a distance from the bed on the order of five times the bed particle height for which 84% of the particles are finer (Nikora et al., 2001; Franca et al., 2010). This variability is potentially reflected in the particularly high variability of K_b and K_m scaling for the large roughness type when $y/H < 0.5$. Nevertheless, the outer region for $y/H > 0.5$ does tend towards stationary mean value for the remainder of the flow depth, thus showing agreement with the trend observed for the lower roughness type. For this reason, even the lack of spatial averaging of this study is believed to give a reasonable first approximation of K_b and K_m for the larger roughness type.

Notwithstanding the future research and improvements of this work that could be built upon, we argue that the time is ripe for further application of bursting and macroturbulence energy and their scales to coupling with sediment transport processes and modeling of geomorphodynamics in gravel bed rivers. The consistency of bursting and

macroturbulence energy in this study is pronounced. Also, fact that the form and scales of the turbulent motions above the roughness layer are similarly dependent upon surface conditions regardless of external energy input (i.e., variation in S longitudinally and Q and thus H in time) provides a result of the similarity of scales for a given river with a fixed roughness height. The energy, along with approximation of the bursting and macroturbulence period, could be connected with bedload and suspended load transport processes in an effort to more succinctly couple the energy for transport with resistance of particles to transport. Functions for streampower associated with the sediment transport carrying capacity of the flow (i.e., $\tau_b V$, $\tau_b^{1.5}$, or V^3) still provide the prevailing method for interpreting and predicting sediment transport in rivers. This method is highly calibrated in practice based on measurements, and while fundamental in nature due to its reflection of energy, the method alone is not closing the gap on our understanding between fluid processes and sediment. The energy of the dominant production scales, such as those presented here, provides perhaps a more fundamental context in which the energy of bursting and the energy of macroturbulence can be used to help predict the rates of bedload and rates of suspended load, respectively, longitudinally in a river system.

Finally, we highlight the method advancements used in this study that should be carried forward, or at the very least considered, in future research that focuses on the macroturbulence scale. First, we highlight the number of data collected in this study. Our results of this study rely on 49 million data readings of velocity. Is such an exhaustive amount of data needed? Perhaps for macroturbulence. Specifically, we collected 30 minute, or 90,000 data, of three dimensional velocity at each point in the flow for which data was collected. The macroturbulence period (T_M) in the outer region found in this study

varied on the order of 1 to 2 seconds depending on the mean streamwise velocity and flow depth. Therefore, we were able to collect 1,000 to 2,000 repetitions of a macroturbulence cycle that passes the velocity probe and we investigated and resulting from our spectral analysis. 1,000 realizations of a process seems reasonable, and we investigated the sensitivity of the number of data to produce consistent spectral results for K_m and found K_m to stabilize at a value equal to approximately 50000. Such a rather long duration of sampling is recommended in the future when studying macroturbulence in the laboratory, but this is a bit of a conundrum in the case of field measurements because we will require long time to take measurements which can be difficult when flow can be varied such as over the course of hydrograph. Regulated gravel bed rivers with controlled dam releases offer the opportunity for full-scale experiments and should be targeted for such studies. Related, we also offer caution when attempting a macro-analysis of the period of macroturbulence by observing the low wavenumber boundary of the -1 power region from the spectral graphs of other studies of gravel bed rivers. Many of previous gravel bed studies in the laboratory collect velocity time-series data for one to five minutes (e.g., Fox and Papanicolaou, 2005). Surely, such a few minute time duration can be justified as has been done by the second author of this work and a number of other prominent studies, and in such studies it is show that one minute is sufficient to provide stabilization of the statistical moments of the turbulence data (Nikora and Goring, 2000; Fox, 2002; Buffin-Belanger and Roy, 2005). However, in the present study, a one minute time series will only capture 30 to 60 cycles of macroturbulence that past the velocimetry instrument, and such low numbers may lead to variation in the estimating of K_m .

A second method advancement that should be highlighted is the consideration of the type of spectral smoothing used that can impact the interpretation of K_m and K_b . We are not the first authors to investigate the bounds of the -1 power region that are associated with large- and smaller-scale production. And, the investigations of the boundary of the -1 power region for open channel flow (Nikora and Goring, 2000) and of the low wavenumber and high wavenumber bound associated with the large and small-scale for turbulent pipe flow (i.e., scales A and B in Kim and Adrian, 1999) were pivotal to the development of this work. But, our investigating of the smoothing, and specifically the use of both the un-smoothed and smoothed spectral plots in both spectral energy density and variance-preserving form might be adopted in future work. The use of un-smoothed spectra alone was obviously noisy and could be difficult to infer the edge of the -1 power region. At the same time, the use of smoothing windows for removing fluctuations has become heavily utilized, if not standard, in spectral analysis research. However, the use of smoothed spectra alone has the problem of the energy associated with K_m and K_b falling away from the -1 slope in the spectral energy density, which could prompt the researcher to over-predict K_m and under-predict K_b . For this reason, we will recommend our four-plot spectral method for selection of K_m and K_b in future work.

CHAPTER 7 TABLES AND FIGURES

Figure 7.1. Plot of the equation developed for energy prediction for small flume. (a) energy prediction of macroturbulence, (b) energy prediction of bursting

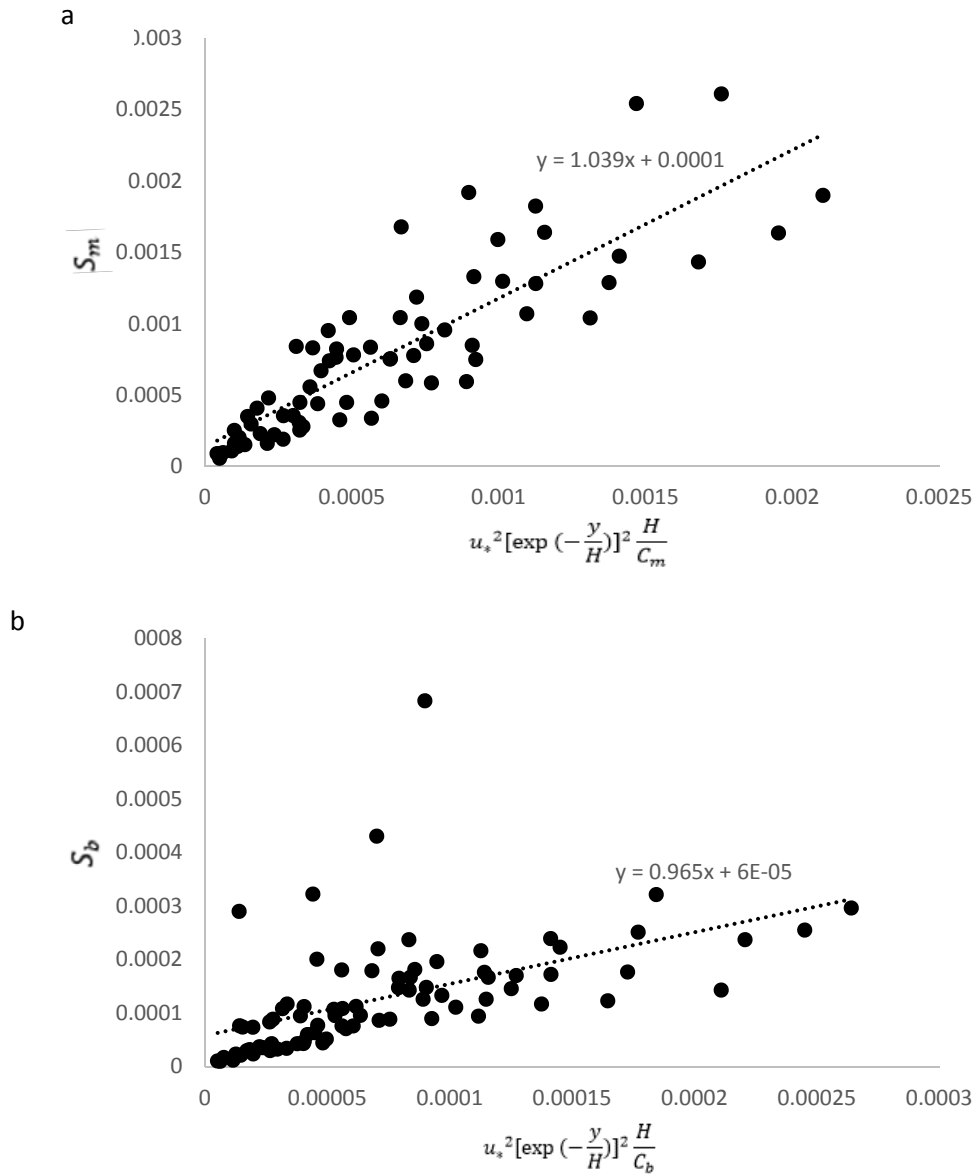


Figure 7.2. Plot of the equation developed for periodicity prediction for small flume. (a) Periodicity prediction of macroturbulence, (b) periodicity prediction of bursting

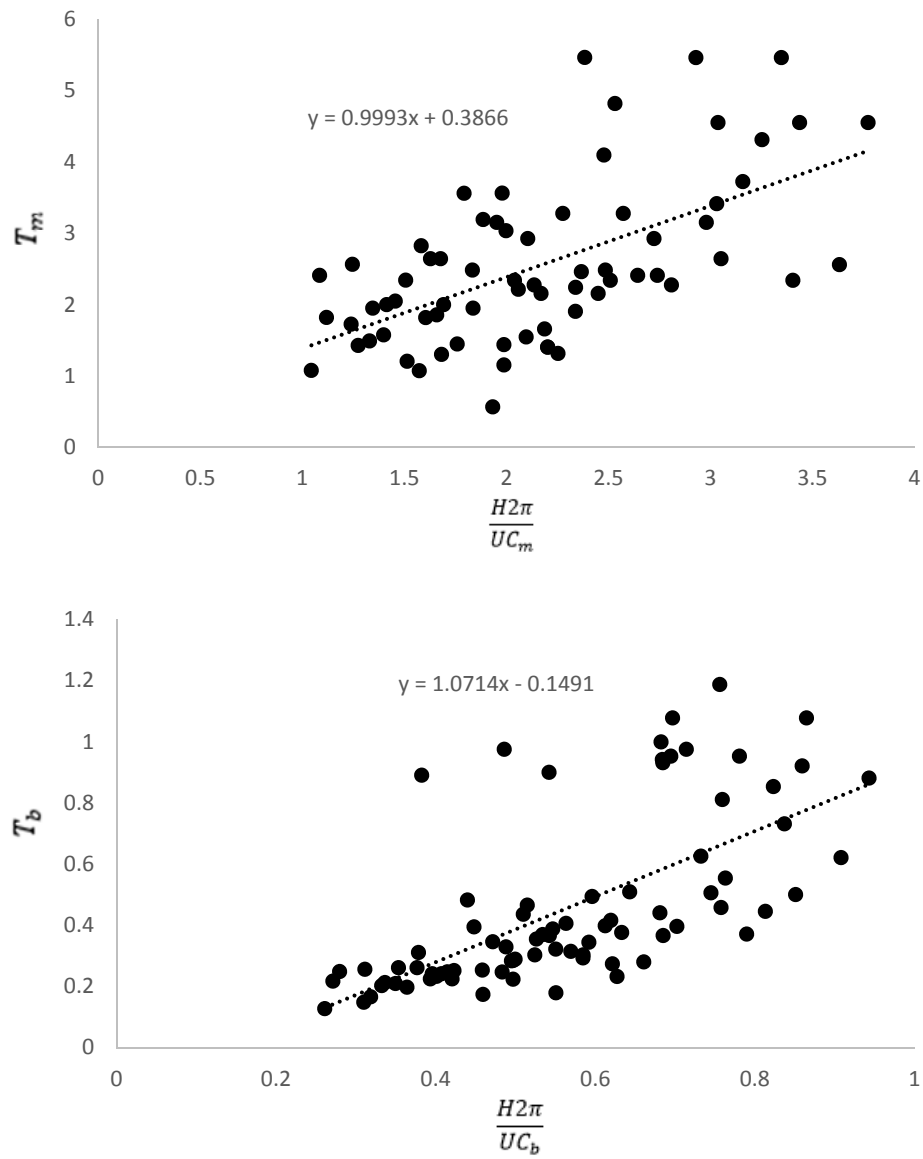


Figure 7.3. Plot of the equation developed for energy prediction for large flume. (a) energy prediction of macroturbulence, (b) energy prediction of bursting

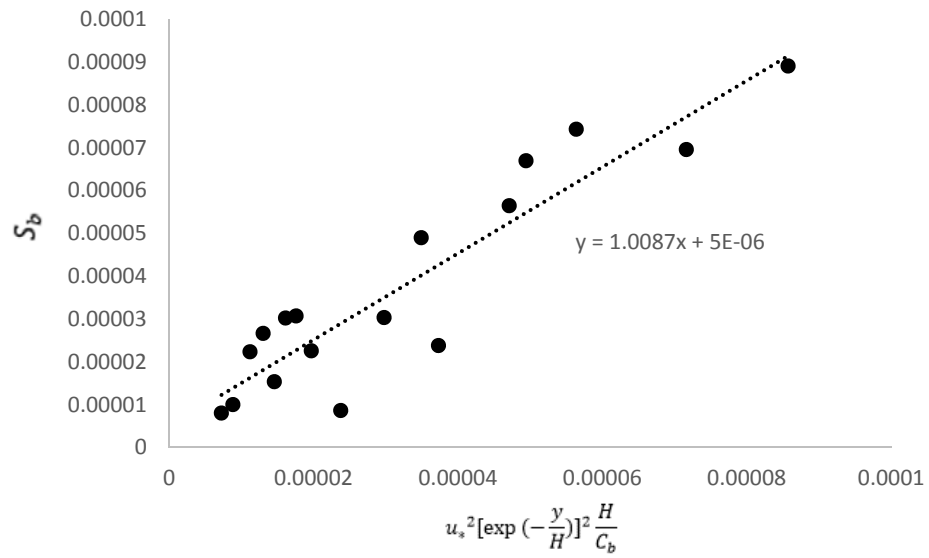
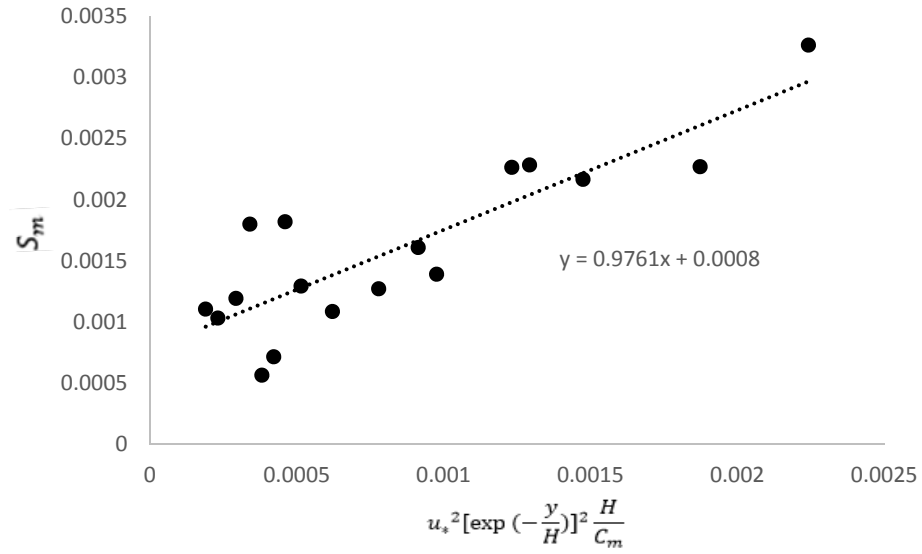
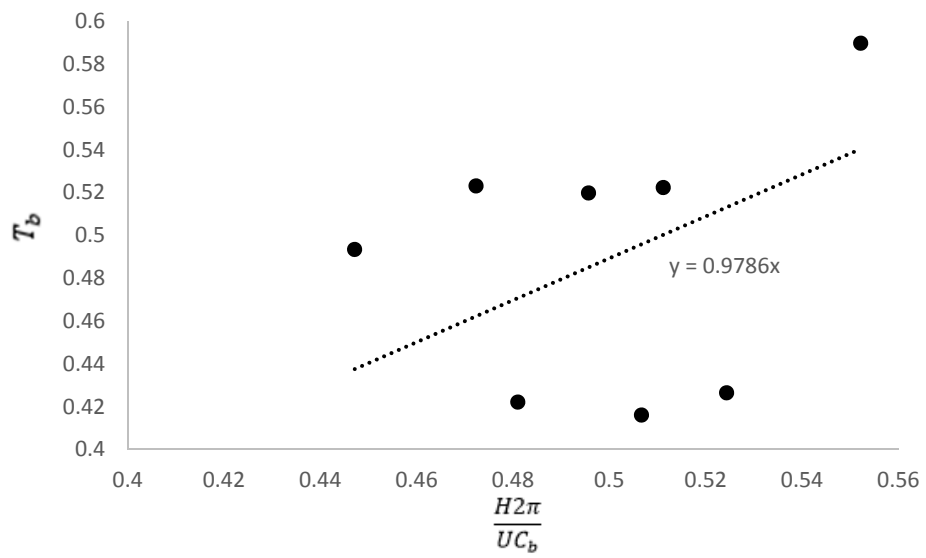
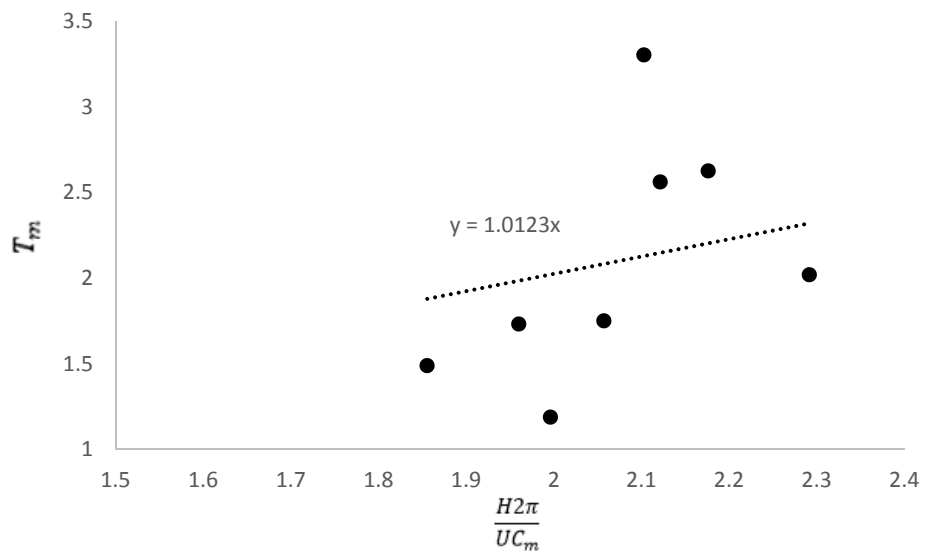


Figure 7.4. Plot of the equation developed for periodicity prediction for large flume. (a) Periodicity prediction of macroturbulence, (b) periodicity prediction of bursting



Chapter 8 Conclusion

The conclusion of this work points to several key results highlighted as follows:

1. The time-average laboratory test results for open channel flow of water over a rough gravel bed scenario suggest an equilibrium boundary layer for the outer region of the flow in which the flow is uniform and fully-developed, which is in agreement with a number of previous studies.

2. Turbulence production also admits to the definition of an equilibrium boundary layer for the outer region; and the energy associated with turbulence production that is indicated by the -1 power region of the spectra as well as the turbulent energy associated with bursting and macroturbulence best collapse when scaled with the scaling law derived from the turbulence energy model for an equilibrium boundary layer, which is a new contribution to the literature.

3. For a fixed roughness type the scales of K_m and K_b reach similarity in the outer region, regardless of external energy input or aspect ratio of the open channel flow suggesting that the form of macroturbulence and bursting behave similarly for different hydraulic conditions.

4. The energy production scales associated with K_m and K_b show dependence upon the roughness characteristics, even in the far-wall outer region of the flow.

5. In practice and for a given roughness, the results of this study provide an approach to calculate the streamwise turbulence kinetic energy of bursting and macroturbulence which show a linkage of this work to applications such as bedload and suspended load sediment transport.

6. The methods developed in this study provide further considerations for others including a need for high amount of data to study macroturbulence and the use of the four-plot method for K_m and K_b identification.

Appendix I – Index

List Of Symbols

B	=	flume width
B/H	=	aspect ratio
$D_{u,v,w}$	=	empirical coefficients for streamwise, vertical, and transverse turbulent intensities
D_{50}	=	particle diameter for which 50% of particles are finer
D_{84}	=	particle diameter for which 84% of particles are finer
Fr	=	$U_m(gH)^{-1/2}$ is the Froude number
g	=	gravitational acceleration
H	=	flow depth
H/k_s	=	relative submergence
K	=	wave-number
K_b	=	wave-number associated with bursting
K_m	=	wave-number associated with macroturbulence
K^+	=	$k_s U_* v^{-1}$ is the shear Reynolds number
R	=	hydraulic radius
Re	=	$U_m H \nu^{-1}$ is the Reynolds number
$RMS(u)$	=	root mean square of streamwise velocity fluctuations
$RMS(v)$	=	root mean square of vertical velocity fluctuations
$RMS(w)$	=	root mean square of spanwise velocity fluctuations
S	=	slope
$S(K)$	=	spectral energy

S_b	=	spectral energy density associated with bursting
S_m	=	spectral energy density associated with macroturbulence
$S(K)$	=	streamwise spectral energy density
TKE	=	turbulent kinetic energy
T_B	=	bursting period
T_M	=	macroturbulence period
U	=	time-averaged streamwise velocity component
U_{max}	=	maximum streamwise velocity
V	=	time-averaged vertical velocity component
V_{mag}	=	magnitude of the time-averaged velocity vector
V_x	=	instrument streamwise velocity
V_y	=	instrument spanwise velocity
V_z	=	instrument vertical velocity
W	=	time-averaged transverse velocity component
X_k	=	frequency domain
f	=	frequency
f_s	=	sampling frequency
k_s	=	equivalent roughness height
$nfft$	=	number of grid points in spectral calculations
p	=	pressure
pxx	=	spectral energy density calculated from Pwelch function in MATLAB
t	=	time
u	=	instantaneous streamwise velocity component

u_0	=	velocity scale
u'	=	instantaneous fluctuating component of streamwise velocity
u^+	=	dimensionless velocity, $u^+ = \frac{u}{u^*}$
$u^*_{\sqrt{gRS}}$	=	friction velocity estimated by $u^* = \sqrt{gRS}$
$u^*_{log-law}$	=	friction velocity estimated by using the log-layer of streamwise velocity profile
u^*_{Rey}	=	friction velocity estimated by using $\overline{u'v'}$ data
$\overline{u'v'}$	=	primary Reynolds shear stress component
$\overline{u'w'}$	=	secondary Reynolds shear stress component
v	=	instantaneous wall normal velocity component
v'	=	instantaneous fluctuating component of wall normal velocity
$\overline{v'w'}$	=	secondary Reynolds shear stress component
w	=	instantaneous transverse velocity component
$width$	=	smooth width used in 'fastsmooth' function
w'	=	instantaneous fluctuating component of transverse velocity
x_n	=	velocity data
y^+	=	dimensionless distance to the bed, $y^+ = \frac{yu^*}{\nu}$
x,y,z	=	stream wise, wall normal, and transverse directions
Π	=	Coles wake strength
κ	=	von Karman constant
ρ	=	water density
μ	=	Dynamic viscosity of water

ν = Kinematic viscosity of water

V_t = eddy viscosity

ω = vorticity vector, $\frac{\partial \bar{u}_j}{\partial \bar{x}_i} - \frac{\partial \bar{u}_i}{\partial \bar{x}_j}$

Appendix II – Procedure data collection and processing

AII.1. Procedures for running the flume

Terms Used:

- Gate-valve: The valve in the middle of the inlet pipe.
- Head-box: Box at the entrance of the flume.
- Outlet-valve: The valve in the middle of the outlet pipe.

Procedure:

- Close both the gate-valve and outlet-valve.
- Vacuum air from the pipe connecting the source of water to the pump using the vacuum line, until water comes out of the suction line valve.
- Once water comes out of the suction line valve, close the valve.
- The flume is now ready for running.
- Turn the motor pump to the ON position and wait about 15 seconds.
- Now, slowly open the gate-valve and wait the flow stabilizes before taking any measurements.

AII.2. Procedure for setting up the Sontek ADV instrument for data collection:

- Install Horizon ADV software version 1.20 onto the PC.
- Plug in the long black cable into the electronic case (yellow case).
- Plug in the switching AC adaptor into the DC port of the electronic case.

- Plug in the serial cable (gray cable) to the electronic case, then plug this into the USB port of the PC.
- Plug in the long black cable into the probe.
- Turn on the power button on the electronic case.
- Now the ADV is ready for collecting data.

AII.3. Procedure for preparing the flume for collecting data with the Sontek ADV and Nortek Vectrino Profiler (depth of water: 10-11 cm):

AII.3.1. Use the down-looking probe orientation to collect data from locations starting at the bed ($y = 0$) and extending to $y = 4$ cm.

- Secure the clamp to the 3 cm diameter rigid section of the probe near the ADV receivers. For the Nortek Vectrino Profiler, secure the clamp to the rigid section of the probe near the Vectrino receivers. (Note: Do not secure clamp to the flexible portion of the probe stem. Clamping the flexible stem can damage the ADV and Vectrino Profiler instruments.
- Extend the guide rod to the bed to prevent vibrations. The end of the guide rod should be secured into a predrilled hole in the bed. At the lowest location for collecting data, the guide rod will extend 6 cm into the bed. The instrumentation apparatus can be moved upward in the vertical a distance of 6 cm. Therefore, the guide rod is always within the predrilled bed hole, and thus prevent vibrations.
- Place the control volume at the $y = 0.1$ cm position by placing the transmitter a distance of 5.1 cm from the bed. For the Nortek Vectrino Profiler, use the bottom

check option in the vectrino profiler software to check the distance of the transmitter from the bed.

- Adjust the probe orientation so that the stream-wise receiver, which is the receiver with the red label, is horizontal. Use a level to orient the probe stem to the vertical.
- Adjust the probe orientation so that the stream-wise receiver is in the direction of the flow. Measure two points on the receiver from the wall and be sure that both of them have equal distance from the wall.
- Run the flume. (see section AII.1)
- Measure the height of the screw on the gate-valve. Open or close gate-valve as needed.
- Measure the depth of water in the reservoir near the pump and be sure that it does not change.
- Wait until the flow stabilizes. Stability will be reached when variation in the average velocity values becomes minimum. Recently we waited 1 hour.
- Start collecting data with the Horizon ADV. (see section 3.4)
- Use the control module to run the motor or adjust both the probe and the guide rod by hand to a new vertical position.

AII.3.2. Use the side-looking probe orientation for points from $y = 3.5$ cm to $y = 9$ cm

- Secure the clamp to the 3 cm diameter rigid section of the probe near the ADV receivers. For the Nortek Vectrino Profiler, secure the clamp to the rigid section of the probe near the Vectrino receivers. (Note: Do not secure clamp to the flexible portion of the probe stem. Clamping the flexible stem can damage the ADV).

- Move the probe from the center of the flume and set the transmitter distance from the center to 5 cm to measure the velocity of points in the center.
- Extend the guide rod to the bed to prevent vibrations. The end of the guide rod should be secured into a predrilled hole in the bed. At the lowest location for collecting data, the guide rod will extend 6 cm into the bed. The instrumentation apparatus can be moved upward in the vertical a distance of 6 cm. Therefore, the guide rod is always within the predrilled bed hole, and thus prevent vibrations.
- Place the control volume at the $y = 3.5$ cm position.
- Use a square to orient the probe stem so that it is vertical to the direction of the flow. Thereafter, the stream-wise receiver is in the direction of the flow.
- Use a ruler to measure the distance of two different points on the probe stem and be sure that both of them have equal distance from the bed.
- Run the flume. (see section 3.3)
- Measure the height of the screw on the gate-valve. Open or close gate-valve as needed.
- Measure the depth of water in the reservoir near the pump and be sure that it does not change.
- Wait until the flow stabilizes. Stability will be reached when variation in the average velocity values becomes minimum. Recently we waited 1 hour.
- Start collecting data with the Horizon ADV. (see section 3.4)
- Use the control module to run the motor or adjust both the probe and the guide rod by hand to a new vertical position.

AII.4. Procedures for collecting data with the Sontek ADV instrument using the Horizon ADV software

- Install the Horizon ADV software version 1.20 onto the PC. You can download the software from the Sontek website.
(<http://www.sontek.com/software/detail.php?HorizonADV-15>)
- Open the Horizon ADV software.
- Click on the ‘Connect to ADV automatically’ option.
- In the new page, you can change the ADV settings. To change your ADV settings, click on the ‘change’ button in the ‘system settings’ category. The description and guidelines of these options are as follows:
 - Velocity range: It determines the maximum velocity that can be measured by the ADV. A Higher velocity setting will have higher variability for any low velocities that are measured. It is recommended to set the velocity range to 250 cm/s or 100 cm/s.
 - External sync: By default, this should be disabled.
 - Other settings: In most situations you will not need to change any of the parameters in this dialog.
- You can also change data collection settings. The data collection category contains the settings related to the frequency, mode, and method of data collection. These settings can be changed by clicking the ‘change’ button. The description and guidelines for each of these options are as follows:

- Sampling rate: This is the rate at which the velocity data will be collected. The maximum sampling rate for the micro ADV is 50 Hz, and it is recommended to record your data using frequency.
 - Recording Mode: The Recording Mode can be set to either ‘continuous’ or ‘Burst’. Continuous mode is used for sampling regularly without any breaks or interruption. Burst mode is used to collect samples in sets at regular time intervals. Burst mode requires the input of additional parameters: ‘sample per burst’ and ‘Burst interval’. It is recommended for beginning users to start with the continuous sampling option.
 - Output File and Output Folder: These parameters are used to select the name and destination of the output file that will be created during real-time data collection.
 - File comments: These lines of text are used to describe briefly the details of your data collection parameters, location, environment, etc.
 - Show boundary info: With this option enabled, the ADV will first scan the region in front of each probe to detect the presence of a solid or surface boundary.
 - Click ‘save’ to save your settings.
- Click on the ‘start’ button.
 - Click on the ‘start recording’ option to record your data.
 - Click on the ‘stop recording’ option to stop recording your data.

AII.5. Procedure for post-processing the Sontek ADV data using WinADV

- Install the WinADV software version 2.031. You can download the WinADV software from the following address:
(http://www.usbr.gov/pmts/hydraulics_lab/twahl/winadv/index.html)
- Import the .adv file collected with the Horizon ADV into the Win ADV program. In order to do this, click on the file tab and then click on the ‘open new ADV file’ option and then import your ADV file.
- Click on the option tab and go to the filtering option.
- Activate the following filtering options. The description and guidelines for thresholds of these options are as follows:
 - The signal to noise ratio (SNR) parameters indicates the relative density of acoustic scatters in the flow and the resulting strength of the signal received compared to the noise level of the instrument. ADV manufactures recommend a SNR value of at least 5 when measuring average flow velocities and 15 or higher when measuring instantaneous velocities and turbulence quantities.
 - The correlation parameter, COR, is an indicator of the relative consistency of the behavior of the scatters in the sampling volume during the sampling period. The value varies from 0 to 100, and ADV manufactures have typically recommended filtering to remove any samples with correlation scores below 70.
 - The last option WinADV provides for modification of the data is despiking option. WinADV allows users to despike their data with two different methods; (1) Acceleration spike filter which you can specify the coefficient.

This method is based on the visual inspection that is not possible to have a flow acceleration greater than the gravity acceleration, otherwise the ejection of particles could be seen. (2) Phase-space threshold despiking which is highly recommended by authors. This method first developed by Goring and Nikora and is based on plotting the velocity components against their derivatives and remove spikes which are the points lie outside of an ellipsoid. Wahl believes, sometimes, replacing spikes cause to produce spikes again. Based on this WinADV does not replace the spikes detected by Phase-space threshold method. This method would not cause any problems when average turbulence parameters is calculated but caution is required when spectral density is calculated because the gaps in the signal after despiking could cause problems. In order to avoid any problems during spectral analysis, detected spikes should be replaced which will be explained later in this section.

- After activating suitable filtering options, click on the ‘process’ button. Then, activate the ‘compute summary statistics’ and ‘produce time series data file’ options for filtered data. Then, click ‘Go’.
- WinADV gives us two files. One is filtered.sum, which is the summary statistics, and the second is default0001.Vf, which is time series of filtered data.
- In order to calculate the average parameters, import the time series of filtered data (default0001.Vf) into the Excel. Then, filter the blank cells in the velocity components (V_x , V_y and V_z).

- Copy and paste the filtered data into the new Excel spread-sheet and see if any orienting, rotating or shifting is required. The procedure for orienting, rotating and shifting will be described in the next sub-section.
- Calculate the average velocities and turbulence parameters.

AI.6. Procedure for setting up the Nortek Vectrino Profiler II instrument for data collection:

- Install Vectrino Profiler software version 1.32 onto the PC. The Vectrino Profiler acquisition software requires a Java virtual machine (JVM) to operate.
- Plug in the signal cable (blue cable) into the converter (RS422 Altronix AL310 converter)
- Plug in the AC adaptor into the black port which comes out of the signal cable.
- Plug the serial cable (gray cable) into the converter, then plug the gray cable into the USB port of the PC.
- Plug the signal cable into the probe.
- In order to properly connect to the instrument, the following must be performed: Go to the Device manager by right clicking on the computer icon on the start menu, then click on the 'manage' option. Then, click on the 'device manager' option and then right click on the 'USB serial port (COM5)' and choose 'properties' option. Then, click on the 'port setting' tab and after that click on the 'advanced' option and set the 'Latency Timer' to 5 msec which is recommended by Nortek because at high sampling rate (above 60 Hz), the driver parameters need to be tuned to provide an

adequate display rate for the application software. Faster systems should be able to use 2 msec. (SW User Guide)

- Now the Vectrino Profiler II is ready for collecting data.

AII.7. Procedures for collecting data with the Vectrino Profiler II instrument using the Vectrino Profiler software

- Install the Vectrino Profiler software located on the USB memory stick. Also, you can download the software from Nortek website. (<http://www.nortek-as.com/en/support/software>).
- Open the Vectrino Profiler software.
- Click on the ‘communication’ tab. Then click on the ‘connect’ option and then choose Vectrino Profiler.
- Select the appropriate serial port and port speed (937500) and press ‘Apply’.
- Run a transducer test in accordance with the procedure described in the **Vectrino Profiler User Guide** to verify that the instrument is working as expected. (Nortek Quick Guide). The procedure is described below:
 - Fill a bucket with water and a little dirt.
 - Click the ‘Start Collecting Data’ button. While the transducers are in the air, the velocity measurement will look like random noise.
 - Immerse the transducers in the water, and observe the velocity, the standard deviation, and the amplitude and note the change in the graphical view of the velocity when the probe is lowered into the water.

- Test the measurement quality with the Probe Check function: Open **Configuration**; tick the **Probe Check** and **Start Data Collection**. (Nortek Quick Guide). This option produce long average amplitude vs. range profiles for each beam when data collection is started. If a transducer arm is not damaged or bent, it is expected that all four profiles are roughly the same, with similar peaks and shapes at the same range. (SW User Guide)
- Click the ‘configuration’ button to activate the dialog for configuring the instrument velocity settings, bottom check settings and disk file parameters. A detailed description of each submenu and each parameter can be found in the **SW User Guide**. (Nortek Quick Guide) but here a brief description of above parameters is given:
 - **File Parameter**: This menu configures where and how data should be saved on the PC.
 - **Bottom Check**: This menu, if is activated, gives the distance of the transducer to the bed at a given sampling interval.
 - **Velocity settings or Doppler**: This menu configures the sampling rate, velocity range, the range of sampling volume and the coordinate system.
- Click on the ‘start collecting data’ option.
- Now, instrument starts to collect data. You can save your data by clicking on the ‘save collected data on the disk’ button.
- Click on the ‘stop collecting data’ option when adequate amount of data is collected. Vectrino Profiler software gives a file that can be used to export data into the MATLAB or EXCEL format.

AII.8. Procedure for post-processing the Vectrino Profiler II data using Multi Instrument Turbulent Toolbox (MITT)

- Export your saved data by clicking the ‘data’ tab in the Vectrino Profiler software. (It is recommended to export data into the MATLAB format because of the large amount of data)

- Download the MITT codes.

(<http://www.mathworks.com/matlabcentral/fileexchange/47805-mitt>)

- Before the MITT is started, the user must create a CVS control file using the format describe in MacVicar 2014 paper. (Multi-instrument Turbulence Toolbox (MITT): Open-source MATLAB algorithms for the analysis of high-frequency flow velocity time series datasets). In order to create a CVS file using Microsoft Excel, the following steps should be done:

- Open Microsoft Excel.
- In the first row, type the ‘filename’ and any other information related to the data such as water depth or instrument locations in different column.
- In the second row, type the format string of parameters which are typed in the first row. Format strings must be in matlab format (e.g. %s for a string, %d for an integer, and %f for a floating point real number (Macvicar 2014)).
- In the next rows, type your file names and information related to them.
- Go to the ‘file’ menu and select ‘Save as’.
- Save as type CVS (comma delimited).
- Click ‘Save’.

- Open MATLAB and open the directory where the MITT programs are located.
(Macvicar 2014)
- Run the MITT. The MITT launch window opens.
- Click the ‘select File’ box. This opens a browser window to search for the CVS control file. (Macvicar 2014)
- Click on the ‘Organize raw data into Data and Config array’ and ‘Clean raw time series’ options. Doing this will open other options.
- In the ‘Organization block options’ tick the ‘Custom algorithm to define sampling locations’, then select the ‘CalcXYZUWFlume’ from where MITT files located. This option is provided for instruments which can collect multi points at the same time. Also, you can define the channel geometry by ticking the ‘Define channel geometry’ option.
- In order to clean data collected with Vectrino II, different filtering and despiking methods are provided in MITT, which are briefly described below; after describing the methods, we provide our recommendations.
 - **Despiking Methods:**
 - Standard deviation: This method is based on fixing the maximum and minimum velocity, then remove velocities larger than specified value. Fixed maximum and minimum values can be determined by using the following equation (MacVicar 2014): $u_T = U \pm C_1 \lambda S_u$ where U is the mean velocity, S_u is the standard deviation, C_1 is a user specified constant, and λ is the ‘universal threshold’ which is for random

white noise is equal to $\lambda = \sqrt{2 \ln n}$ where n is the number of independent samples.

- One side skewness: This method fixes maximum and minimum velocity using the following equation (Macvicar 2014): $u_T = U_{median} \pm C_2 \lambda S_u^*$ where U_{median} is the median velocity, S_u^* is the ‘one-sided’ standard deviation calculated from the data on the side of the median that has lower variability and C_2 is a user specified constant.
- Phase space: This method is based on plotting the velocity components against their derivatives and remove spikes which are the points lie outside of an ellipsoid. (Goring and Nikora 2002) It is recommended to tick the ‘freeze good data’ option when using the phase-space threshold method for despiking because it keeps the good data which are those adjacent to the spikes. If ‘freeze good data’ option is not activated then data that adjacent to the spikes determined as spikes and MITT will remove them.
- Velocity correlation: This method is based on the idea of phase space filtering method but instead of plotting velocity components against their derivatives, it plots the three velocity components against each other (Cea 2007). One of the advantage of this method is that, no replacement is done until we want to do the spectra analysis and it is recommended in the highly turbulent flows.
- Filtering Method:

- Low pass third order Butterworth: This method is based on removing the Doppler or white noises above Nyquist frequency (one half of sampling rate). (Macvicar 2014)
- We recommend to use ‘phase space threshold’ for calculating the average and turbulence parameters because this method not only works well for despiking the data but also is independent of any coefficients which are used in ‘standard deviation’ and ‘One side skewness’ methods. For doing spectra analysis, which we will explain in details further, we recommend to use ‘phase space threshold’ method for despiking and ‘Low pass third order Butterworth’ method for filtering.
- For calculating the average and turbulence parameters, it is recommended to remove spikes and not replacing them with anything (interpolation values, mean values,...) while for the spectra analysis it is necessary to replace spikes. MITT provides only one replacing option which is linear interpolation. Since MITT is an open source, you can change the replacing method as you wanted. For average parameter calculations, we changed the MITT code in order to not replacing spikes while for spectral analysis we use the original code for phase-space method which replace spikes with a linear interpolation.
- After the appropriate despiking and filtering methods is chosen (It is recommended to activate phase-space despiking method with freezing option and not activate filtering option), click ‘Run Analysis’ button.

MITT will give you a file (.mat format) which contains the raw data and clean data. You can use this file for further analysis.

AII.9. Procedure for orienting and shifting the Sontek ADV and Nortek Vectrino Profiler data

- Determine the flow field coordinate system (u = stream-wise, v = vertical, w = span-wise)
- Change the ADV and Vectrino Profiler coordinate systems (V_x, V_y, V_z) into the flow field coordinate system (u, v, w). For down-looking data: $u = -V_x$, $v = V_z$, $w = -V_y$ and for side-looking: $u = -V_x$, $v = V_y$, $w = -V_z$.
- Shift the down-looking data until TKE and V_{mag} are equal to zero at $y = 0$ cm.

AII.10. Procedure for plotting time-average turbulence parameters

- Import time series data output Win ADV gives you into an excel spreadsheet. For the Nortek Vectrino Profiler, develop a MATLAB code for analyzing the clean data acquired by MITT and calculating the time-average turbulence parameters.
- For the Nortek Vectrino Profiler, copy and paste the time-average parameters calculated by the developed MATLAB code for each profile into the Excel spreadsheet.
- Change the ADV coordinate system to your coordinate system as described in step 2 of section AII.9. For the Vectrino Profiler II, it is easier to implement these changes in the developed MATLAB code.
- Apply the correction factor to the side-looking data, if it is necessary, to make the side-looking data consistent with down-looking data.
- Calculate turbulent kinetic energy (TKE) for each point for the data collected by the ADV. $(TKE = 0.5 * ((RMS(V_x'))^2 + (RMS(V_y'))^2 + (RMS(V_z'))^2))$

- Calculate Reynolds stresses ($\overline{u'v'}$, $\overline{u'w'}$, $\overline{v'w'}$) from the 'time series of filtered data' excel file Win ADV gives you.
- Calculate turbulence anisotropy ($\overline{v'^2} - \overline{w'^2}$) for each point.
- Plot \bar{U} for the whole profile collected with different styles (down-looking, tilt-looking, side-looking) in one graph.
- Plot \bar{V} for the whole profile collected with different styles (down-looking, tilt-looking, side-looking) in one graph.
- Plot \bar{W} for the whole profile collected with different styles (down-looking, tilt-looking, side-looking) in one graph.
- Plot V_{mag} for the whole profile collected with different styles (down-looking, tilt-looking, side-looking) in one graph.
- Plot TKE for the whole profile collected with different styles (down-looking, tilt-looking, side-looking) in one graph.
- Plot $\text{RMS}(V_{x'})$ for the whole profile collected with different styles (down-looking, tilt-looking, side-looking) in one graph.
- Plot $\text{RMS}(V_{y'})$ for the whole profile collected with different styles (down-looking, tilt-looking, side-looking) in one graph.
- Plot $\text{RMS}(V_{z'})$ for the whole profile collected with different styles (down-looking, tilt-looking, side-looking) in one graph.
- Plot $\overline{u'v'}$ for the whole profile collected with different styles (down-looking, tilt-looking, side-looking) in one graph.
- Plot $\overline{u'w'}$ for the whole profile collected with different styles (down-looking, tilt-looking, side-looking) in one graph.

- Plot $\overline{v'w'}$ for the whole profile collected with different styles (down-looking, tilt-looking, side-looking) in one graph.
- Plot turbulent anisotropy for the whole profile collected with different styles (down-looking, tilt-looking, side-looking) in one graph.

AII.11. Procedure for spectral analysis

- As noted before, caution is required when using WinADV to analyze the data because WinADV would not replace spikes detected from phase-space method. This non-replacing method provided in WinADV causes problems when spectral analysis is required because they change the property of the signals. In order to avoid this problem, the spikes detected from phase-space method should be replaced. The way we suggest is to import the time series of filtered data (default0001.Vf) into the MATLAB and write a code to replace the blank cells (or spikes) in the file with the previous cell. For the Nortek Vectrino Profiler II, replace the spikes by the option provided in the MITT.
- We developed a MATLAB code based on pwelch function to do spectral analysis. Pwelch is a function in MATLAB that estimates the power spectral density (PSD) of a given signal using the Welch's method. Welch method is a modified version of periodogram method developed by P.D.Welch. Base on this method, the signal is segmented into different groups with the same length. It is possible for sections to have overlaps. Then a weighted factor (window) is multiplied to each data point in each segments. After this the Fourier transforms of each segments is calculated and K modified (if we have k segments) periodograms is obtained. The spectral estimate is

the average of these periodograms. Window function is basically act on raw data to reduce the FFT leakage. Leakage is the information gained from spectral at wrong frequencies.

- The form of Pwelch function we used is the following form:

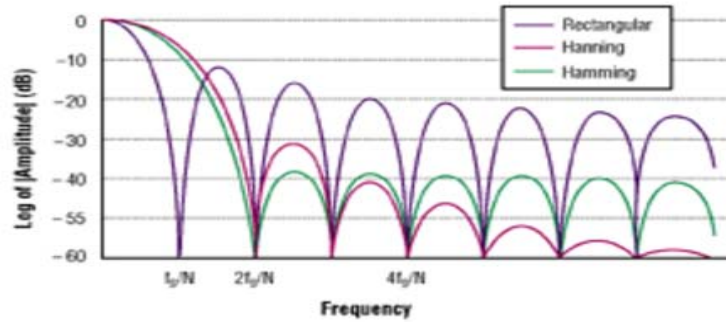
$$[p_{xx},f] = pwelch(x,window,noverlap,nfft,fs)$$

By default, pwelch divides the original signal into eight groups with 50% overlap. It uses the Hamming window by default. If an empty vector [] is used for nfft, then pwelch adopts the default value which is the greater value between 256 and the next power of two greater than the length of each segments. The length of pxx and f depends on nfft. If nfft is even then the length of pxx would be equal to $nfft/2+1$. Otherwise, the length of pxx would be equal to $(nfft+1)/2$. The length of 'f' is equal to the length of pxx. The units of 'f' is Hz and the unit of power spectral density (PSD) is power per Hz. The sampling frequency would be fs and if an empty vector [] is used, fs would be equal to 1 Hz by default.

- We recommend to use following values for pwelch parameters described above:
 - Window: we recommend to use a value in the range 2000-3000 because not only this length of window cover the necessary information but also make the spectral representation clearer and smoother. We also recommend to use the hanning window because it has less leakage to the next frequencies compare with other windows like Hamming, rectangular, etc. The Hanning window follows the following distribution:

$$\text{Hanning window} = 0.5 - 0.5 \cdot \cos(2\pi n/N)$$

Although Hanning window has a small leakage to the next bins but its main lobe is twice as wide as the main lobe of rectangular window and it is shown in the following figure.



In our case, we focus on studying the different regions of spectral corresponding to different frequencies. Based on this, it is much more important for us to have less leakage in other frequencies associated with their adjacent frequencies rather than a good representation of a specific frequency.

- noverlap: We recommend to not using any overlaps since it would smooth our signals more than what is needed.
- nfft: We recommend to use the default value for this parameter which is as stated above the greater value between 256 and the next power of two greater than the length of each segments.
- fs: This parameter should be your sampling frequency which in our case is 50 Hz.
- In our results, spectral plots is represented in two different formats: (1) power spectral density, (2) variance preserving form. What is described above is related to the former format of spectral plots. In order to get the latter format,

pxx should multiply by frequency 'f' and then plot the new series against the frequency series in semi-log scale.

- After calculating the spectral of the signal and before plotting the spectral in any of two forms described above, it is required to smooth the spectral. In order to smooth spectral, it is recommended to use fastsmoothing function in MATLAB. This function apply low pass filtering to the spectral results. The form of this function which is used by authors is shown below:

$$yy = \text{fastsmooth}(y,w,\text{type})$$

where y is the spectral results acquired from pwelch function, w is the smooth width and 'type' determines the smoothing type. Three smoothing types is provided in fastsmoothing function. Type 1 gives a rectangular moving average. For example for 3-point smoothing, it gives the following value for the point j:

$$S_j = \frac{Y_{j-1} + Y_j + Y_{j+1}}{3}$$

Type 2 gives a triangular smoothing. It is like rectangular smoothing which apply two times into the signal. In other words, if we apply type 1 smoothing into the signals and then again apply type 1 smoothing into the smooth signal, the results would be equal to type 2 smoothing or triangular smoothing. For example for 3-point smoothing, it gives the following values for point j:

$$S_j = \frac{Y_{j-2} + 2Y_{j-1} + 3Y_j + 2Y_{j+1} + Y_{j+2}}{9}$$

Type 3 gives a pseudo-Gaussian which is equivalent to the rectangular smoothing that apply three times into the signal. For example for 3-point smoothing, it gives the following values for point j:

$$S_j = \frac{Y_{j-3} + 3Y_{j-2} + 6Y_{j-1} + 7Y_j + 6Y_{j+1} + 3Y_{j+2} + Y_{j+3}}{27}$$

We use type 3 in fastsmoothing function to smooth the spectral results.

- It is recommended to scale spectra plots with wave number to better visualize different regions and corresponding peaks. In order to transfer frequencies to wave-numbers, ‘Taylor Frozen hypothesis’ is used.
- Bursting period is calculated to determine its location in spectral plots. In order to calculate the bursting period, two different methods is used;

- (1) Using a simple equation which is shown below:

$$T_B = (3 \text{ to } 6) \frac{H}{V}$$

Where T_B is bursting period, H is the flow depth, and V is the mean velocity.

- (2) A burst occurs when the following condition is satisfied:

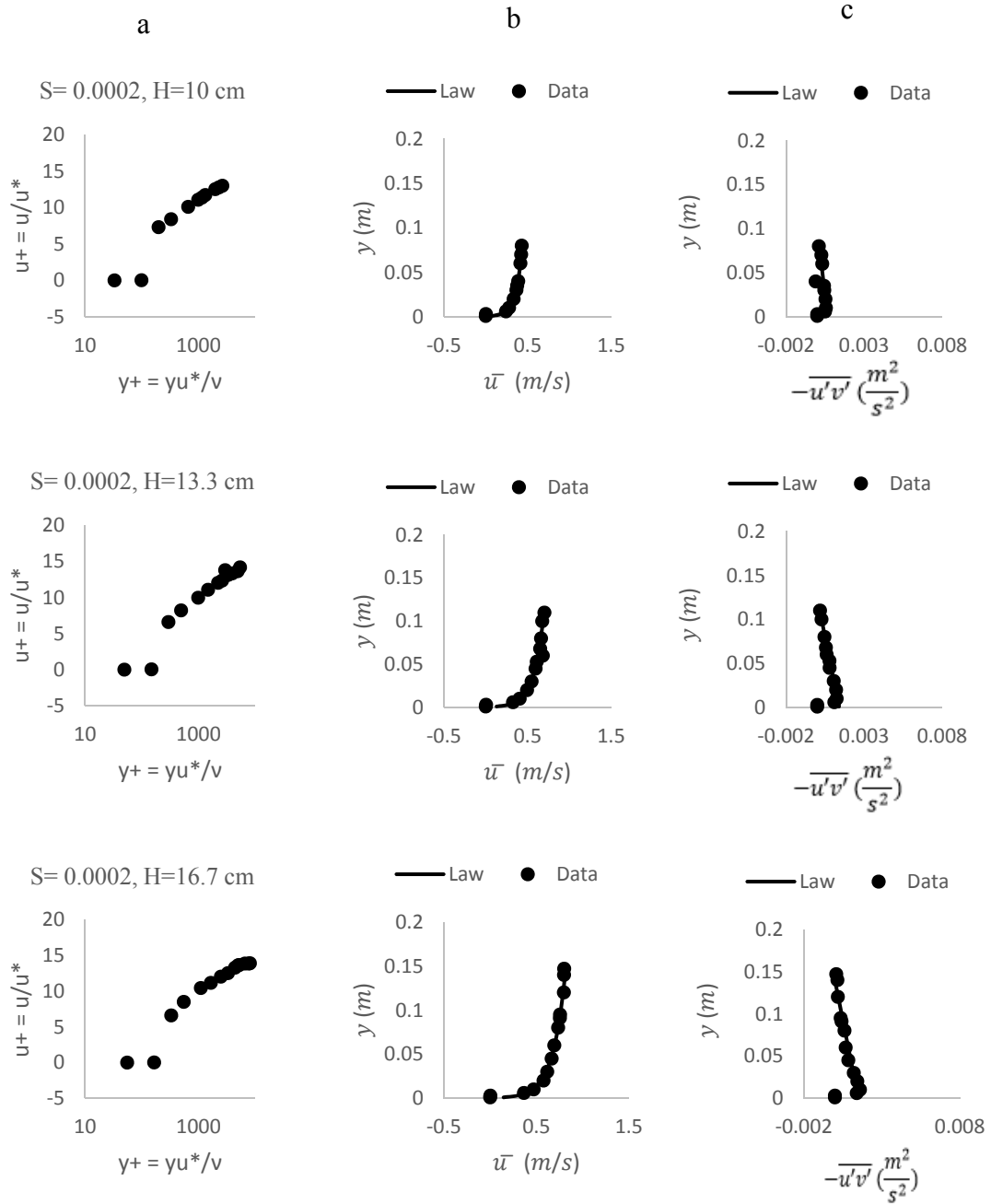
$$(0.5 \text{ to } 2)u < RMS(u)$$

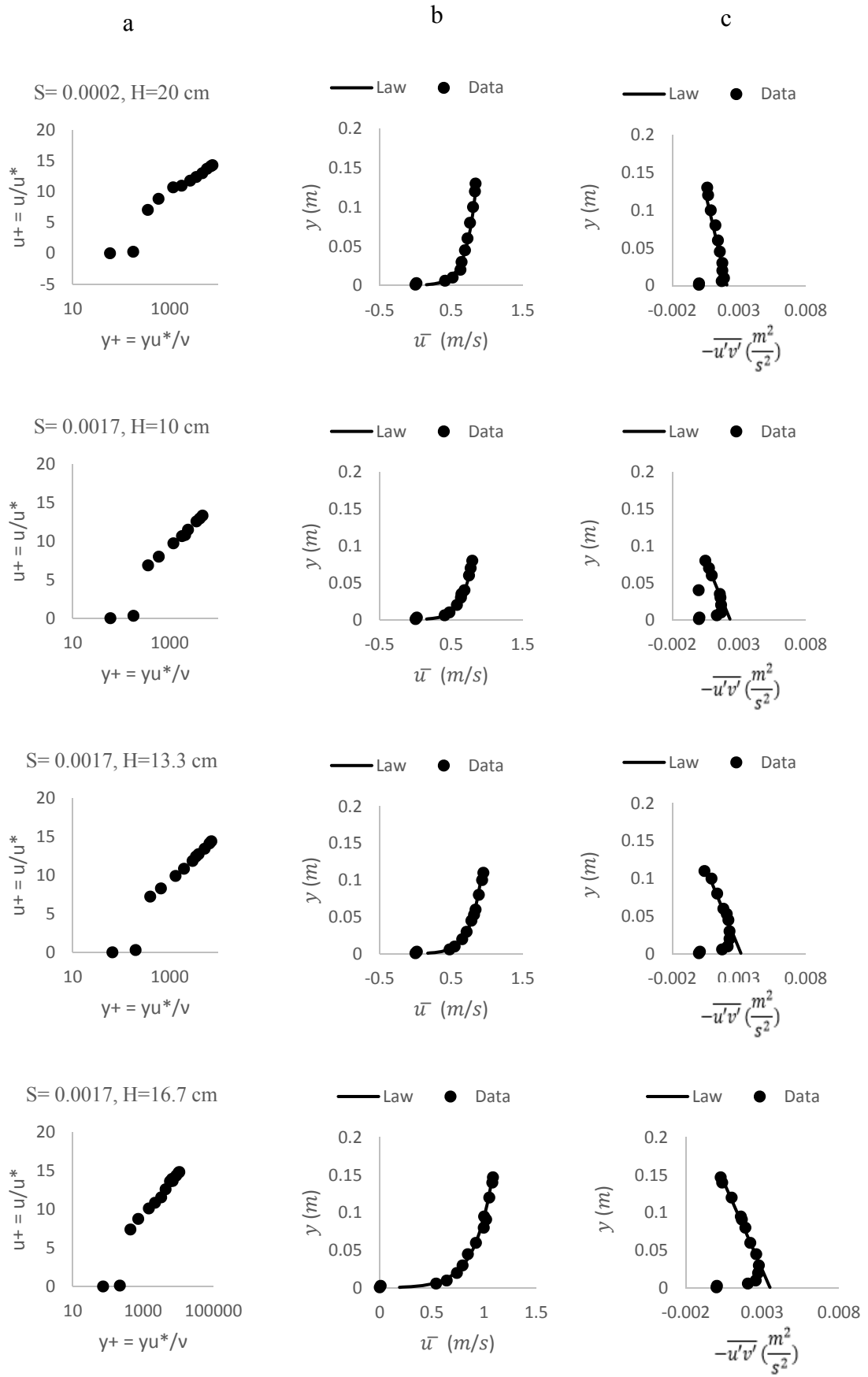
Where u is the instantaneous velocity.

In order to use this method, a MATLAB code is developed to count the bursting period. The result of this method is close to the result of first method.

Appendix III

Figure AIII.1. Results of parameter fitting to estimate the friction velocity for the small flume. (a) shows the linear region identified for fitting the friction velocity via the logarithmic law. (b) shows an example of log law fitting. (c) shows fitting of the friction velocity using the primary Reynolds stress.





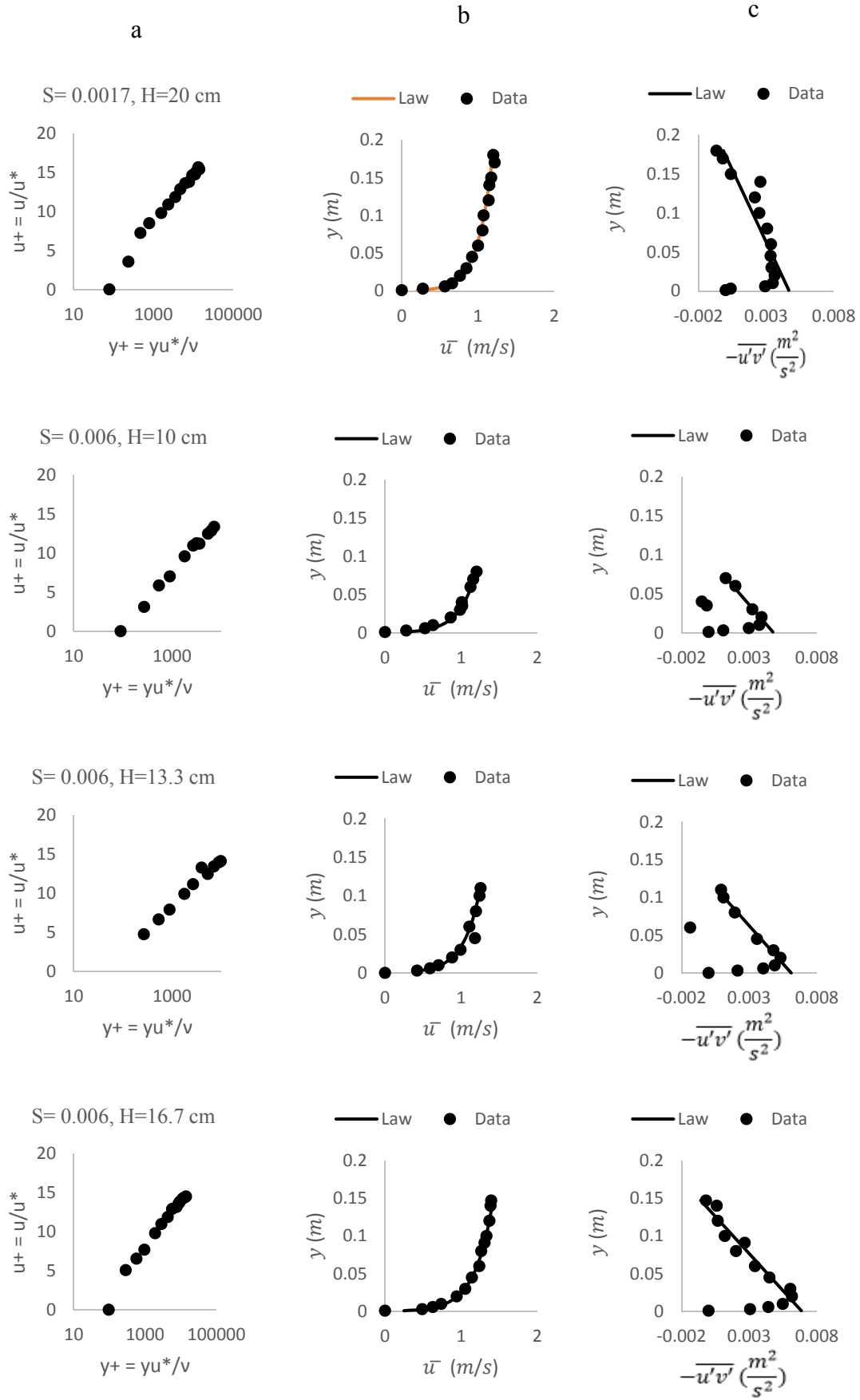
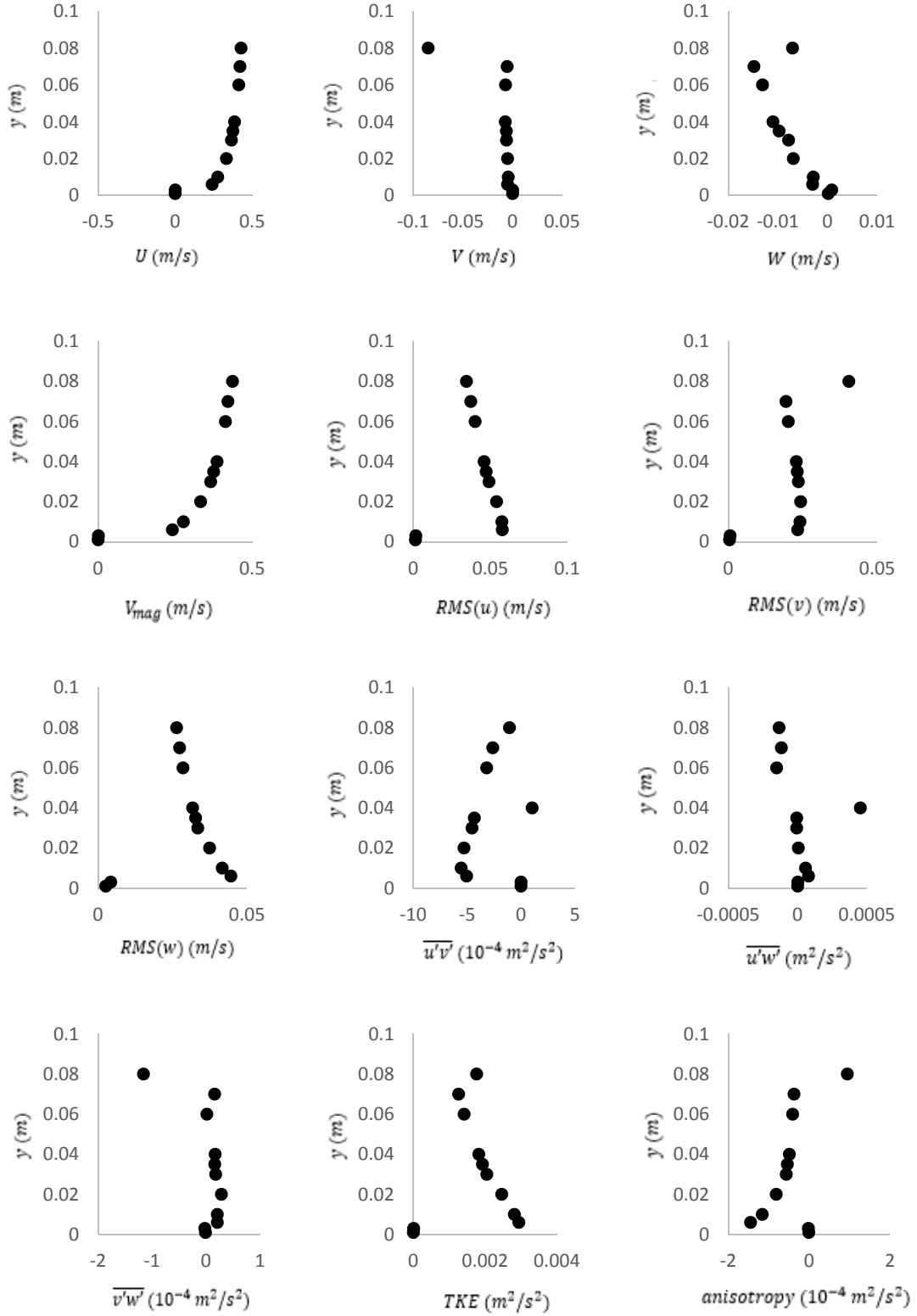
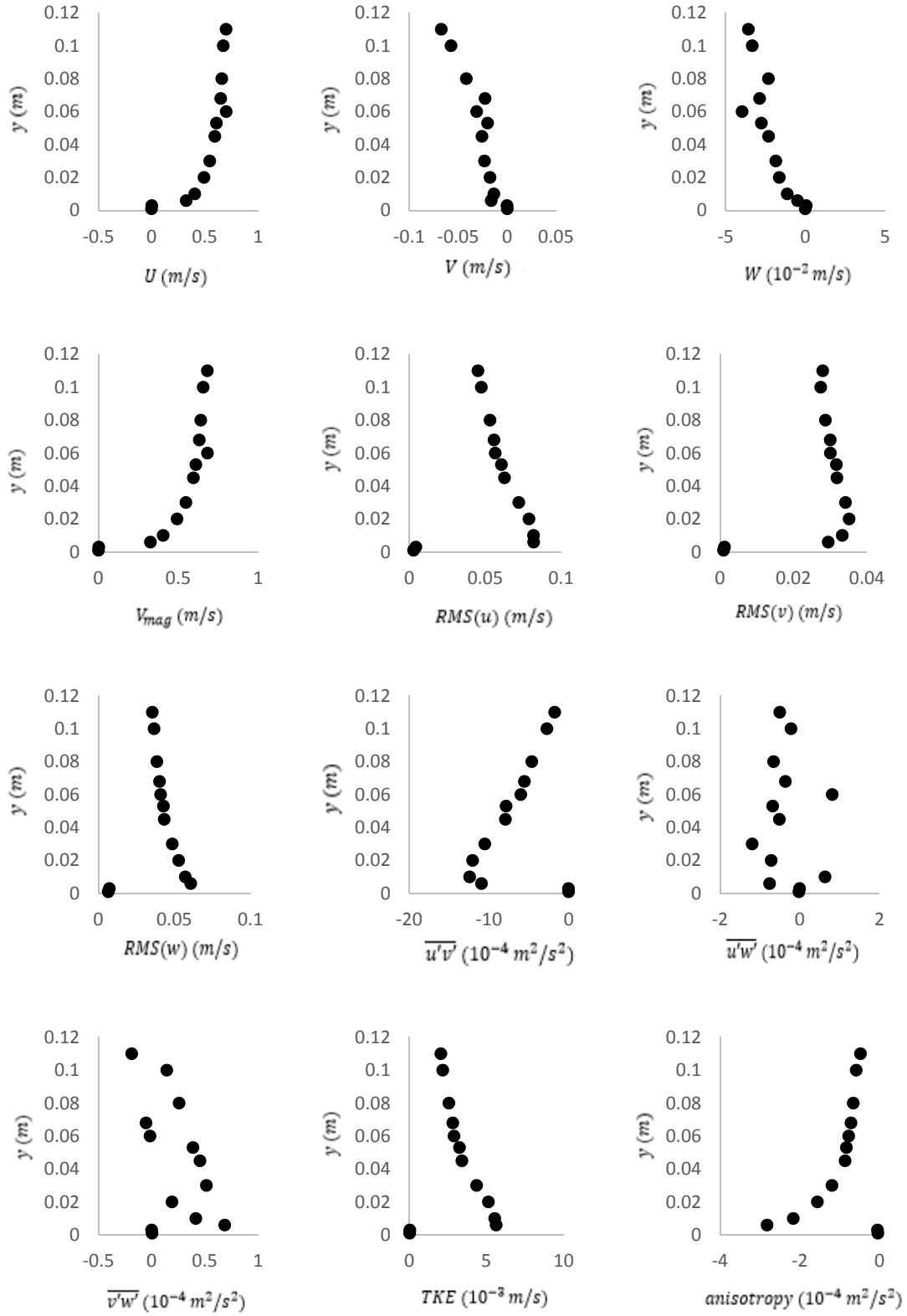


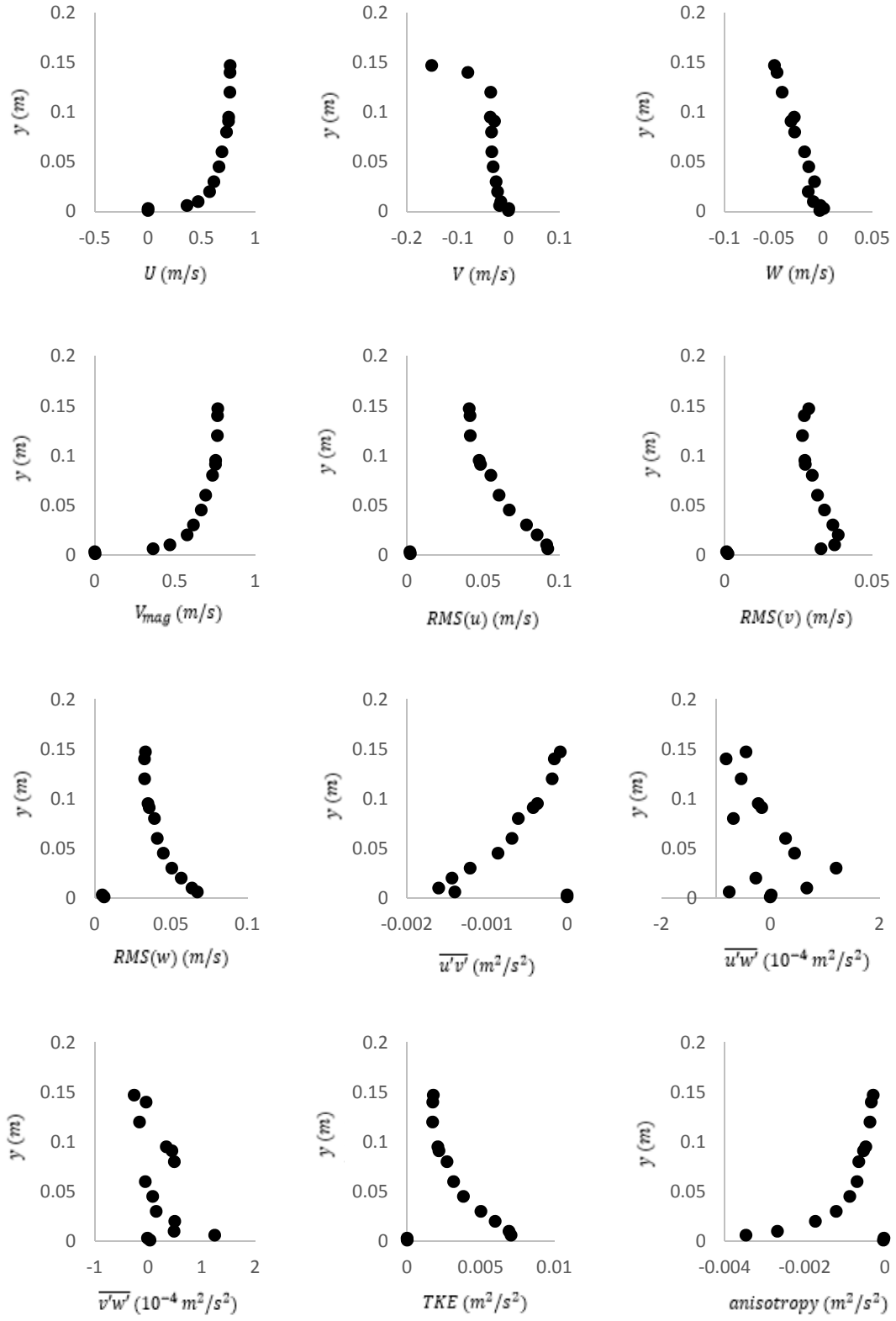
Figure AIII2: 12 Parameters for the small flume



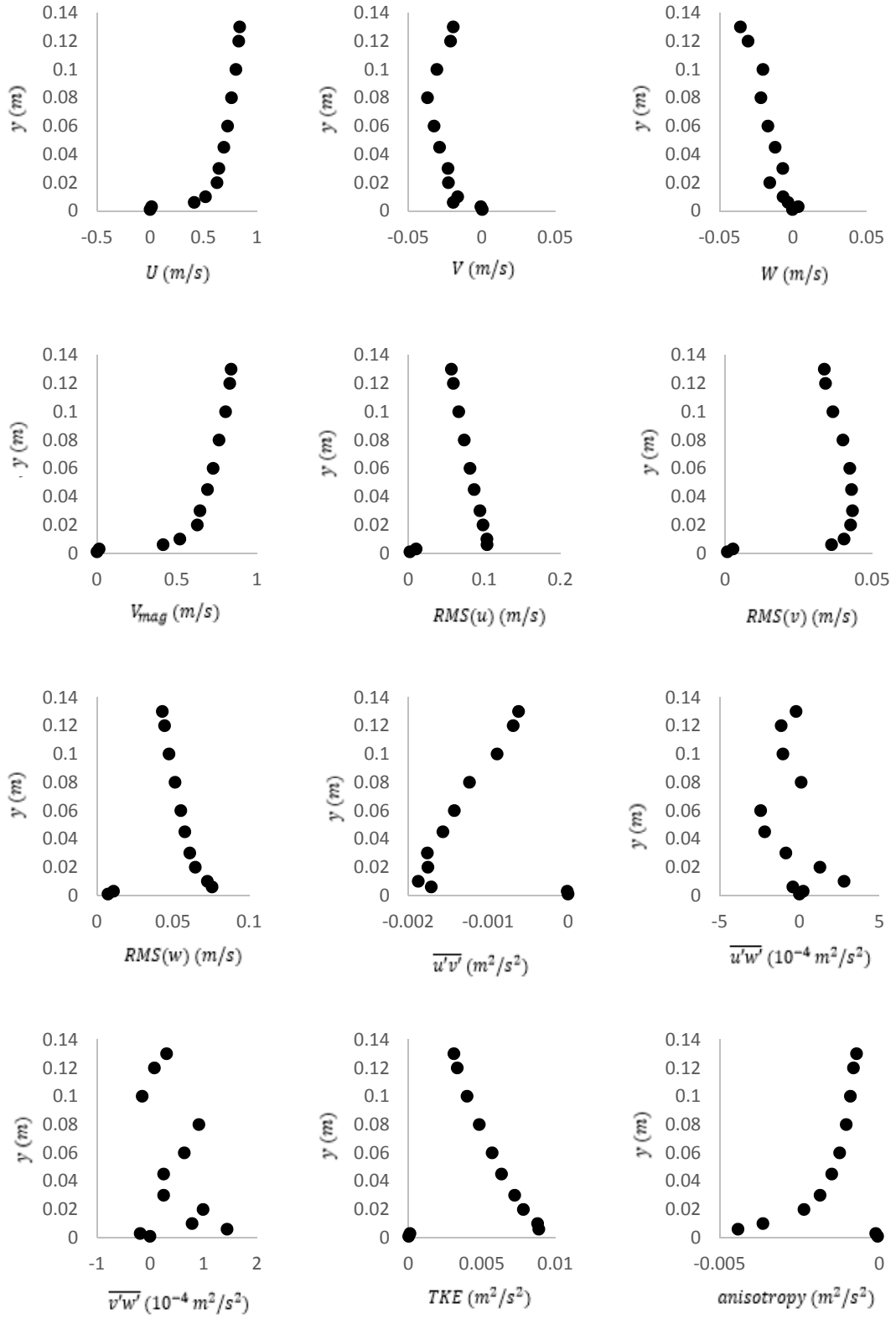
12 parameters for test 1



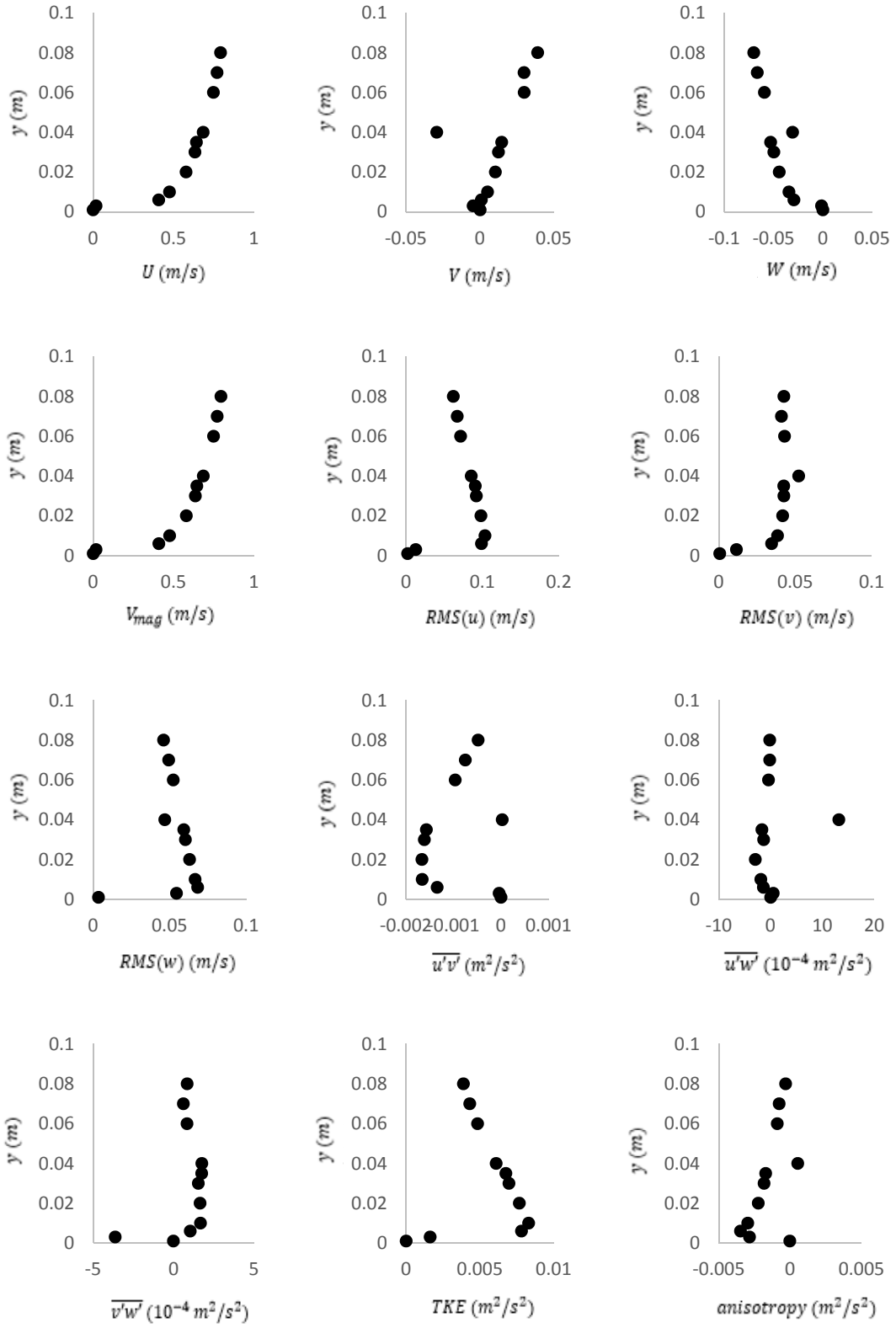
12 Parameters for test 2



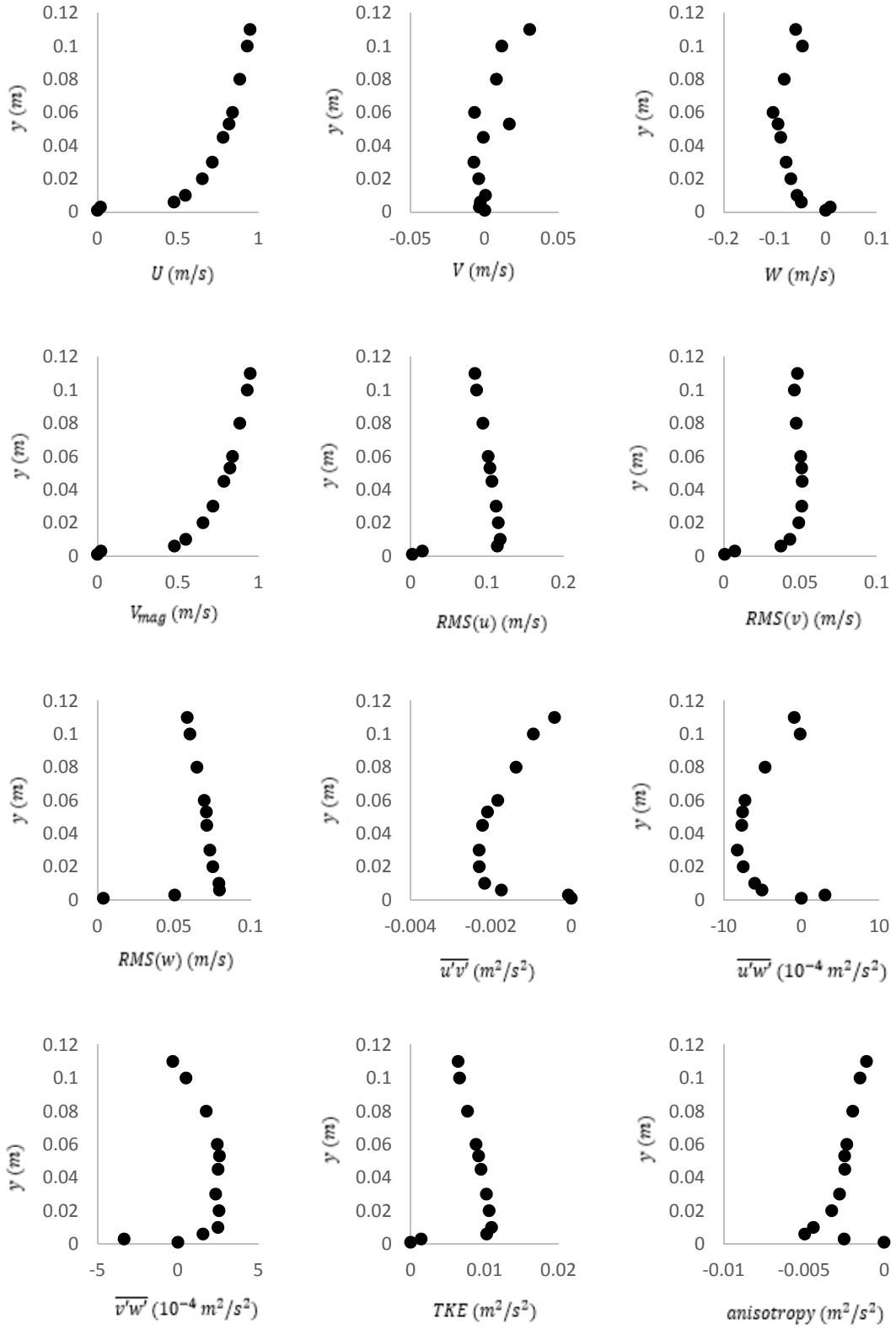
12 Parameters for test 3



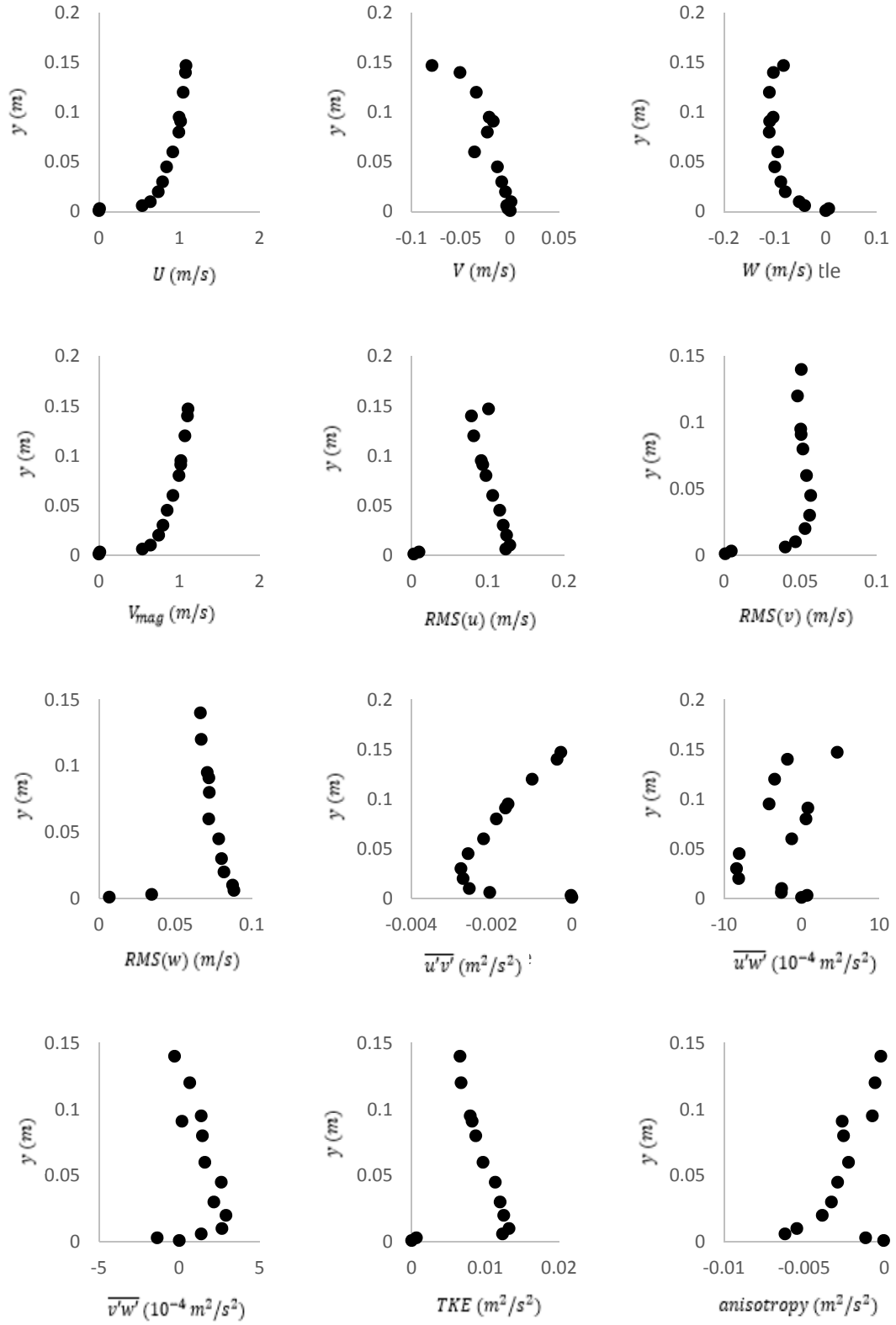
12 Parameters for test 4



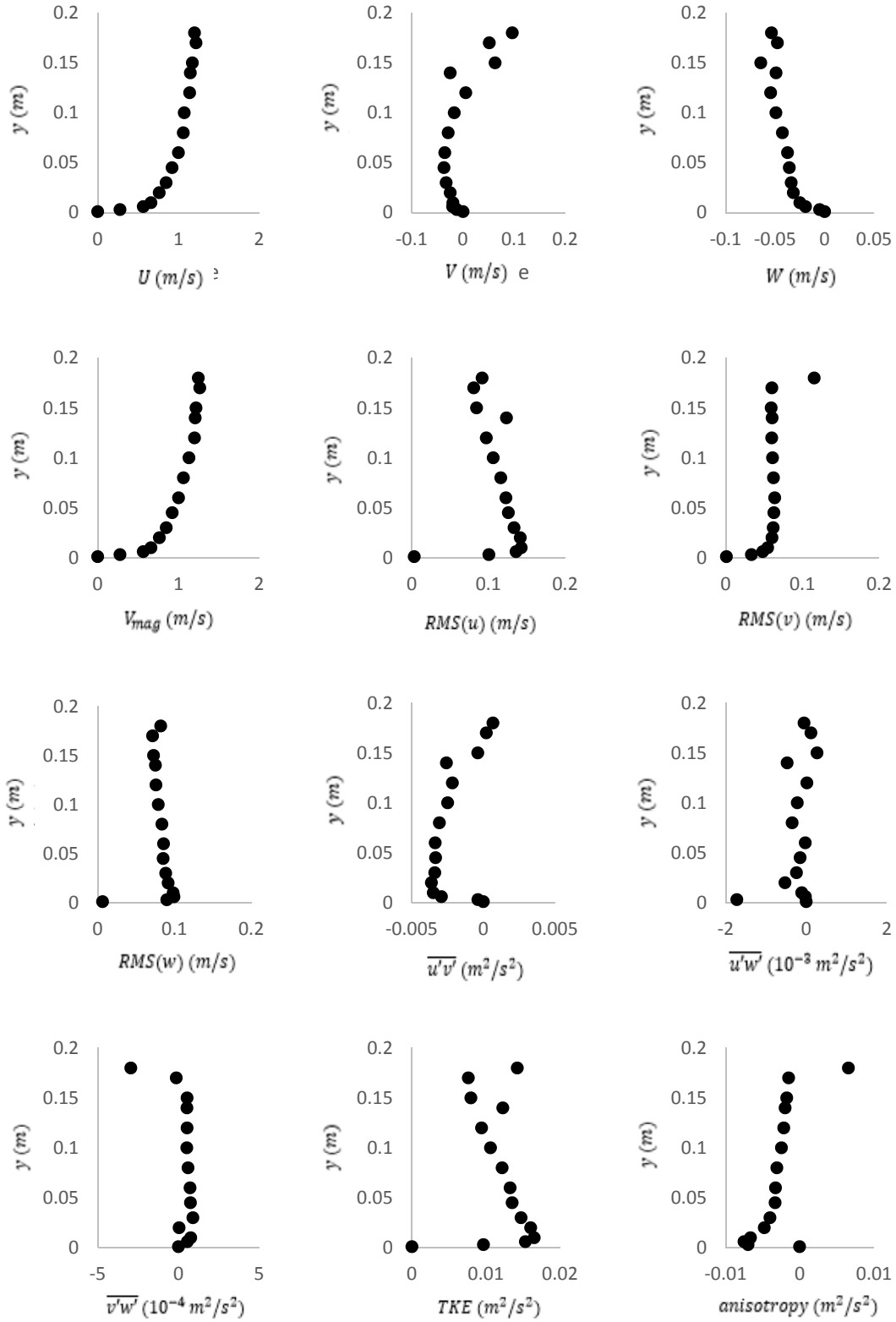
12 Parameters for test 5



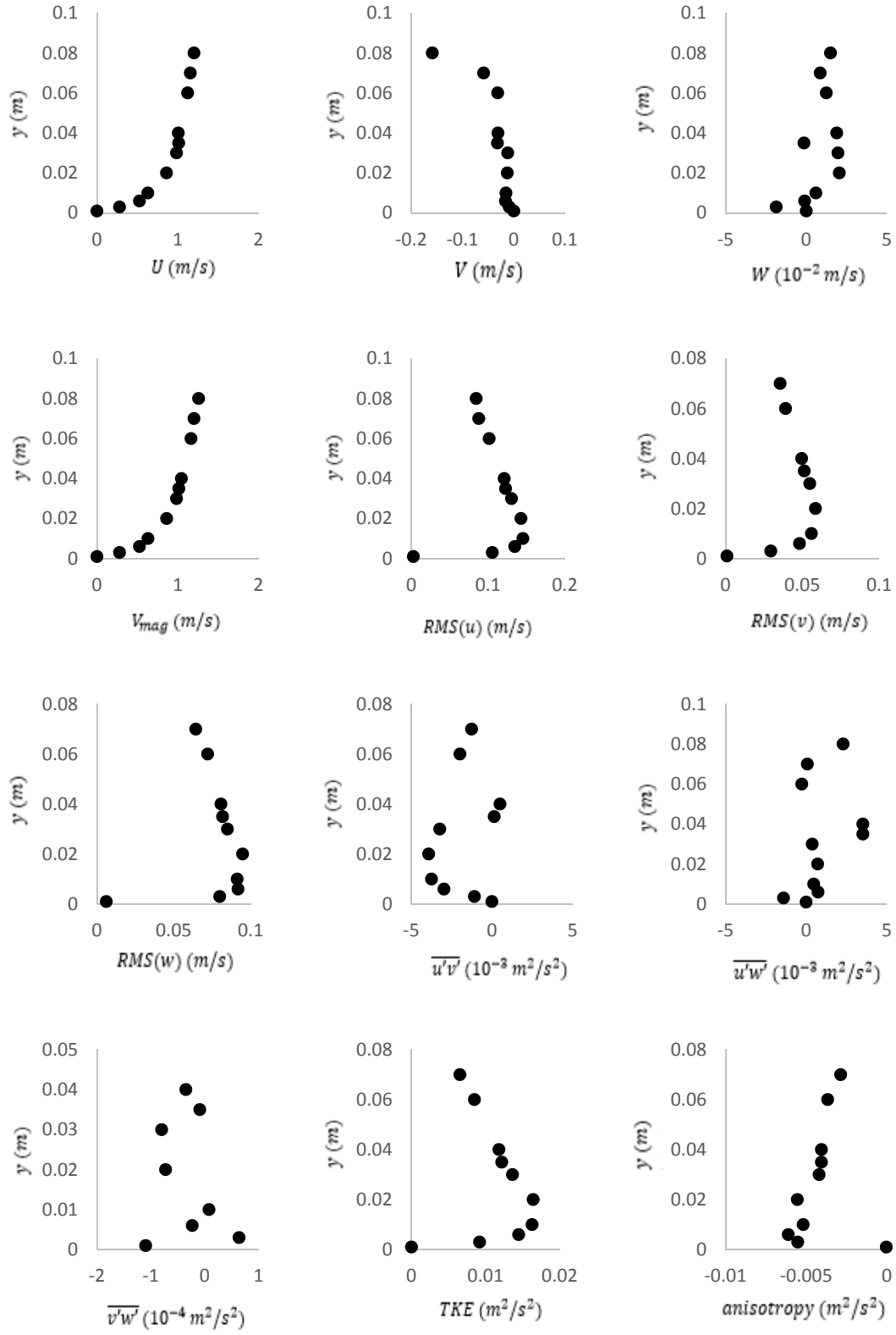
12 Parameters for test 6



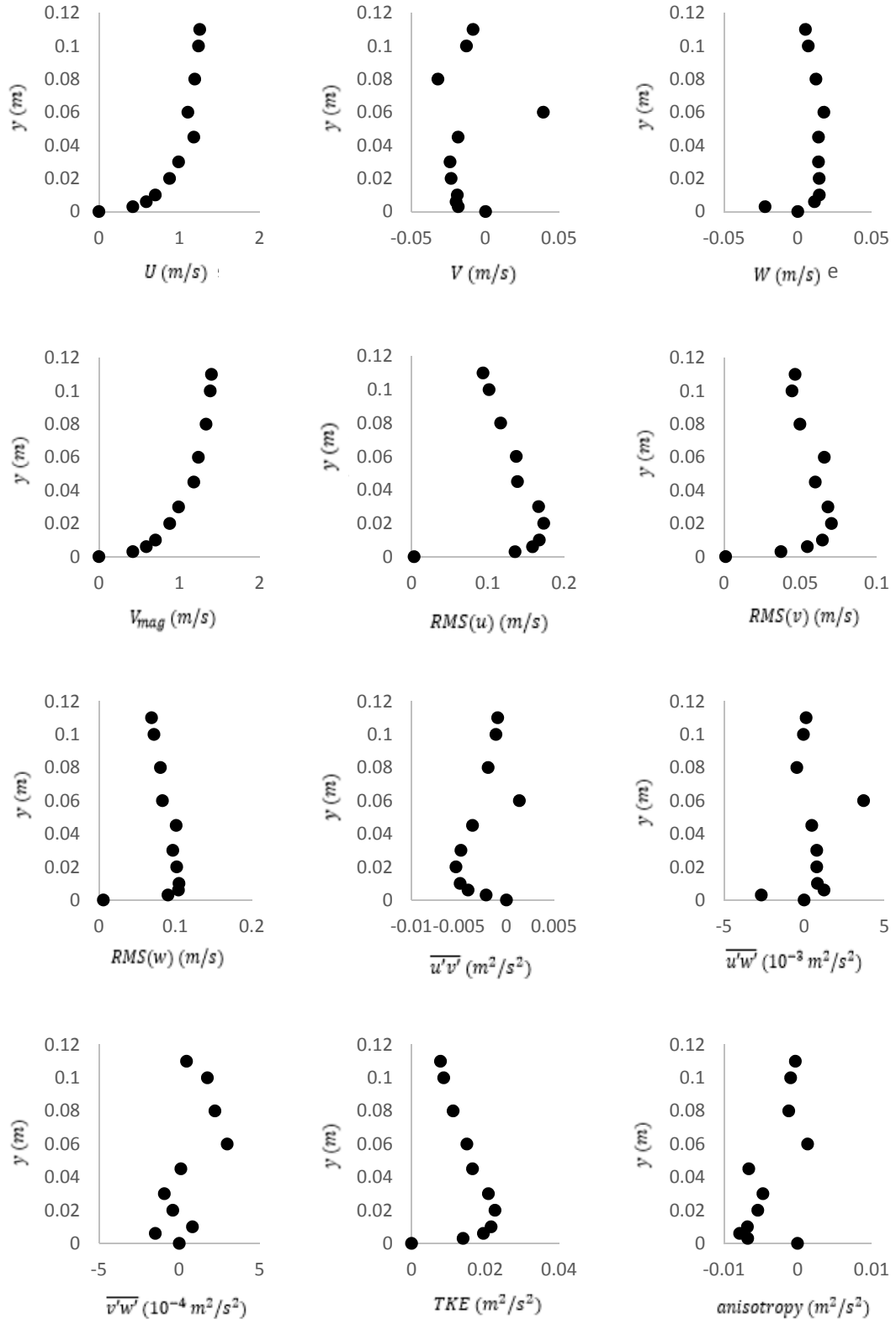
12 Parameters for test 7



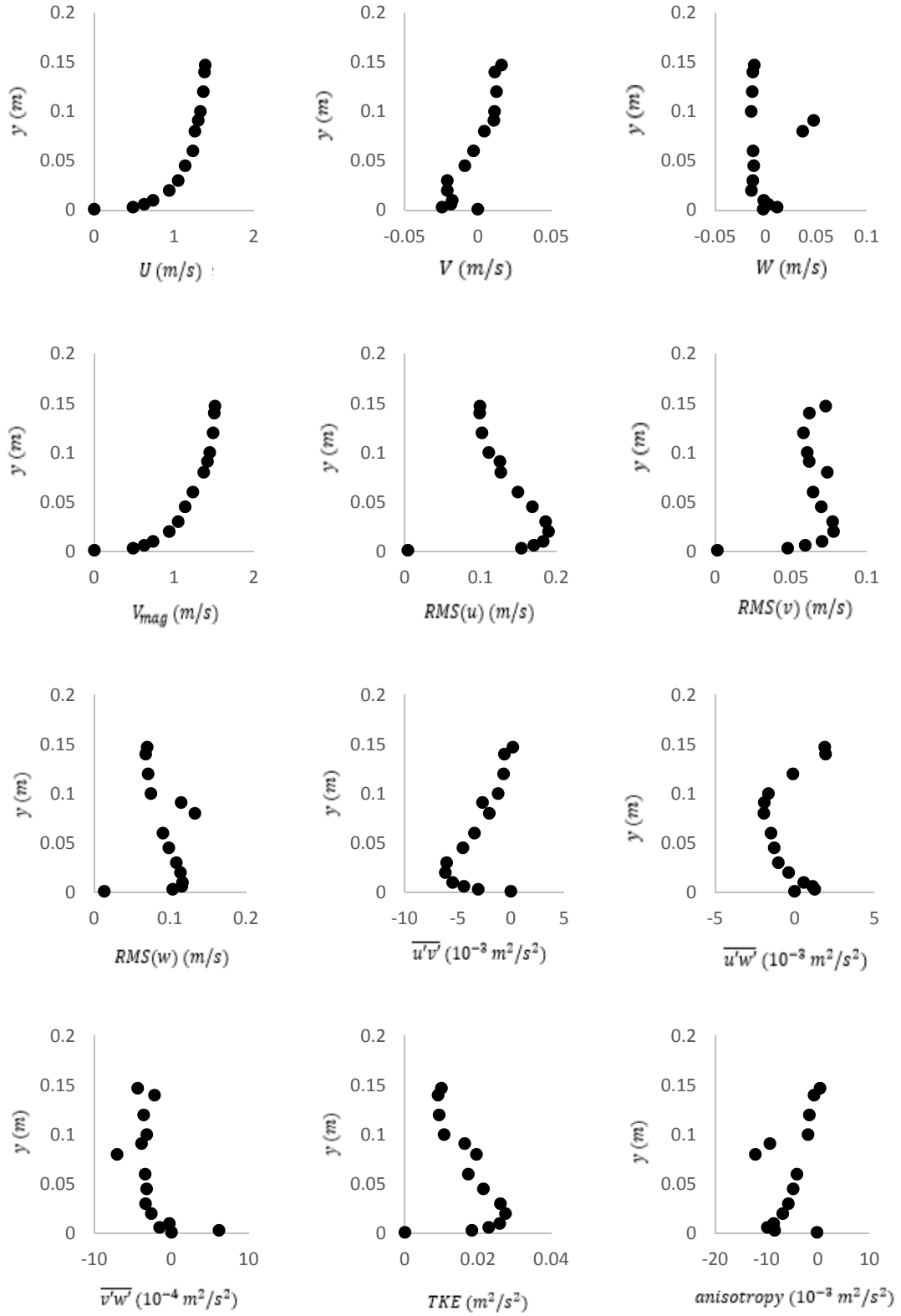
12 Parameters for test 8



12 Parameters for test 9

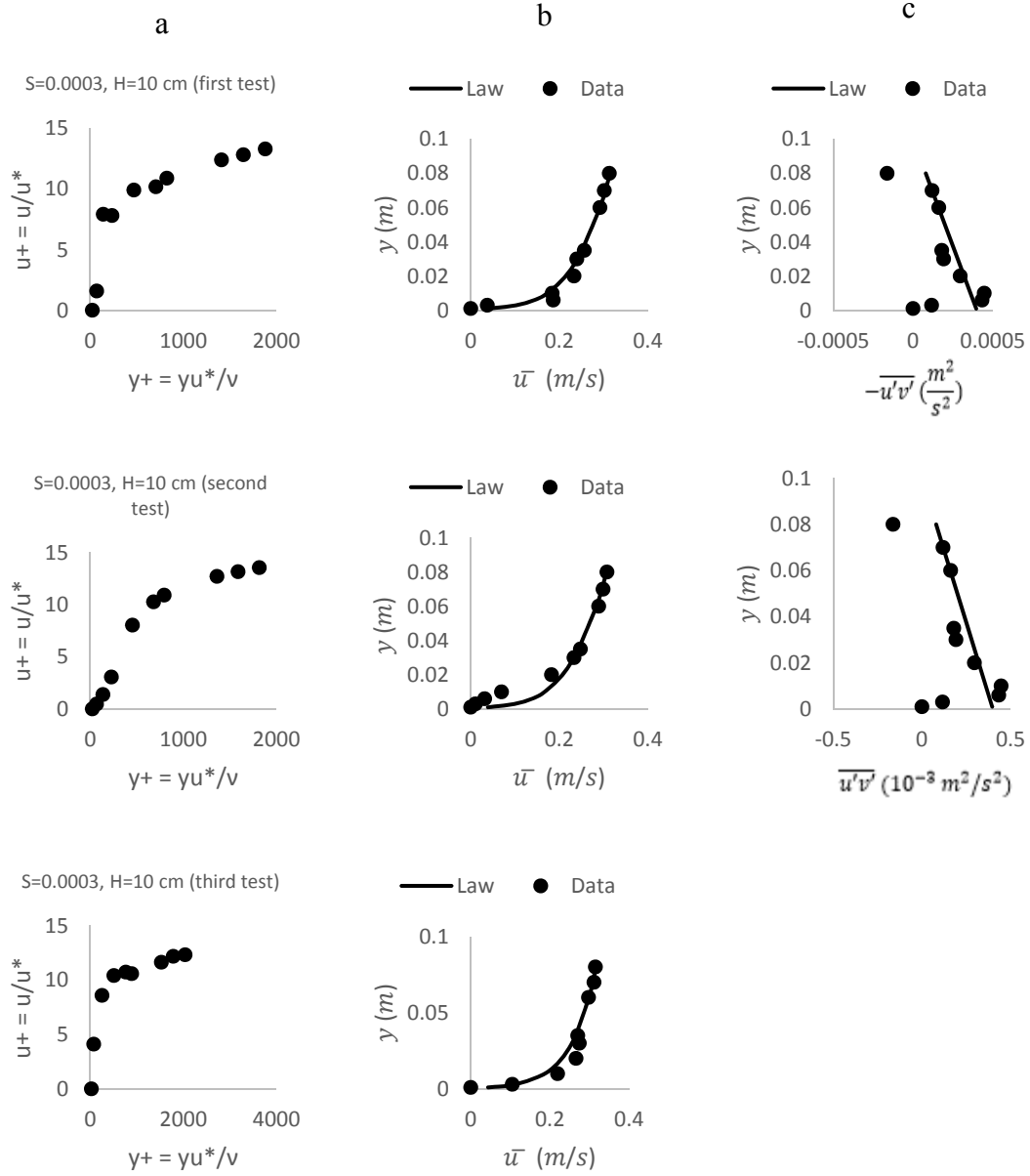


12 Parameters for test 10



12 Parameters for test 11

Figure AIII.3. Results of parameter fitting to estimate the friction velocity for the big flume. (a) shows the linear region identified for fitting the friction velocity via the logarithmic law. (b) shows an example of log law fitting. (c) shows fitting of the friction velocity using the primary Reynolds stress.



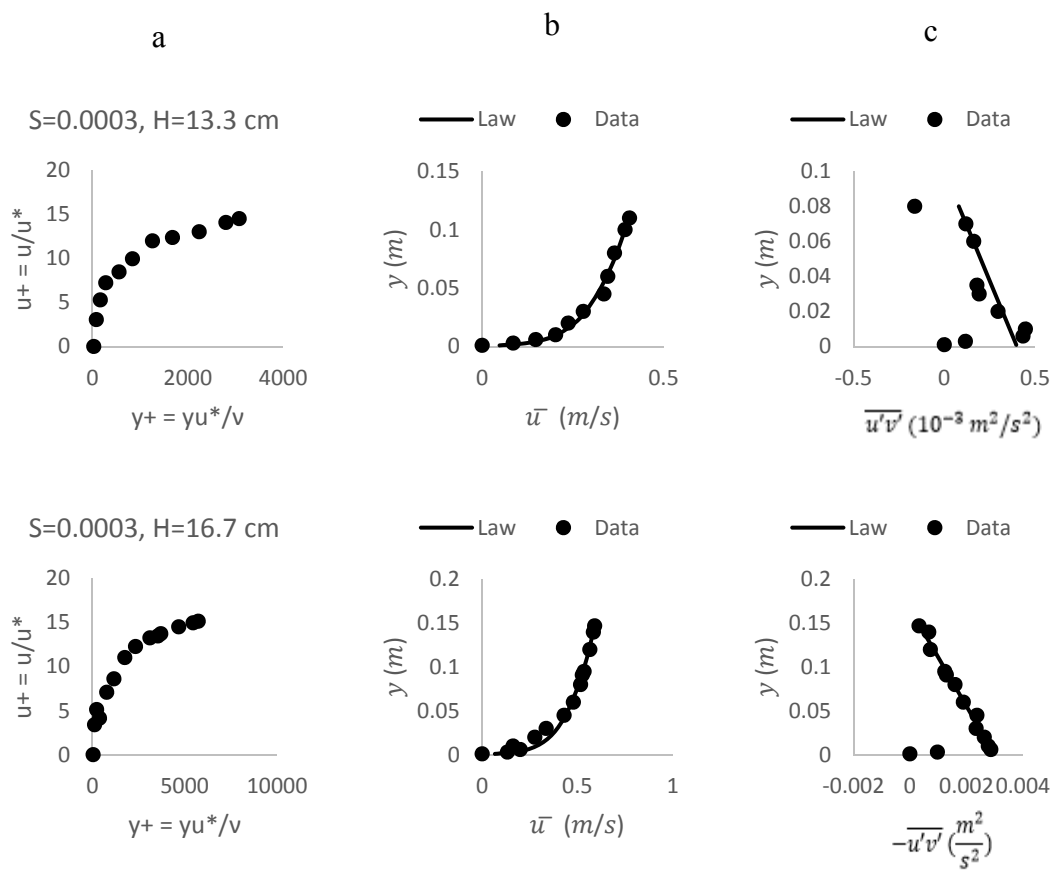
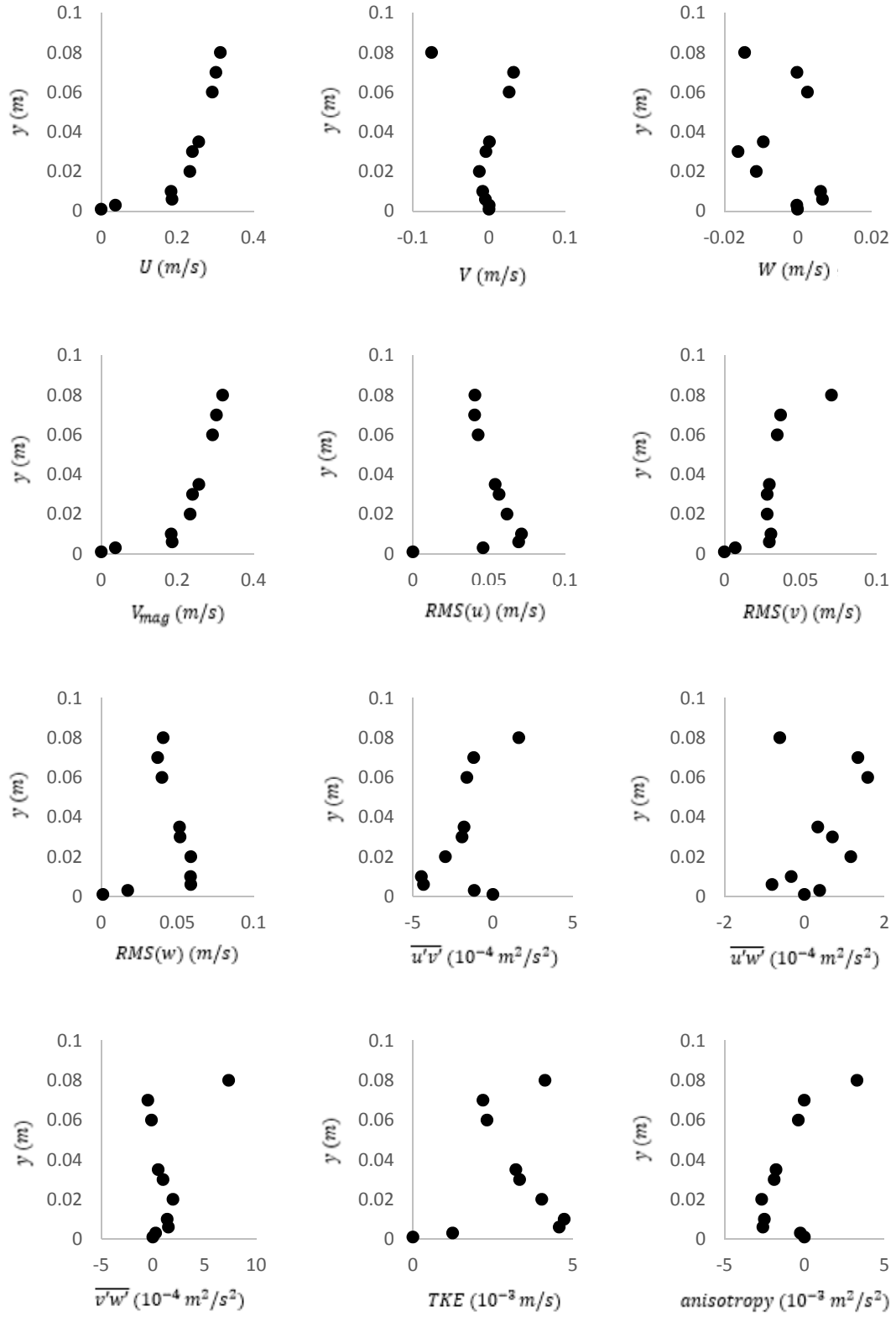
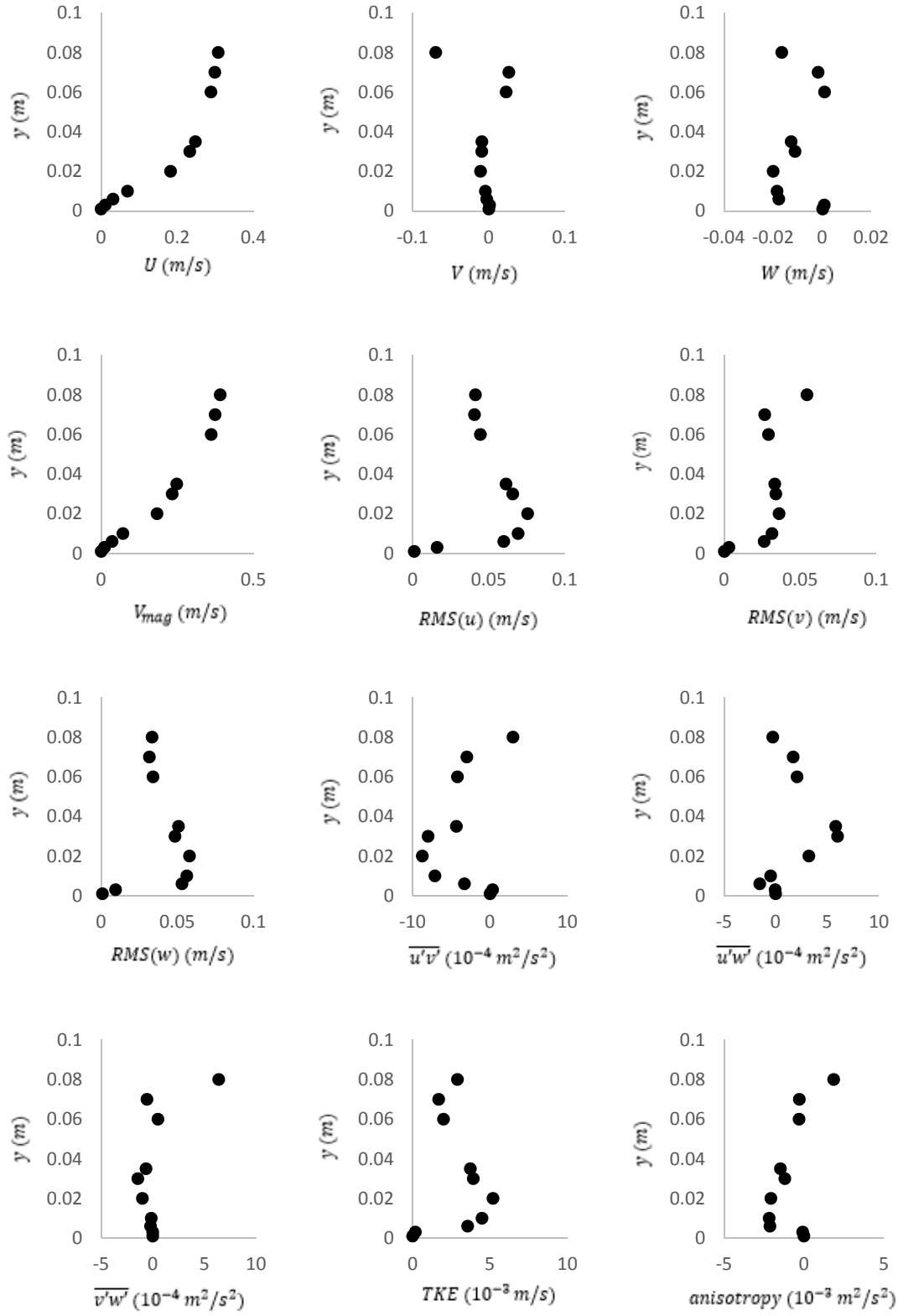


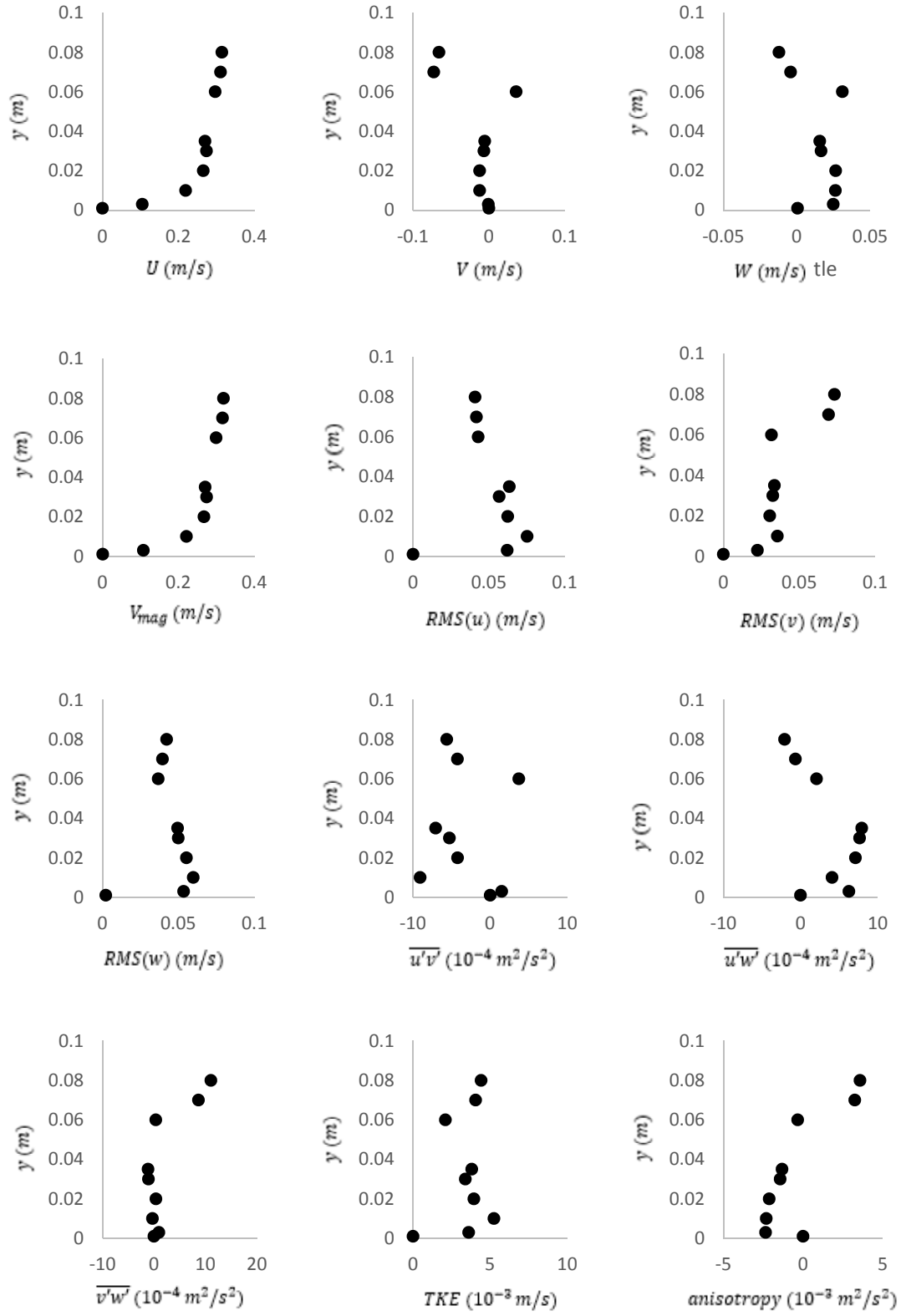
Figure AIII4: 12 Parameters for the big flume



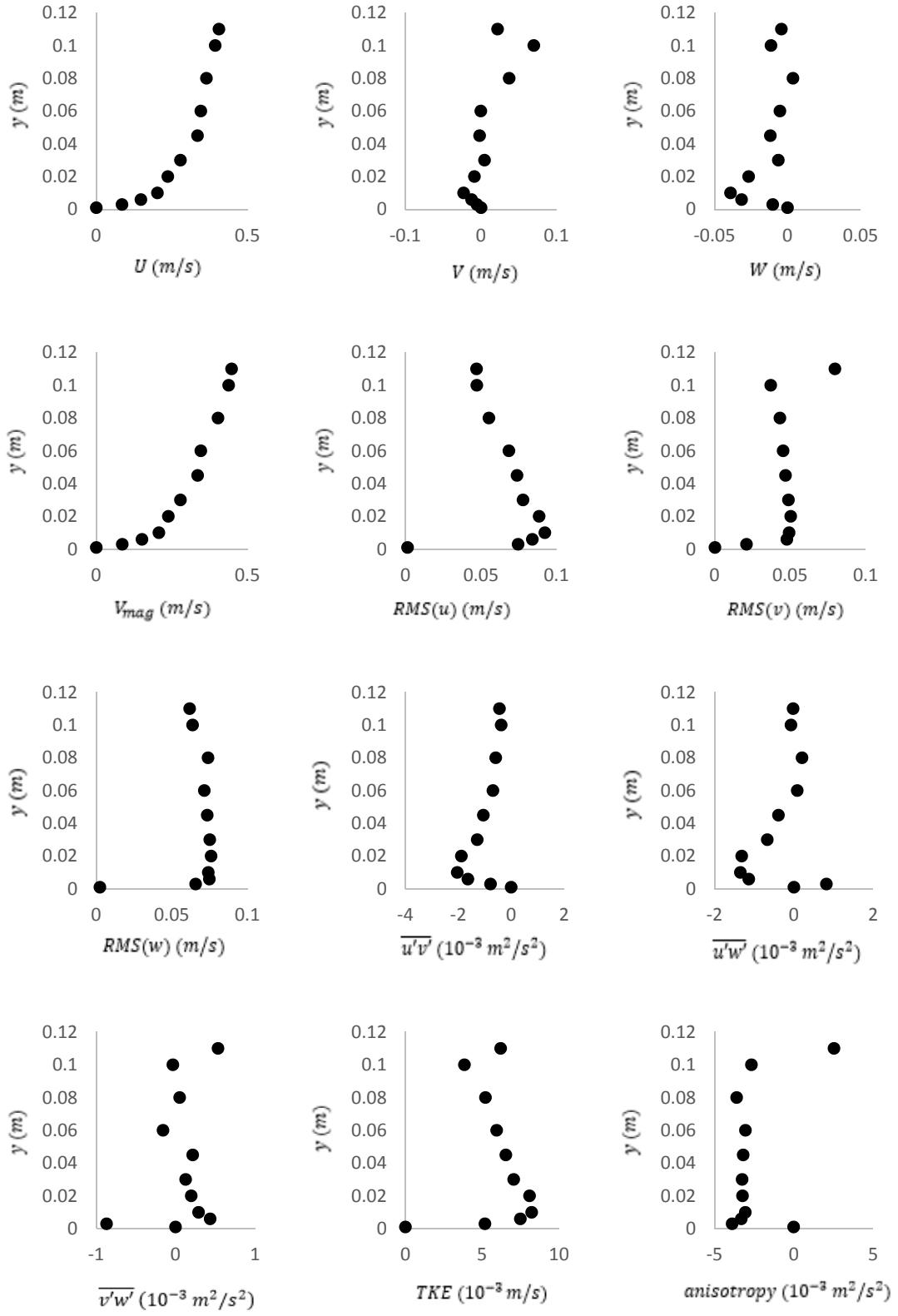
12 Parameters for test 1



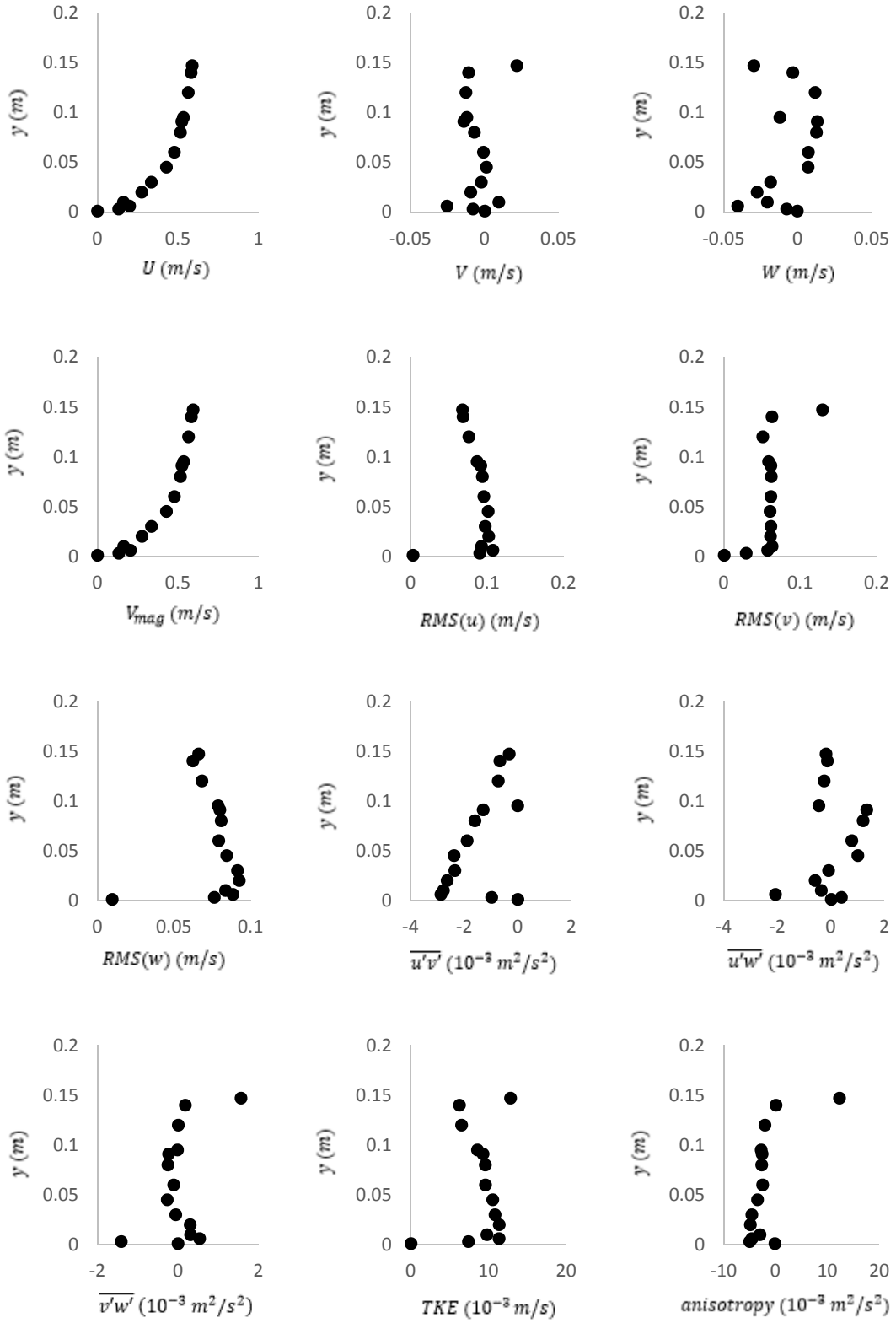
12 Parameters for test 2



12 Parameters for test 3



12 Parameters for test 4



12 parameters for test 5

References

- Amir, M., and Castro, I. P. (2011). "Turbulence in rough-wall boundary 460 layers: Universality issues." *Exp. Fluids*, 51(2), 313–326.
- Belcher, B., 2009. "Vortex model of open channel flows with gravel beds." Electronic dissertation, University of Kentucky, Lexington, KY.
- Belcher, B., Fox, J., 2009 Discussion. Rodriguez, J.F., and Garcia, M.H., 2008, Rodriguez, J.F., and Garcia, M.H. 2008. Laboratory measurements of 3-D flow patterns and turbulence in straight open channel with rough bed. *J. Hydraul. Res.* 46(4): 454–465, *Journal of Hydraulic Research* 47(5), 685-688.
- Belcher, B. and Fox, J. (2011). "Outer Scaling for Open Channel Flow over a Gravel Bed." *J. Eng. Mech.*, 10.1061/(ASCE)EM.1943-7889.0000200, 40-46.
- Buffin-Bélanger, T., Roy, A.G. 2005. 1 min in the life of a river: selecting the optimal record length for the measurement of turbulence in fluvial boundary layers. *Geomorphology*, 68, 77-94
- Cea, L., Puertas, J., Pena, L., 2007. Velocity measurements on highly turbulent free surface flow using ADV. *Exp. Fluids* 42, 333–348.
- Clauser, F. H. (1954). "The turbulent boundary layer." *Adv. Appl. Mech.*, 4, 479 10 1–51.
- Cui, H. (2011). "Estimation of velocity distribution and suspended sediment discharge in open channels using entropy." M.S. thesis, Texas A&M Univ., College Station, TX
- Fox, J.F., Papanicolaou, A.N., Kjos, L., 2005. Eddy taxonomy methodology around a submerged barb obstacle within a fixed rough bed. *Journal of Engineering Mechanics* 131, 1082–1101.
- Fox, J. F. 2002. "Investigation of flow characteristics around submerged WSDOT barbs."

- MS thesis, Washington State Univ. at Pullman, Pullman, Wash.
- Fox, J. and Stewart, R. (2014). "Mixed Scaling for Open-Channel Flow over Gravel and Cobbles." *J. Eng. Mech.*, 10.1061/(ASCE)EM.1943-7889.0000793, 06014010.
- Franca M.J., Ferrera, R.M.L, Cardoso, A.H. and Lemmin, U. (2010). Double-average methodology applied to turbulent gravel-bed river flows. *J. River Flow*, 2010, 59-65.
- George, W. K., and Castillo, L. 1997. "Zero-pressure-gradient turbulent boundary layer." *Appl. Mech. Rev.*, 5012, 689–729.
- Goring, D.G., Nikora, V.I., 2002. Despiking Acoustic Doppler Velocimeter data. *J. Hydraul. Eng.* (128), 117–126.
- Horoshenkov, K. V., A. Nichols, S. J. Tait, and G. A. Maximov (2013), The pattern of surface waves in a shallow free surface flow, *J. Geophys. Res. Earth Surf.*, 118, 1864–1876, doi:10.1002/jgrf.20117.
- Hurther, D., Lemmin, U., Terray, E.A., 2007. Turbulent transport in the outer region of rough-wall open-channel flows: The contribution of large coherent shear stress structures (LC3S). *Journal of Fluid Mechanics* 574, 465–493.
- Kader, B. A. and Yaglom, A. M.: 1984, 'Turbulent Structure of an Unstable Atmospheric Layer', in R. Z. Sagdeyev (ed.), *Nonlinear and Turbulent Processes in Physics*, vol. 2, pp. 829–845, Harwood Academic, Boston, MA.
- Katul, G. and Chu, C.R. 1998. A Theoretical and Experimental Investigation of Energy-Containing Scales in the Dynamic Sublayer of Boundary-Layer Flows. *Boundary-Layer Meteorology*. Volume 86, Issue2. Pp 279-312.
- Kendall, A. and Koochesfahani, M. 2006. A method for estimating wall friction in

- turbulent boundary layers. 25th AIAA Aerodynamic Measurement Technology and Ground Testing Conference, AIAA 2006-3834
- Kim, K.C. and Adrian, R.J. 1999. Very large-scale motion in the outer layer. *Physics of fluid* 11, 417
- Liu, Z.C., Adrian, R J., Hanratty, T.J., 2001. Large-scale modes of turbulent channel flow: transport and structure. *Journal of Fluid Mechanics* 448, 53-80.
- MacVicar, B., Dilling, S. and Lacey, J. 2014. Multi-instrument turbulence toolbox (MITT): Open-source MATLAB algorithms for the analysis of high-frequency flow velocity time series datasets. *Journal of Computers and Geosciences*
- Nezu, I., Nakagawa, H., 1993. *Turbulence in open channel flows*, A. A. Balkema, Rotterdam, The Netherlands.
- Nikora, V.I., Goring, D.G., 1998. ADV measurements of turbulence: can we improve their interpretation? *J. Hydraul. Eng.* 124, 630–634.
- Nikora, V. and Goring, D. (2000). "Flow Turbulence over Fixed and Weakly Mobile Gravel Beds." *J. Hydraul. Eng.*, 10.1061/(ASCE)0733-9429(2000)126:9(679), 679-690.
- Nikora, V. I., D. Goring, I. McEwan, and G. Griffiths (2001), Spatially averaged open channel flow over rough bed, *J. Hydraul. Eng.*, 127(2), 123–133.
- Nikora, V.L., 2005. Flow turbulence over gravel-bed: Spectral scaling and coherent structures. *Acta Geophysica Polonica* 53(4):539-552
- Nikora, V., Roy, A.G., 2012. Secondary flows in rivers: Theoretical framework, recent advances, and current challenges. *Gravel Bed Rivers: Processes, Tools, Environments*, 3-22.

Nikora, V.I., 1999: “Origin of the “-1” spectral law in wall-bounded turbulence”, *Phys. Rev. Lett.* 83, pp. 734-737.

Nortek (2011). Vectrino-II profiling velocimeter. Software users guide.

Perry, A.E., and M.S. Chong, 1982: “On the mechanism of wall turbulence, *J. Fluid Mech.* 119, pp. 173-217.

Perry, A. E. and Abell, C. J.: 1977, ‘Asymptotic Similarity of Turbulence Structures in Smooth- and Rough-Walled Pipes’, *J. Fluid Mech.* 79, 785–799.

Picek T, Matoušek V (2008): Comparison of flow characteristics measured using horizontal- and vertical-oriented ADV probes, Proc. The 22nd Symposium on Anemometry, Holany-Litice in press (in Czech).

Pons, A. (2007). Comparing different methods of shear velocity estimates under field conditions. Master internship report, university of Guelph, pages 1–26.

Robinson, S. K. (1991). Coherent motions in the turbulent boundary layer. *Annual Review of Fluid Mechanics* 23(1), 601-639.

Roy, A.G., Buffin-Bélanger, T., Lamarre, H., Kirkbride, A.D., 2004. Size, shape and dynamics of large-scale turbulent flow structures in a gravel-bed river. *Journal of Fluid Mechanics* 500, 1–27.

Simons, D.B and Senturk, F. Sediment transport technology textbook

Shvidchenko, A.B., Pender, G., 2001. “Macroturbulent structure of open-channel flow over gravel beds.” *Water Resources Research* 37(3), 709–719.

Stewart, R. and Fox, J. 2015. Role of macroturbulence to sustain turbulent energy in decelerating flows over a gravel bed. *Journal of Geomorphology*.

- Tchen, C. M.: 1953, 'On the Spectrum of Energy in Turbulent Shear Flow', Journal of Research of the National Bureau of Standards 50, 51–62.
- Townsend, A. A. (1976). 525 The structure of turbulent shear flow, 2nd Ed., Cambridge University Press, Cambridge, U.K.
- Venditti, J., and Bennett, S. 2000. Spectral analysis of turbulent flow and suspended sediment transport over fixed dunes, J. Geophys. Res., [Oceans], 105C9, 2035–2047.
- Wahl T.L., 2000. Analyzing ADV data using WinADV. Proceedings Joint Conference on Water Resources Engineering and Water Resources Planning and Management, American Society of Civil Engineers, Minneapolis, 30 July–2 August. www.usbr.gov/wrrl/twahl/winadv.
- Welch, P. D. (1967), "The use of Fast Fourier Transform for the estimation of power spectra: A method based on time averaging over short, modified periodograms", *IEEE Transactions on Audio and Electroacoustics*, AU-15 (2): 70–73
- Zanoun, E., Durst, F., and Nagib, H. 2003, "Evaluating the Law of the Wall in Two-Dimensional Fully Developed Channel Flows," *Phys. Fluids*, 15, 2003, pp. 3079-3089

VITA

Education

University of Kentucky	Civil Engineering	M.S. (2014-2016)	GPA: 3.88/4
Sharif University of Technology	Civil Engineering	B.Sc. (2010-2014)	GPA: 3.22/4

Professional Experience:

- **Hydraulic Engineer (Internship), Abkhan Company** May-July 2014
- **Teaching Assistant, (University of Kentucky, Sharif University of Technology) 2013-Present**
 - Fluid Mechanic
 - Dynamics
 - General Physics

Professional Publication:

- Study of macroturbulence in gravel and cobble-bed channels. (Conference Paper)

Honors and Awards:

- Ranked top 0.05% (122 out of 460000) in Iran Public Universities Entrance Exam. 2010
- Semi- finalist in Physics Olympiad during High School. 2008
- Finalist in “the 10th Khwarizmi Youth Nation-Wide Festival. 2008
- Finalist in Laboratory competition in Khorasan Province, Iran. 2008

Amirreza Ghasemi